University of London

Imperial College of Science, Technology and Medicine

Department of Mechanical Engineering

Planning for Steerable Needles in Neurosurgery

Marlene Pinzi

Submitted in part fulfilment of the requirements for the degree of
Doctor of Philosophy in Mechanical Engineering and
the Diploma of Imperial College, December 2020

Abstract

The increasing adoption of robotic-assisted surgery has opened up the possibility to control innovative dexterous tools to improve patient outcomes in a minimally invasive way. Steerable needles belong to this category, and their potential has been recognised in various surgical fields, including neurosurgery. However, planning for steerable catheters' insertions might appear counterintuitive even for expert clinicians. Strategies and tools to aid the surgeon in selecting a feasible trajectory to follow and methods to assist them intra-operatively during the insertion process are currently of great interest as they could accelerate steerable needles' translation from research to practical use.

However, existing computer-assisted planning (CAP) algorithms are often limited in their ability to meet both operational and kinematic constraints in the context of precise neurosurgery, due to its demanding surgical conditions and highly complex environment. The research contributions in this thesis relate to understanding the existing gap in planning curved insertions for steerable needles and implementing intelligent CAP techniques to use in the context of neurosurgery.

Among this thesis contributions showcase (i) the development of a pre-operative CAP for precise neurosurgery applications able to generate optimised paths at a safe distance from brain sensitive structures while meeting steerable needles kinematic constraints; (ii) the development of an intra-operative CAP able to adjust the current insertion path with high stability while compensating for online tissue deformation; (iii) the integration of both methods into a commercial user front-end interface (NeuroInspire, Renishaw plc.) tested during a series of user-controlled needle steering animal trials, demonstrating successful targeting performances.

(iv) investigating the use of steerable needles in the context of laser interstitial thermal therapy (LiTT) for maesial temporal lobe epilepsy patients and proposing the first LiTT CAP for steerable needles within this context.

The thesis concludes with a discussion of these contributions and suggestions for future work.

Acknowledgements

I started working at Imperial College, in the Mechatronics and Medicine (MiM) Lab during my master thesis, and I have never left since that time. Many are the reasons which made me stay and start my PhD journey at MiM. Imperial College is, for sure, a fascinating and prestigious university. This inspiring place reminds you of its extraordinary history. At the same time, it exposes you to the excellence of its current research and especially, the devotion and passion of Imperial College scientists. Although this might look like a very plausible reason for starting a PhD at Imperial, what pushed me, at first, was the respect and admiration I felt for my supervisor: Ferdinando Rodriguez y Baena. I have always thought he was at the same time a peculiar and extraordinary professor, one of those you would remember after years for his humanity and integrity. Once I got to know him better, I discovered him to be also a fantastic leader. He was indeed a role model for me, the central pillar for my personal and professional development during my time at Imperial. He incredibly managed to be a boss and a friend at the same time, pushing me outside my comfort zone and giving me honest (too honest sometimes) and transparent feedback about my work. One of my most outstanding achievements has been recently hearing him saying: "I have nothing more to teach you, this work is almost perfect, well done!".

MiM lab is populated by wonderful and capable people with which was a great pleasure to work and share knowledge during my PhD time. Eloise Matheson started this journey with me, almost the same day and in the same project, bringing some gender-balance in a men-populated lab. She has always been one of the most loved people in the lab because of her altruism and her ability to know everything about robotics, literally. I feel so blessed to have

met such a strong and intelligent woman from whom I have always tried to get inspired, and I am grateful that she is now one of my greatest friends.

Riccardo Secoli was also one of my point of reference since I came to MiM for my master thesis. I have always been very good at underestimating myself and not be fully satisfied with my work. Still, he somehow managed to put everything under a different perspective when I was looking for some reassurance. He had always given me so many significant inputs. He has always been the first one to know about any possible offer, opportunity and exciting event. He is a precious source of information and more importantly, a very good friend since he always included me in all these interesting experiences, from joining a posh Ferrari event to working on an early-stage startup together.

However, I would have never gone so far without Stefano Galvan. His remarkable experience in software engineering and his guidance throughout these years was essential for my professional growth. He taught me how to think in a logical manner, how to decompose big problems into smaller ones and how to speak less loudly in a standard lab working environment. Every time I felt stuck with my research or I lost the track, he listened to me for hours (not all PhD students can claim such treatment) and enlightened me with very useful suggestions which encouraged me not to give up.

What made my PhD time even more enjoyable was the friendship that I built with all my MiM colleagues with whom I shared part of this journey either for a short or long period. Tom Watts, who survived to be sitting next to me for a long time and kindly answered all the math-related question I had for him. He was the one that impressed me with his British politeness as well as for his squash player skills. Arnau Carrigas is also a great workmate and a special friend. His hilarious sense of humour and weird Italian accent (somehow close to the Sardinian one) manages to strike me all the times. One year he was so kind as to nominate me "best work colleague", but he surprisingly ended up winning that award. Vani Vyrdiawan, who is the most friendly and smiling person in the lab, even after becoming dad for the second time. Hisham Iqbal, who in another life should definitely be an event organiser, is instead a careful Christmas coaster buyer on one side and a surprising animal party on the other side. Then, Stephen, who

waited for me many mornings before sneaking in the staff cafeteria and keeping our caffeine levels up. Enrico, who downplays drama with his un-politically correct jokes and Fabio Tatti, who has always given me a sense of calm and optimism. Then Hadi EL Daou, the sweetest geek I've ever met and finally, Silvia Cappelletto, who brought nice energy in the lab and became a dear friend and exceptional flatmate despite the short time we spent together. I won't forget our bus rides getting in turns our head around PhD related topics.

These are only a few among the people who crossed the path with me during these years, which somehow gave me something.

Finally and not of less importance, I am thankful to my family, who supported me throughout this period, listening to my complaints and pretending to understand my research topic. They have always shown to be very proud of me, boosting my confidence when I most needed. Above all, my boyfriend Matteo Centonze who was the most patient and comprehensive person. He had the unfortunate experienced to be in lockdown with me during my PhD thesis writing time but he found the recipe to solve my mood swings with his love and attention. He knew my mood was strictly dependent on how many paths in a patient brain my path planner was going to find, still, he stayed next to me every day reminding me that was I was doing was great and with an honourable purpose.

To conclude, this was the best time of my life, the most exciting and inspiring but also the one in which I met most of the people that will remain in my life in the future.

Dedication

To my family,

who taught me the power to question and the value of knowledge as a mean to freedom.

Alla mia famiglia,

che mi ha insegnato il potere della curiosità e il valore della conoscenza come strumento di libertà.

'Gutta cavat lapidem non vi,
sed saepe cadendo.'

'Dripping water wears away a stone not with its strength,
but with its constancy'

Lucrezio

Declaration of Originality

This is to certify that to the best of my knowledge, the content of this thesis is my own work. This thesis has not been submitted for any degree or other purposes. I certify that the intellectual content of this thesis is the product of my own work and that all the assistance received in preparing this thesis and sources have been acknowledged.

Copyright Declaration

Nomenclature

AFT Adaptive Fractal Tree

AHC Amygdalohippocampal Complex

AHFT Adaptive Hérmite Fractal Tree

CAP Computer-Assisted Planning

CED Convection Enhanced Delivery

*EDEN*2020 An Enhanced Delivery Ecosystem for Neurosurgery

EnCx Entorhinal Cortex

FuG Fusiform Gyrus

GPU Graphic Processing Unit

LGN Lateral Geniculate Nucleus

LiTT Laser Interstitial Thermal Therapy

MIS Minimally Invasive Surgery

PBN Programmable Bevel Tip

PHG Parahippocampal Gyrus

PiCx Piriform Cortex

RRT Rapidly-exploring Random Tree

Contents

List of Tables

List of Figures

Chapter 1

Introduction

1.1 Motivation: a clinical need

Minimally invasive surgery (MIS) aims to reduce morbidity and tissue disruption of essential structures in the brain, such as nerves that control vision and hearing, making it less likely that a person will experience changes in function.

Rapid developments have taken place due to the significant benefits MIS presents for the patient, including less trauma, shorter hospital stays and reduced recovery times as reported by [WGJD08].

In traditional open neurosurgeries, surgeons create large incisions to be able to operate and access the target area. With MIS, surgeons can reduce the intervention to a few small holes or openings, and use sophisticated tools and video equipment to operate. The MIS revolution received its impetus from technological advances in pre- and intra-operative navigation and visualisation, lower profile instruments and of course the evolution of mechanical and computerised devices now considered the gold standard in the different branches of neurosurgery (trauma, oncological, vascular and functional). Minimising human intervention during the procedure is one of the key goals for MIS. In future systems, human presence will be supervisory following the planning stage. This could facilitate complex neurosurgical interventions while

improving accuracy and reducing the overall time and cost [VRB+19].

On this regard, neurosurgery is a field that can greatly benefit from robotic solutions, not least due to the following reasons: a rich history of neurosurgical innovation in stereotaxy, a constrained anatomical environment, the microsurgical nature of procedures, a highly technical nature of the field, a need for growth in MIS and a culture that adopts and embraces new technology, according to [WJLS17]. However, general system solutions are rare, and conversion of research programs to commercially successful products has been noted to be very rare, likely due to the inherently complex nature of procedures. Early robotic neurosurgical platforms served as computer-assisted stereotactic guidance systems. Indeed the first medical robotic demonstration in 1985 used a PUMA 560 Industrial robot to guide a brain biopsy needle to a target along a straight trajectory [KHJH88]. In 1991, a later version of the system allowed the successful resection of deep benign astrocytomas in 6 children without morbidity or mortality [DJGK91].

The Renishaw neuromate® stereotactic robot was the first to obtain U.S. Food and Drug Administration (FDA) approval; this system is a 5 Degrees of Freedom (DOF) serial manipulator [LZP+02] which moves in a pre-programmed direction to a specific site defined by integrated neuronavigation systems for stereotactic biopsy or functional neurosurgical applications [DHM+95] including deployment of electrodes for Deep Brain Stimulation (DBS), stereo-electroencephalography and other stereotactic applications.

Other robotic, frameless stereotactic solutions include the Zimmer Biomet (originally MedTech) Rosa brain, a 6 DOF serial robotic manipulator designed for the accurate placement and insertion of neurosurgical tools, the Medtronic (originally Mazor Robotics) Renaissance system, a hexapod parallel robotic manipulator with 6 DOF that is directly mounted to the skull of the patient and used for DBS and biopsies, and CyberKnife [CA06]. CyberKnife is a frameless platform for stereotactic radiosurgery - a non-invasive procedure that uses precisely targeted radiation as an ablative surgical tool. It consists of a 6 DOF arm that points the medical linear accelerator (LINAC) using real-time image guidance.

Future enhancements in visualisation, tools dexterity, automation, and sensory feedback, are

expected to expand neurosurgical robots applications further. First, the user interface should be simple enough not to require specialised training to be able to plan the procedure and operate the device accordingly. This is particularly true in the case of new flexible tools which, whilst they enable neurosurgeons to overcome current surgical limitations, they might be less intuitive to manoeuvre safely. Furthermore, robots must be able to sense and automatically correct for perturbations at all phases of the intervention, thus reducing the skill level required by the surgeon to perform the procedure.

Steerable needles are at the forefront of medical robotic innovation, aiming to revolutionise the treatment of brain disease through new minimally invasive surgical techniques. Steerable needles are an important advancement in MIS techniques for the treatment of brain diseases since they can reduce brain-tissue damage [FFK+12], avoid critical structures of the brain and adjust their trajectory online for better accuracy.

1.2   Background

Percutaneous procedures, such as biopsy, brachytherapy and localised drug delivery require high accuracy and precision in reaching target locations inside the human body. The needle's insertion towards a specific target is usually difficult due to the lack of visibility, limited manoeuvrability and possible obstructions or obstacles between the starting and the target points. Performing this procedure using traditional rigid needles limits the path to a straight line, thus increasing the chance of complications due to the inability to manoeuvre around impenetrable or sensitive anatomical structures.

Several needle steering technologies have been developed in order to provide curvilinear paths within the tissue. These can be broadly classified into seven main categories: needle steering controlled using concentric tubes, also known as active cannula [WJ10, DLIB10], needle steering controlled using the lateral motion of the needle base [GS07, DS05a], flexible needle steering controlled using a fixed shape bevel tip (with and without pre-curve) [MWRO10, KC09, EMKR10], pre-curved stylet [DS05b], tendon actuated tip [RvdBvdDM15], optically controlled needle

[RQK$^+$15] and flexible needle steering controlled using a bio-inspired multi-segment needle or programmable bevel-tip (PBN) [SR13b, SKBD17]. Since then, shape memory alloy (SMA) actuated flexible needles have also been presented by [YNN$^+$18, KDH14].

Needle-based minimally invasive therapies in neurosurgery offer fertile ground for steerable needles. Steerable needles could, in fact, further improve the accuracy of these procedures while minimising surgical risks. Particularly, there is a growing emphasis on both minimally invasive and robotically assisted therapies in neurosurgery. Among these we have: stereotactic needle-based brain biopsies (SBB), deep brain stimulation (DBS), stereoelectroencephalography (SEEG), stereotactic needle-based aspiration, stereotactic brachytherapy, needle-based thermal ablation and intracerebral drug delivery (IDD). Of course, distinct surgical procedures could benefit from steerable needle technologies in different ways.

J. Burgner Kahrs et al. [BSL$^+$13] suggested that curved insertion could advance needle-based aspiration for hematomas, thus reducing the current high risk of failure, which offsets the benefits of this procedure. They hypothesise that a robot that can access the haemorrhage site through a needle-sized burr-hole and then debulk the clot from within could reduce the trauma to sensitive brain structures, currently associated with surgical decompression. To do so, they propose the use of a concentric tube robot which consists of a straight, stiff outer needle and an inner curved superelastic cannula. What makes concentric tube robots particularly suitable for brain aspiration is that, contrary to bevel-tip needles, they do not depend on tissue interaction to achieve steering. Besides, they can achieve high curvatures within the clot for dexterous aspiration.

Concerning deep brain stimulation, multiple studies are proposing steerable needles use as [HBM$^+$19, PRH$^+$16]. The main advantages are attributable to their dexterity which allows clinicians to avoid obstacles on their way towards the target region and reach it with high accuracy. In a recent study, Segato et al. proposed a computer-assisted path planner for the EDEN2020 PBN [SPF$^+$19a] for DBS Parkinson's applications which aims to achieve accurate targeting of the subthalamic brain nucleus, achieving greater simulated results with respect to currently followed straight trajectories. Also, this PBN is particularly suited for chronic

disease management since it could potentially be kept in situ for extended periods. In fact, it is entirely passive and made of a biocompatible highly flexible material which makes it compliant to possible brain soft-tissue deformations.

Similarly to DBS, brachytherapy applications demand high targeting accuracy, with the placement of radioactive seeds in specific positions proximal to the lesion under treatment. In B.Kohn et al. [KDH14], a shape memory alloy (SMA) actuated flexible needle is considered to improve this practice.

Another fascinating field of application for steerable needle technologies involves thermal tissue ablation practices. Thermal ablation is usually performed by means of a laser fibre for treating tumours and seizure-generating brain regions. Concentric tubes robots have been proposed to provide complete ablation, especially of curved anatomical structures, with respect to currently used straight catheters. Furthermore, steerable needles' enhanced flexibility offers the potential of modifying the traditional surgical procedure. For instance, Yue Chen et al. [CPC+17] suggested accessing the patient's brain through a natural opening in the skull base called foramen ovale), thus avoiding the need for a burr-hole.

Finally, steerable needles lend themselves to intracerebral drug delivery procedures. Since the blood-brain barrier (BBB) prevents the transport of most systemically delivered molecules to the brain, convection-enhanced delivery (CED) has been developed in the last decade as an effective drug-delivery approach to overcome the BBB. This is a method of drug-delivery currently undergoing clinical evaluation. It uses a positive pressure gradient to increase drug uptake in the treatment of brain tumours.

In this context, it has been suggested that the location of the needle tip with respect to the target is vitally important for the efficacy of drug delivery [ZDB19]. The targeted pose for the infusion must be optimised with respect to the patient-specific tissue properties.

However, the efficacy of the current technique is limited due to poor targeting of infusion points [SAP+10] and suboptimal delivery of catheters [MPL+11]. Innovation is taking place to overcome these failings at a system-wide level [BHW+16] and also focusing on specific problems

associated with catheterisation [GBW+13], but a radical new approach is needed to address these limitations effectively. At the same time, new imaging modalities are providing clinicians with additional tools to better plan and execute surgery, for instance by performing tractography to identify no-go functional areas [VHW+12] and to assess the extent and type of cancerous infiltration into white matter [LVR+13]. The availability of this information during therapeutic delivery is potentially life-changing but currently limited due to the loss of positional accuracy (i.e. pre vs. intra-operative feature locations) resulting from intra-operative brain shift and tissue deformation. Steerable needles, featuring a single or multiple channels, have been proposed for IDD applications [ZDB19, HAE+15] thanks to their ability to adjust the path online in response to possible deformations in order to reach a specified goal pose accurately. Particularly important in the context of this thesis is the European funded project EDEN2020 featuring a diffusion model for improved therapy planning that is expected to increase the efficacy of the drug delivery process [ZDB19].

Crucial to accurately reaching the goal pose or improving the coverage of the target area is the ability to plan optimised obstacle-free and low-risk paths. Computer-assisted planning helps to (i) automate the path selection during the pre-operative phase of the intervention; (ii) minimise patients' risk by generating safe paths at a predefined minimum distance from sensitive structures; (iii) improve patients' outcomes by proposing paths that optimise important surgical metrics. Computer-assisted planning, together with intra-operative planning are both widely researched topics for steerable needles. The latter exploits the flexibility of steerable needles in being able to adjust a pre-operative trajectory on-the-go, if needed.

However, planning for an appropriate three-dimensional (3D) insertion path for a flexible needle can be particularly challenging. This is due to factors like kinematic constraints of the considered catheter, the presence of complex anatomical structures such as the brain network, and surgical constraints dependent on the specific application (i.e. entry and target pose conditions).

Different kinds of path planning algorithms have been used in the context of steerable needles. It is also observed that, since Xu et al. [JDAG08] first applied the most common sampling-based

path planning method called Rapidly-exploring Random Tree (RRT) to search for valid needle paths in a 3D environment, RRTs have become the most common path planner technique for steerable needles technologies. However, these algorithms have often been tested with simple geometrical obstacles, which is a poor representation of a realistic anatomical environment [VAP+14, ZWZ+, PBWA14]. Furthermore, they generally do not include needle curvature constraints and target orientation accuracy is mainly not considered. Only recent RRT spline-based solutions are able to meet constraints on both a specified target orientation and on a maximum curvature radius, without requiring further smoothing [YMY+14, FSM18a]. However, these solutions cannot easily be extended to higher curvature constrained needles since they are limited by their geometrical approach which, as in the case of Dubin's curves, bound the maximum curvature radius up to half the distance between the start and target point [FSM18a, Moh15]. RRT-based methods featuring very low computational time have also been proposed for intra-operative use [PBWA14]. However, local methods, aiming for pre-operative path adjustment instead of full re-computation could achieve much greater stability from which intra-tissue applications could benefit [ZSP15, WJLS17]. Therefore, a comprehensive computer-assisted planning method should be able to meet new constraints deriving from precision neurosurgery applications and adjust the selected path online during the insertion, compensating for deviations of the tip and tissue deformations with excellent stability. Path planning methods for steerable needles are reviewed extensively in Chapter 2.

1.3 Objectives

- To assist surgeons during the pre-operative phase of procedures requiring high accuracy on the final goal pose, which includes both target position accuracy and target orientation accuracy.

- To propose a computer-assisted planner for steerable needles that can generate safe and feasible paths according to neurosurgeons preference.

- To propose an intra-operative solution which compensates online for tissue deformations

and deviations from the pre-operative path.

- To demonstrate the *ex-vivo* and *in-vivo* performance of pre-operative and intra-operative path planning methods.

- To explore a novel application for steerable needles in neurosurgery and demonstrate curved potential trajectories over straight ones through a retrospective study.

1.4   Research Problem

The main research problem tackled by this thesis is an investigation into path pre-operative planning and online re-planning in the context of steerable needles. This is achieved through the development of a computer-assisted planning technique meeting both the kinematic constraints of a flexible needle and the surgical constraints of a precision neurosurgery intervention which, as for IDD, demands high accuracy on the goal pose. Furthermore, its integration within the EDEN2020 robotic suite (www.eden2020.eu) allowed testing of its performances during *ex-vivo* and *in-vivo* trials on ovine models. Then, a novel optimised pre-operative planning method for thermal ablation purposes is proposed, which can maximise target area coverage and minimise the risk of damage along with a curved insertion. This has been evaluated through a retrospective study done on epilepsy patients, demonstrating the potential of steerable needles for this type of surgical procedure.

1.5   Contributions

This thesis makes the following novel contributions:

- Multi-threading and GPU-based parallel processing methods are explored to implement pre-operative planning tools that, given a goal pose and a PBN, can aid surgeons in mapping corresponding feasible access areas on the patient's skull.

- A computer-assisted planning (CAP) algorithm for steerable needles is implemented, which takes into account patient-specific anatomy, PBN geometrical constraints, and functional clinical requirements, such as preferential drug delivery target orientation (resulting from studies on the microstructure of the brain tissue) and surgeon preference.

- An intra-operative planner for steerable needles is proposed. Online trajectory adjustments are successfully performed to compensate for tissue deformation, needle-tissue interaction, and needle deviations from the planned path (e.g. due to surgeon error during the servo-assisted insertion of the needle).

- Both the computer-assisted planner and the intra-operative planner are integrated into the EDEN2020 robotic suite and *ex-vivo* and *in-vivo* tests are performed on ovine models.

- A new potential application of the EDEN2020 technology for thermal ablation for epilepsy procedures is proposed, together with an ad hoc CAP method for steerable needles that optimises coverage and reduces damage to sensitive structures.

1.6 Research Strategy

The research presented in this dissertation is applied. Numerous pieces of previous academic research exist regarding path planning for steerable needles, not only within a neurosurgical environment but also extended to other organs, soft-tissues and cavities. As such, the proposed research took the form of new research tackling the navigation of follow-the-leader deployment of steerable needles for the specific application of precise neurosurgery, based on existing literature.

1.7 Research Approach

This dissertation makes use of a quantitative research strategy, where the aim is to classify features, count them, and construct statistical models in an attempt to explain what is observed. In quantitative research all aspects of the study are carefully designed before data is collected in

the form of numbers and statistics. Furthermore, the experimental research approach has been implemented. In this approach, a test is performed in a controlled environment and specific data are collected from it. This type of data is used for a situation in which variables are controlled and manipulated to establish cause-and-effect relationships. Every technical chapter of this thesis features a methodology section providing information on the specific experiment design, tools, techniques and procedures used to conduct the tests.

1.8 Data Collection Methods and Tools

For the purpose of this thesis, we decided to mainly use computational simulations methods (Chapter 3, 4, 5, 7) in combination with lab experiments (in-vitro tests, Chapter 5) and on field experiments (ex-vivo animal tests, Chapter 6).

With the advent of large-scale computers, computational approaches have become indispensable for characterising, predicting and simulating real-world events and engineering systems. From the point of view of scientific investigations, one of the great strengths of computer simulations over experiments in the lab, is the ability to study a complete range of parameters and analyse their influence within a simplify simulated environment. Particularly in autonomous robotics, computer simulations can cut research cost and time, providing a low cost and easy accessible environment for the development of robotics software.

In addition, simulation can be an important intermediate step between the creation of an algorithm and the testing in a real world scenario. Since a simulated environment is controllable, troubleshooting a "misbehaving" algorithm is simplified due to less factors playing part in its final performance. Furthermore, a simulated environment is not unpredictable which ensures the reproducibility of research. A question could be raised about the transferability of simulated performance into a real world scenario, where many more factors are involved, which warrants the careful use of experiments to corroborate simulated findings.

Lab and on field experiments (Chapter 5) have thus also been performed in the context of this thesis. During lab experiments the environment was controlled and the independent variables

could be manipulated to study cause and effect relationships. Lab experiments offer high internal validity, which makes them superior to field experiments. However, this may lead to a lack of ability of generalisation to the real world.

Finally, field tests were carried out to evaluate the integration (Chapter 6) of the proposed algorithms within a real-world scenario and measure the influence of real-world uncertainties on the final performance.

1.9 Publications

During the course of the PhD, the following papers were published. This thesis contains edited versions of these publications; where material used is from modified versions of a publication, it is detailed at the start of the corresponding chapter.

- Marlene Pinzi, Stefano Galvan, and Ferdinando Rodriguez Y Baena, "Surgical Planning and intra-operative Navigation", Poster presentation at *ERF 2017, European Robotics Forum*, March 2017

- Marlene Pinzi, Stefano Galvan, Wenbo Zhan and Ferdinando Rodriguez Y Baena, "Towards an Optimized Path Planner for the EDEN2020 Neurosurgical Steerable Needle",*Hamlyn Symposium on Medical Robotics Conference*, June 2017

- Marlene Pinzi, Stefano Galvan, and Ferdinando Rodriguez Y Baena, "Adaptive Fractal Trees Parametrisation for Neurosurgery Applications", *7th Joint Workshop on New Technologies for Computer/Robot Assisted Surgery*, September 2017

- Marlene Pinzi, "Pre-operative and intra-operative Path Planning for Steerable Needles", Invited Speaker at *Robotics at Leeds Conference*, September 2018

- Marlene Pinzi, Stefano Galvan, and Ferdinando Rodriguez Y Baena, "The Adaptive Hérmite Fractal Tree (AHFT): a novel surgical 3D path planning approach with curvature and heading constraints." *International Journal of Computer Assisted Radiology and Surgery*, vol. 14, no. 4, pp. 659–670, April 2019

- Marlene Pinzi, Riccardo Secoli, Tom Watts, Stefano Galvan and Ferdinando Rodriguez Y Baena, "Path Replanning for Orientation-constrained Needle Steering" *IEEE Transactions on Biomedical Engineering*, under the second review

- Riccardo Secoli, Eloise Matheson, Marlene Pinzi, Stefano Galvan, Tom Watts, Abdul Donder, and Ferdinando Rodriguez Y Baena, "A Modular Robotic Platform for Precision Neurosurgery with a Programmable Bevel-Tip Needle" *The International Journal of Robotics Research*, under review

- Marlene Pinzi, Vejay Vakharia, Brian Hwang, William Anderson, John Duncan and Ferdinando Rodriguez Y Baena, "Computer Assisted Planning for Curved Laser Interstitial Thermal Therapy" *IEEE Transactions on Biomedical Engineering*, under review

1.10 Thesis Structure

Chapter 2 presents a review of path planning algorithms used in the field of steerable needles and more specifically, the evaluation of their performances with different user-defined constraints and experimental setups. The relative merits of different approaches are considered in order to justify the subsequent research choices.

Chapter 3 develops a pre-operative path planner tool for steerable needles with the purpose of mapping the patient's skull and aid with entry point selection in a easy and interactive way. The tool will allow clinicians to visually map the patient skull, highlighting those regions from where safe and feasible paths can be followed.

Chapter 4 validates a pre-operative path planning algorithm able to cope with the kinematic constraints of a steerable needle and predefined start and target poses. Its performance to target pose migration and rotation are assessed in simulation.

Chapter 5 introduces an intra-operative path planning algorithm based on the concept of "elastic bending" methods able to adjust the pre-operative path online, compensating for deviations at the tip of the needle and environmental changes. In-vitro experiments with a 4-segment PBN

demonstrate its potential to be applied either to user-controlled steering or in semi-automatic needle steering frameworks.

Chapter 6 presents the integration of the discussed pre-operative and intra-operative planning algorithms into the EDEN2020 system, a neurosurgical platform which targets drug delivery for treatment of glioblastoma. The system is presented along with performance evaluation.

Chapter 7 proposes the application of a novel computer-assisted planning method to laser interstitial thermal therapy (LiTT) for maesial temporal lobe epilepsy. This is the first quantitative evaluation of an optimised patient-specific technique for curved LiTT insertions. Results confirm the potential of steerable needles for LiTT neurosurgical purposes.

Chapter 8 concludes the thesis, stating the achievements of the research with respect to the initial hypotheses. It discusses the wider context within which the thesis was conducted and presents opportunities for future study.

Chapter 2

Literature Review

2.1 Path Planning for Steerable Needles

Path planning algorithms are a major point of study in the robotic field. Their aim is the generation of a feasible path from a starting point to a target point, which avoids search space obstacles. However, the main issue, especially in the field of steerable needles, is not the generation of an obstacle-free trajectory but its characteristics of smoothness and curvature which are strongly limited depending on the application. Furthermore, the path planning environment can be either static or dynamic. For the static environment, the whole solution can be found before starting execution. However, for dynamic or partially observable environments, replanning is required frequently and more update time is needed.

There are many studies on robot path planning using various approaches, which are broadly classified into search methods and numerical methods, as outlined in this section (Fig. 2.1). The first category includes those strategies in which the topology of the total environment has to be considered. They rely on capturing the topology of the environment and synthesizing it, either in a graph (A star, visibility graph, Voronoi diagram, etc.) or in a tree connecting the start to the goal position as for sampling-based methods (Rapidly-exploring Random Trees, Probabilistic Road Maps, Adaptive Fractal Tree etc.). Classic strategies using artificial potential fields (APF) are also included.
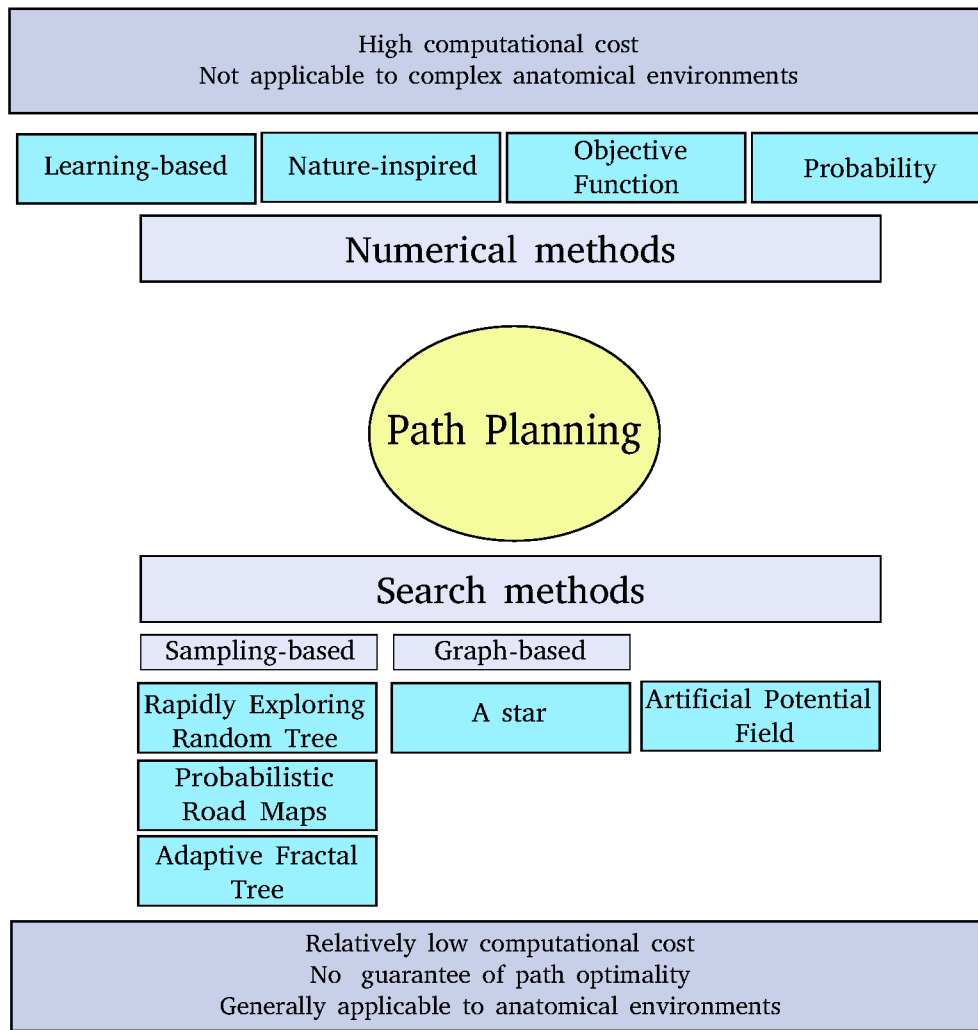
Figure 2.1: Path planning methods classification. The most common techniques used for needle steering applications can be divided into three categories: numerical methods, sampling-based methods and graph-based methods.

Numerical methods, on the other hand, are based on mathematical optimisation and they include learning based methods, nature-inspired methods, probability methods and objective function methods. They are in general local or reactive approaches which can exploit sensors information to adapt the initial path calculated by the global planner to unforeseen situations like the appearance of obstacles.

Finally, the concept of real-world uncertainty in path planning problems is introduced and the most relevant intra-operative path planning approaches for needle steering, developed between 2013 and 2020, are discussed.

2.1.1   Search methods

Graph-based strategies

Graph based path planning algorithms perform optimisation based on an array of nodes generated by discretisation of the problem space [YQS$^+$16]. Graph-based methods are *resolution-complete*, meaning that, at the chosen resolution, they are guaranteed to find a solution, if one exists. In addition, they are also *resolution-optimal*, meaning that they can find the optimal solution, among the existing ones, at the chosen resolution. Thus, optimality is guaranteed inside the limits imposed by the discretisation of the domain.

A star (A*) is the most well-known graph based method for path planning. It was developed by Peter E. Hart, Nils Nilsson and Bertram Raphael in 1968 [HNR68]. The authors extended the well known "Dijkstra's algorithm" which aims at finding the shortest path between a node and all other nodes in a weighted graph. In particular, it can generate the shortest path from a starting node to a destination node. However, a critical drawback of Dijkstra's algorithm is that it does not consider any information about the target location, thus expanding in every direction of the search space. A* is a modified version of Dijkstra's algorithm, improved to overcome the aforementioned limitation. A* reduces the number of the graph nodes explored, by using a heuristic leading to the target. Hence, A* algorithm is generally much faster to run than Dijkstra's algorithm. In particular, it combines features of uniform-cost search and pure heuristic search to efficiently compute optimal solutions. It follows that the cost associated with a node is $f(n) = g(n) + h(n)$, where $g(n)$ is the cost of the path from the initial state to node n and $h(n)$ is the heuristic estimate or the cost of a path from node n to a goal. Thus, $f(n)$ estimates the lowest total cost of any solution path going through node n. At each point a node with the lowest f value is chosen for expansion. The algorithm terminates when a goal is chosen for expansion.

Search space partition techniques can be used in combination with graph based path planning. Generally, these methods produce a set of possible paths and a search algorithm such as A* must be used for selecting the optimal route. For instance, Voronoi diagrams have been pro-

posed in the field of path planning to maximise the margin for error while navigating between obstacles. A similar approach by Bhattacharya and Gavrilova [BG07] has been used to generate a simplified roadmap of the environment, also reducing the computational complexity of the path optimisation task. Similarly, visibility graphs are an illustration of intervisible points between obstacles. Like Voronoi diagrams, they create a simplified roadmap of the environment [LSLL98]. This method has been used with success for UAV path planning [Bin11] when knowledge of the environment is complete.

However, the main drawback of the A* algorithm is its memory requirement. Since the entire node array must be saved, A* is severely space-limited in practice. Mohamed et al. [Moh14] introduced a new variant of the A* algorithm, which they state could be applied in a typical needle based surgery. They implemented an octagonal division for the environment which resulted in not only bigger obstacle avoidance sensivity and smoother paths but also reduced computational time with respect to the orginal A* version. However, only preliminary results have been shown: average computational time is not provided and the algorithm assessment, specially in the context of needle based surgery, is very poor.

To conclude, A* based methods are able to effectively find paths with obstacle avoidance, but the search is excessively time consuming. Thus, in practical path planning systems, as in the context of robotics, it is generally outperformed by algorithms which can pre-process the graph to attain better performance as well as memory-bounded approaches.

Artificial Potential Fields

The artificial potential field (APF) method proposed by Khatib [Kha] is a popular approach for implementing real-time obstacle avoidance. The APF algorithm is based on artificial forces generated by the search space and applied to the robot. In particular, repulsive forces and attractive forces are assigned to the obstacles and goal position respectively. For each point of the search space it is possible to calculate an artificial potential value due to the contribution of the attractive potential pulling the robot towards the target and the repulsive one pushing the robot away from obstacle regions. The robot is, therefore, attracted to the goal position

and repulsed from the obstacles in the environment. Since this capability is achieved without costly representations of the free-space, there has been much interest in adapting the potential field method to path planning.

With regard to medical applications, DiMaio and Salcudean [DS05b] proposed a potential-field-based path planning technique for needle steering tested in a geometrical environment.

However, the main disadvantages of APF methods are that trap situations can occur due to the presence of local minima in the potential, thus limiting their use in congested environments such as anatomical ones. Li et al. [LJYY] came up with a possible approach to overcome this issue which relies on an APF method in conjunction with an improved conjugate gradient algorithm (ICGA). This technique was tested in a static geometrical simulated environment, resulting in higher efficiency (13.45% higher) compared to APF method. Future Li et al. [LJL$^+$17a], give an example of an APF algorithm used in medical instrument static trajectory planning. Simulation of prostate brachytherapy using an organ group mockup (OGM) of the pelvic cavity is performed. The puncture needle always moves from a high potential point to a low potential point; the needle motion is in the minimum potential direction while the goal is the point of lowest potential. However, the APF algorithm is only used to generate a preoperative reference path while is the path tracking controller that constantly guides the needle during the insertion.

It can be concluded that although APF algorithms have a reasonable time solution, they shows poor ability to overcome the local minima trap and provides non-optimal results. Finally, their poor performance in narrow passages and complex dynamic environments makes it difficult to implement them in a real-world application.

Sampling-based methods

Sampling-based methods do not require an a priori discretization of the domain but progressively sample the space, increasing the accuracy of the solution as the search progresses. In contrast to graph-based methods, sampling-based methods do not explicitly characterize the free space and the obstacles space, but generate solutions and then check their feasibility through

a collision detector.

- Rapidly Exploring Random Tree

  The rapidly exploring random tree (RRT) method is a very common sampling-based method that was first proposed by La Valle [Lav06]. RRTs rapidly search the configuration space to generate a path connecting the start node and the goal node. The configuration space consists of two parts, a fixed obstacle region, which must be avoided, and an obstacle-free region, where the robots must stay. RRT methods are based on a random sampling of the search space that allows to create a tree which expands towards the obstacle-free directions. In order to implement a basic RRT algorithm, the following steps should be obeyed:

  1. the initial collision free state x is selected as the first vertex. Then, a state $xrandom$ is randomly chosen in the free space.

  2. the nearest state $xnear$ to the newly generated state $xrandom$ is selected based on a certain metric (mostly an Euclidean metric) which is already designed. $xnear$ is considered as the parent state with respect to $xrandom$.

  3. $xrandom$ is the state which shows the direction where the next step should go but may be beyond the robot's reachability. Thus a control input factor is added, considering the kinodynamic constraints, in a cost function $gm = f(x, y, z)$ form. Then according to the constraints r and cost function gm we get the reachable state $xnew$ which is first checked for collisions and then added to the path.

  RRT produces very cubic graphs. This is expected as nodes are attached to their nearest neighbor. The structural nature of these graphs hinders the probability of finding an optimal path. RRT-based algorithms are not asymptotically complete, meaning that convergence to the optimal solution is not guaranteed.

  RRT* is a modified version of RRT able to converge towards an optimal solution. The main difference with RRT, is on how a new point is connected to the growing tree. First, RRT* records the distance each vertex has traveled relative to its parent vertex. This is

referred to as the cost of the vertex. After the closest node *xnear* is found in the graph, a neighborhood of vertices in a fixed radius from the new node are examined. If a node with a cheaper cost() than *xnear* is found, the cheaper node replaces *xnear*. The second difference RRT* adds is the rewiring of the tree. News states are not only added to a tree, but also considered as replacement parents for existing nearby tree states. With uniform global sampling, this results in an algorithm that asymptotically find the optimal paths from the initial state to every state in the problem domain. However, this is inconsistent with path planners' single-query nature and becomes expensive in high dimension.

RRT and RRT* planners generally have large computational time and cannot deal with changing environments where the obstacles are not in a fixed position. Furthermore, they can suffer from a lack of control in orientation, residual position errors and curvature discontinuities. On the other hand, sampling based methods and specially RRTs have been extensively explored, integrating them with different strategies in order to guarantee the compliance to kinematic constraints while reducing computational time.

Xu et al. were the first to create a variant of RRT for needle steering [JDAG08] which takes into account the kinematic constraint of a flexible catheter. Their implementation was only tested with simple 3D spherical obstacles and it is too slow for closed-loop implementation (average of 621.4 across 10 trials). In the recent literature several attempts have been made to produce needle steering RRT-based planners that act online during a procedure to correct for needle positioning errors. Different methods to speed up the convergence of the algorithm and allow its intra-operative use have been evaluated. Patil et al. [PBWA14] demonstrated a RRT based planner for rapid replanning and controlling of a concentric tube steerable needle in 3D, with a computational time bounded at 1 second per replanning step. Variable curvature arcs are used to compose the trajectory and a reachability-guided sampling heuristic (RG-RRT) is introduced to reduce the execution time of the algorithm. This method differs from standard RRT in the choice of the new random point at each iteration: while in RRT the new point is sampled randomly from the search space, in RG-RRT, the allowed space for sampling is limited to the region of space accessible to the needle, according to its kinematic constraints. A similar approach

was also applied in Vrooijink et al.'s study [VAP+14]. The reachability-guided sampling allows the search tree to grow efficiently, thus reducing the run time to a fixed planning time bounded at 0.6 seconds and, therefore, allowing its online application.

A simple modification of RRT* that demonstrates order-of-magnitude improvements in complex obstacles environments is represented by Informed RRT* methods. These behave as RRT* until a first solution is found, after which it only samples from the subset of states defined by an admissible heuristic to possibly improve the solution [GSB]. Informed RRT* has also been recently used in neurosurgical applications [SPF+19a] in combination with an evolutionary optimization procedure for path smoothing and refining. Although, this technique features a high computational time varying between 1 to 3 min, thus limiting its potential to preoperative path planning.

On the other hand, different RRT and RRT* solutions have been developed with the aim of generating paths within the required curvature boundaries. Recently, Hong et al. [HBM+19] incorporated the physical constraints of a flexible needle directly within an RRT*-based algorithm. Three-dimensional Dubins curves [HG10] have been coupled with a RRT*-based method [PHB17] to aid the process in the case that start and goal regions are sufficiently far away. This approach has been originally proposed for aerial vehicles (UAV) such as drones but could be applicable to steerable needles technologies. With the same purpose, spline-based RRT methods can deal with differential constraints directly in the global planner, removing the need for a refinement process. In particular, curvature bounded cubic Bézier splines have been used as local planner to connect two states of the RRT search tree [YMY+14]; in Yang et al. simulation and experimental results of a mobile robot efficiently navigating through a 2D cluttered environment are presented.

Finally, the RRT-Connect algorithm has been proposed as an enchanced version of the RRT, which involves the parallel growth of two trees [KS00]. These methods, unlike basic RRTs, grow search trees from both the goal and the initial region in an attempt to connect these two and take into account both start and target pose constraints. With this strategy, more possible connections are available than just those between search tree

and goal regions. Thus, successfully finding an access path is more likely.

An optimised version of this technique has been very recently introduced in the context of nonholonomic steerable needles technologies for surgical applications requiring high precision with start and goal regions in $SE(3)$ [FSM18b]. These tailored RRT-Connect algorithms outperform state-of-the- art one-directional planners and provide a reliable and fast method (with a computational time bounded at 0.5 seconds) for planning access paths in temporal bone surgery. In contrast to the standard RRT-Connect, the proposed k-RRT-Connect imposes orientation constraint at the start and target state. It also overcomes the common shortcoming of the RRT-Connect method to show discontinuities at the intersection of the two trees. Nonetheless, the implemented connection techniques work only for bounded curvature values that are not always generalizable to existing steerable needles constraints.

To conclude, sampling-based motion planning algorithms such as rapidly exploring random tree planners have been effective for a broad range of robotics problems including needle steering. However, a common issue in most existing path planning approaches, including RRTs, is that the algorithm performs the search sequentially, relying on a single CPU, a fact that imposes a considerable lower bound on computation time and cost. For this reason, the design of real-time path planning algorithms capable of online updates is very challenging and a trade-off between computational time and solution optimality needs to be taken into account.

- Adaptive Fractal Tree:

  The Adaptive Fractal Tree (AFT) [LGCSR16] is an innovative algorithm characterised by the expansion of a self-similar (fractal) structure through the search space. Each branch of the tree is associated to a GPU thread and runs in parallel on the graphic card, thus optimising the use of computational resources. The topological structure of the tree resembles the recursive nature associated to the motion of nonholonomic needles. At each step, all possible future motions depend on the current pose, a process that reverses recursively from the target to the insertion point via all tree levels. The basic

tree structure with this fractal geometry features five possible motion directions: straight, up, down, right and left, represented by a straight line in the first case and arcs for all remaining cases, the curvature value of which can be chosen based on the needle's constraints. The search space between the straight line and the maximum curvature arcs can be explored by adding further arcs featuring lower curvature. The ability to consider straight line segments in addition to the curvilinear ones may both shorten the length of path and save the cost of control and energy for the active needle. Moreover the curvature is not considered as a constant, which would severely restrict the range of motion of the needle tip, making it difficult for planners to compute a feasible motion plan in 3D environments with obstacles. Because of its specific structure, the AFT is able to produce paths that comply with the maximum curvature constraints. The density of the fractal structure, which grows exponentially with the level of the tree, enables the generation of several collision-free paths even in cluttered environments. Then, an optimised trajectory can be selected minimising a cost function based on the needle preferential requirements, such as low curvature values and the absence of inflection points.

The results of a simulation of 100 different AFT path planning problems in a prototypical scenario are discussed in the study conducted by Liu et al [LGCSR16]. The average computation time is 5.15 ms, with a corresponding standard deviation of 0.048 ms. The small variation in computation time between the different simulations is a result of the automatic speed adjustment of the GPU. However, the computation time is fixed and independent of the complexity of the obstacles. This represents a significant advantage of AFT in surgical applications. In comparison, a standard RRT implementation performs considerably worse than the AFT. The RRT simulation performed on the same dataset and with the same setup indicates that, after 16,000 iterations (corresponding to an approximate computation time of 30s in our, non-optimized implementation), a path was found in 42% less cases than in AFT.

A "parallelisable" path planner, such as the AFT can cope with the catheter nonholonomic constraints and enable successful real-time path computations even in complex surgery. However, precise surgical constraints on start and target pose cannot be included and the

desired target position is reached only within a predefined minimum accuracy.

- Probabilistic Road Maps:

The Probabilistic Road Maps (PRM) motion planning problem is normally formulated in terms of the configuration space C, the space of all possible placements of the moving object. Each degree of freedom of the object corresponds to a dimension of the configuration space. Each obstacle in the workspace, in which the object moves, transforms into an obstacle in the configuration space. Together they form the forbidden part C_{forb} of the configuration space. A path for the moving object corresponds to a curve in the configuration space connecting the start and the goal configuration. A path is collision-free if the corresponding curve does not intersect C_{forb}, that is, it lies completely in the free part of the configuration space, denoted with C_{free}.

The probabilistic roadmap planner samples the configuration space for free configurations and tries to connect these configurations into a roadmap of feasible motions. There are a number of versions of PRM, but they all use the same underlying concepts. These free configurations form the nodes of a graph. A number of (useful) pairs of nodes are chosen and a simple local motion planner is used to try to connect these configurations by a path. When the local planner succeeds an edge is added to the graph. The local planner must be very fast, but it is allowed to fail on difficult instances. A typical choice is to use a simple interpolation between the two configurations, and then check whether the path is collision-free. This will result in a straight line path connectors in the configuration space. Once the graph reflects the connectivity of C_{free} it can be used to answer motion planning queries.

The PRM assumes that the collision-free connectivity of states is specified using boolean values rather than distributions. Alterovitz et al. [ASG] relaxed this assumption and combined a roadmap representation of the configuration space with a stochastic model of robot motion capable of generating samples of the next configuration given the current configuration and an action. They applied this method to static needle steering, to find a path which maximise the probability that the robot will successfully reach the goal under

uncertainty.

To summarise, PRM algorithms rely on the construction of a good road map that can take up to few minutes for complex environments. Planning queries are then processed very fast. The very small query time make PRMs particularly suitable for robots performing several point-to-point motions in a well known static workplace. Furthermore, similarly to basic RRTs, are only probabilistically complete and the resulting trajectory can be very jerky and unnatural.

2.1.2 Numerical methods

2.1.3 Nature-inspired

A considerable number of researchers tried addressing the problem of mobile robotics path planning and obstacle avoidance using optimization algorithm techniques that imitate the behavior of some living things including bees, fish, birds, ants, flies etc. These algorithms are referred to as nature-inspired and has been applied in engineering to solve research problems including path planning. Nature-inspired computation-based methods are able to solve complex problems that are characterized with imprecision, uncertainty and partial truth to achieve practical and robust solutions. Notwithstanding the strengths discussed above, there are some weaknesses of nature-inspired path planning methods, some of which include trapping in local minima, slow convergence speed, premature convergence, high computing power requirement, oscillation, difficulty in choosing initial positions, and the requirement of large data set of the environment which is difficult to obtain. Notable among nature-inspired methods used in path planning and obstacle avoidance research include artificial neural networks (ANN), genetic algorithms (GA), simulated annealing (SA), ant colony optimization (ACO), particle swarm optimization (PSO), fuzzy logic (FL) and artificial bee colony (ABC), however the focus of this section will be on GA ans PSO, being the ones have been recently applied to the surgical planning context.

Genetic Algorithms The Genetic Algorithms belong to the larger class of evolutionary algorithms (EAs) and they have demonstrated to be effective procedures for solving multi-criterion

optimization problems. These algorithms mimic models of natural evolution and have the ability to adaptively search large spaces in near-optimal ways. They use three main types of rules at each step to create the next generation from the current population:

1. Selection rules select the individuals, called parents, that contribute to the population at the next generation.

2. Crossover rules combine two parents to form children for the next generation.

3. Mutation rules apply random changes to individual parents to form children.

GAs have been used for path planning problems [Ach11, CKB$^+$17]. The first step of GAs consists of generating an initial population of chromosomes. In [CKB$^+$17], each chromosome represents a path. The robot path is encoded as a sequence of free cells. It begins at a start cell and finishes with the goal cell joined by a set of intermediate cells. To generate the remaining paths in the initial population, the algorithm will choose random intermediate cells, not in the initial path, which will be used to generate a new path from start to goal cells across the selected intermediate cell. After the generation of the initial population, each path is evaluated and ranked. The fittest paths are selected to form the current generation. By selecting solutions which have a high fitness score and iterating the re-combination process a large number of times, further improved solutions are developed. In a recent study [SPF$^+$19a], an EA algorithm has been used for the final smoothing phase of a deep brain stimulation computer-assisted RRT-based planning algorithm. However, the long computation time of EA algorithms and their difficulty to independently find a solution in complex environments represent an issue for potential surgical applications.

Particle Swarm Optimization (PSO) Particle swarm optimization (PSO) is a computational method that optimises a problem through iteratively improvement of a candidate solution with respect to a given metric. It solves a problem by having a population of candidate solutions and moving these particles around in the search-space according to simple mathematical formulae over the particle's position and velocity. Each particle's movement is influenced by its local best known position, but is also guided toward the best known positions in the search-space, which

are updated as better positions are found by other particles. This is expected to move the swarm toward the best solutions. PSO is originally attributed to Kennedy et al. [KE] and it was first intended for simulating social behaviour such as the movement of organisms in a bird flock or fish school. PSO has been recently used in three-dimensional path planning for flexible needle puncturing applications [CSHZ20]. In this context two variables are defined as particles: the values of the center angle of each arc constituting the path and the angle of rotation of the needle body between adjacent arcs. With the two variables and radius of the arc, the coordinates of any point on space arc are finally calculated. PSO is shown to be simpler and more versatile than RRT in finding solutions for a simplified flexible needle puncturing application. In addition, parameters of PSO can be easily adjusted when the boundary conditions change. the path can be obtained by changing the most basic elements of the path, such as the length of each arc and the angle between adjacent arcs.

However, this method is limited to very simple trajectories relying on a small set of parameters. More complex trajectories are usually desired in order to successfully find obstacle-free solutions within cluttered anatomical environments.

Learning Based Approaches

Neural networks deal with cognitive tasks such as learning, adaptation generalization and they are well appropriate when knowledge based systems are involved. Thus, several approaches based on neural networks for autonomous mobile robots are oriented to design and achieve robots which simulate the human decision-making in similar way of acquiring some keys of intelligence. In designing a neural networks navigation approach, the ability of learning must provide robots with capacities to successfully navigate in the environments. Also, robots must learn during the navigation process, build a map representing the knowledge from sensors, update this online and use it for intelligently planning and controlling the navigation. Reinforcement Learning (RL) techniques have recently extended his used to the path planning domain. Sadati et al. [ST09] made use of a Lyapanov energy function of a Hopfield neural network to optimise a bevel-tip needle insertion under soft-tissue deformation.

Reinforcement learning path planning methods have been also applied to underwater autonomous vehicle [YK16] demonstrating their potential to reduce the time needed to compute an optimal path with respect to more conventional path planners (RRT, A*). Furthermore, they can account for the non-holonomic nature of a system, thus not requiring for a path smoothing process after a route has been determined. In the context of minimally invasive neurosurgery, a recent study [SSCD] presents a grid path planning method using GA3C Deep Reinforcement Learning trained on a dataset of continously changing maps and targets, in order to guarantee high generalization in learning. When tested against the standard A* and RRT* algorithms, the proposed method performs better in terms of trajectories smoothness and clearance from safety regions but with significantly increasing length. In addition, failures start occurring when the complexity of the map increases, especially when dealing with new maps with severe differences from the ones the method was trained on. Computational time is also very dependant on the considered environment.

To conclude, reinforcement learning path planning methods are still not applicable to complex environments or real-time applications, although they have a strong potential to be the future of path planning research.

Probability Methods

Markov Decision Process (MDP) is an analytical tool that provides a mathematical framework for modeling decision making in situations where outcomes are partly random and partly under the control of a decision maker. The planning problem has also been formulated as a Markov Decision Process (MDP). In the case of motion planning for steerable needles, robot's motion uncertainty is represented by soft-tissue interactions. The search space is discretised and probability distributions are used to model robot's motion uncertainty. Then, optimal actions (within error due to discretisation) are computed for a set of feasible states using dynamic programming (DP) which is an optimisation method for recursive solutions having repeated calls for the same inputs.

Alterovitz et al. [ABG, ALG+05, ASG08] developed a motion planner computing optimal steer-

ing actions which maximises the probability of reaching the desired target, with the capability of considering uncertainty in the insertion due to patient-specific differences. In [WA14], the path planning problem is devised as a Partially Observed Markov Decision Process (POMDP). This method enforces collision avoidance in the trajectory optimization process and generates a locally optimal path. The local optimization is done directly in belief space. The belief state is the probability distribution over all allowable needle state given sensor measurement and past control inputs. The assumption made is that Gaussian distribution could be a reasonable estimation of the belief state, therefore a noise which has been sampled from a Gaussian distribution with zero mean is added to the motion uncertainty model.

Tan X et al. presented an extension of previous MDP needle steering planners called Enhanced MDP [TYLC18]. The authors claimed that the uncertainty probability prediction has been oversimplified, producing inaccurate assumptions to the complex tissue-needle interaction. In particular, using one transition probability to represent a range of uncertainty in needle–tissue interaction is not sufficient in practical applications. As the non-homogeneous property of the tissue could cause the uncertainty of tissue deformation to vary greatly between an upper and lower boundary, they propose to model the uncertainty with a normal distribution.

However, the accurate estimation of the needle tip pose is hard to achieve as the needle motion and the sensory model are stochastic. Also, limitations in predicting the needle–tissue interaction under the influence of multi-layer tissues and the difficulty to collect such data reduce MDP-based applications.

Objective function methods

Objective function path planning methods are based on mathematical optimisation techniques. Alterovitz et al. [AGO05] developed a motion planner for steerable bevel-tip needles that combines numerical optimization with soft tissue simulation to generate a 2D optimal obstacle-free trajectory plan which compensate for simulated tissue deformations. Similarly, Duindam et al.[DASG08] proposed a path planner which makes use of a discretized control space to be able to express the needle trajectory analytically without approximate numerical simulation.

This method can find a locally optimal trajectory in a 3D environment with obstacles with just a few seconds of computational time. However, Duindam et al.'s methods benefits for a low computational time it treats collision avoidance as a cost and not as a hard constraint. Schulman et al. [SDH^{+}14] formulate a 3D needle steering planner as a constrained non-convex trajectory optimisation problem. To do so they define the problem over manifolds in the $SE(3)$ Lie group instead of using vectors in the real coordinate space. The pathway generated is curvature constrained and locally optimal. The method considers both kinematic constraints, maximum curvature constraints and obstacle safety margins as hard constraints, while the proposed cost function minimises path length and needle steering-induced tissue damage.

However, sequential convex optimization cannot solve difficult path planning problems, and the probabilistic completeness is not ensured. Additionally, its performance strongly depends on the path initialisation choice and the obstacles avoidance is in general not guaranteed.

2.1.4   Path planning under uncertainties

Whereas many traditional path planners assume a robot's motions are perfectly deterministic, a needle's motion through soft tissue cannot be anticipated with certainty due to patient differences and the difficulty in predicting needle-tissue interaction. Furthermore, in clinical settings it is typically difficult to precisely sense the pose of the needle tip.

Motion planning for needle steering is challenging because the needle is a nonholonomic and underactuated system, the needle's motion may be perturbed during insertion due to unmodeled needle/tissue interactions, and common intra-operative imaging modalities such as ultrasound and x-ray projection imaging typically provide only noisy and partial state information.

Since the motion response of the needle is affected by different sources of uncertainty, success of the procedure can rarely be guaranteed. Therefore, if we consider a dynamic environment that presents tissue and anatomical structures displacement due to patient motion or breathing, the use of pre-computed paths may not be appropriate.

As explained in Section 2.1.3, Alterovitz et al. [ABG] developed a new motion planning ap-

proach for steering flexible needles through soft tissue that explicitly considers uncertainty in needle motion, introducing a new objective for image-guided motion planning: maximizing the probability of success. The uncertainty is in this study related to the probability of deflection of the needle from a specific insertion. Their method formulates the planning problem as a Markov Decision Process (MDP) based on an efficient discretisation of the state space, models motion uncertainty using probability distributions, and computes optimal actions (within error due to discretisation) for a set of feasible states using infinite horizon Dynamic Programming (DP). This approach only requires parameters that can be directly extracted from images, allows fast computation of the optimal needle entry point, and enables intra-operative optimal steering of the needle using the precomputed dynamic programming look-up table.

A second way to account for deformation is to use a finite element mesh (FEM) to compute soft tissue deformations. Vancamberg et al.[VSMM] used this information to minimize the final error of a RRT solution in a breast biopsy application whereas Patil et al. [PVdA11] used FEM meshes combined with a sampling-based algorithm to plan in highly deformable environments. The efficiency of these strategies is highly dependant on the quality of the mesh simulation and how accurately it represents the real tissue. However the most common alternative is to apply a single-query planner that is fast enough to be used intra-operatively in order to replan the trajectory from imaging or sensing feedback information as in [PBWA14].

Table 2.1 shows the result of a literature review of online planning methods which have been proposed between the year 2013-2020 in the field of 3D needle steering.

These online planning techniques can be evaluated with respect to a list of fundamental features in the context of a real-time surgical scenario. Among these:

- Average computational time

    In intra-operative path planning, the execution time of the algorithm plays an important role in determining the applicability of the planner. The update frequency requirement depends on factors such as the needle insertion speed or the refreshment rate of the sensing which could include a real-time imaging modality such as 3D intra-operative ultrasound

Method group	Method	Paper	Entry	Goal	Hardware	Simulation	Phantom	Ex Vivo	Target stationary	Target moving	Obstacles Static geometrical	Obstacles Static anatomical	Obstacles Moving geometrical	Obstacles Moving anatomical	Time (s)	Target Error (mm)	Std deviation	Success Rate (%)	Parallelisable	Experimental setup
Search-based methods	RRT	VAP+14	Pose	Region		o	o		o	o	o			o	$6\,e^{-1}$	1.76 / 2.16	1.02 / 0.88			The needle is steered in a soft-tissue phantom using closed-loop motion planning towards a virtual moving target (0.4 mm/sec resulting in 7 mm displacement) while avoiding moving obstacles (0.3 mm/sec resulting in 3 mm displacement) in a 3D environment (N=10).
Search-based methods	RRT	ZWZ+	Pose	Pose	Intel Core i5 (4-core, 2.5 GHz)	o				o			o		$3.7\,e^{-3}$	1.31	0.38	100		Maximum radius of curvature is set to 50mm. Six spherical obstacles (Radius 2 cm) are considered. Movement of target and obstacles are modelled as 3D periodic sinusoid motion in 3D with amplitude of 5mm and period of 60s and 5s respectively (N=20).
Search-based methods	RRT	FSM18b	Pose	Pose	Intel Core i5 6500 (3.2 GHz)	o			o			o			0.5			From 60 to 95		Simulation of cochlea access application using CT data from 22 real and 100 synthetic anatomies (maximum curvature k=0.05). The number of paths found per second, the minimum distance from obstacles and the target accuracy are evaluated depending on the obstacle map complexity
Search-based methods	RRT	PBWA14	Pose	Region	Intel Core i7 (3.33 GHz)		o	o	o		o				1	3.6	1.85		o	Spherical target (Radius=0.5mm). 10 random target regions are chosen. They compare closed-loop fast replanning versus open-loop insertion (N=5).
Search-based methods	RRT	SPA15	Point	Region	Intel Xeon (i2 Cores)	o			o		o	o						98	o	Spherical target (Radius=0.5cm). Two scenarios are considered. One with known needle maximum curvature and one with online curvature estimation (N=100).
Search-based methods	RRT	HBM+19	Point	Region		o			o			o			1.4			From 69 to 100		RRT-based approach incorporating the physical constraints of a magnetically guided flexible needle. Tested on 921 entry points with goal region in the brain (in the STN and in the fornix)
Search-based methods	AFT	GCSR16	Pose	Region	Intel Core i7 (3.2 GHz) & Nvidia GTX TITANX GPU	o				o		o			$5\,e^{-3}$	1.45	1.19		o	Simulation of needle steering through liver tissue. The target motion is 2 cm overall. Results are compared with RG-RRT (N=100).
Search-based methods	APF	LJL+17	Pose	Point		o	o		o		o	o				0.29/1.15	0.56			Simulation of prostate brachytherapy using an organ group mock-up (N=5).
Search-based methods	APF	LJYY		Point		o			o		o				0.9\12	1.019				3D APF is used in combination with improved conjugate gradient algorithm (ICGA) to speed up computation and avoid local minima.
Search-based methods	A*	Kha	Pose	Region		o	o	o	o		o				1	0.1				A circular obstacle (radius=2mm) and a target (radius=1mm). The needle deflection along the insertion is evaluated at different speed. The difference between prediction and experimental data is discussed (N=5).
Search-based methods	A*	Moh1	Point	Region		o			o			o								Simulation with binary images derived from diagnostic image processing. Distance from obstacles is evaluated.
Numerical methods	MDP	TYLC18	Point	Region		o	o		o		o							68		Simulation using liver CT data to compare performance with respect traditional MDP (N=1000 computational simulations). A phantom is used to validate it experimentally (N=5).
Numerical methods	MDP	WA14	Pose	Pose	Intel Core i7 (3.7GHz)	o			o		o				26	0.17	0.01	99		Simulation of needle steering through liver tissue. The probability of collision, average curvature deviation and deviation to target are evaluated. Results compared with LQG-MP (N=1000).
Numerical methods	Ob Function	SDH+14	Region	Region	Intel Core i7 (3.5GHz)	o			o		o				1.8			81		An entry region is considered (0.1x5x2.5). A spherical target region (radius 0.25mm) is considered in a simulated prostate environment.

Table 2.1: Review of path planning techniques for steerable needles insertions which have been developed and tested between 2013 and 2020.

(i-US). In general, the path planner needs to be fast enough to update the insertion path according to the current needle position and environmental configuration. The choice of hardware and software used can also affect the execution time. As the hardware and software used in different studies varied, the performance of different planners in term of

computational speed is hard to be compared. Besides, in some cases the search speed can be accelerated with parallel processing utilizing the benefit of multi-core CPU or/and GPU.

It is clear from Table 2.1 that search time for sampling-based methods is lower with respect to graph-based and optimisation-based ones. RRT-based planners maintain good performance even in a 3D anatomical environment [PBWA14, FSM18a]. However, their maximum run time is user-defined considering a good trade off between speed and rate of success. Therefore, at equal maximum run time, a more complex obstacle map would lead to a decrease in success rate [FSM18a]. On the other hand, the sampling-based AFT [LGCSR16] features a fixed computational time regardless of the complexity of the obstacles. This is advantageous in a neurosurgical context where the complexity of the anatomical environment is patient-specific.

- Algorithm robustness: success rate

The success rate in finding a collision-free trajectory is an indication of the robustness of the path planning algorithm. However, this metric cannot be decoupled from the complexity of the considered environment, both in terms of obstacles density and possible applied deformations. Additionally, simulation tested methods feature a smaller targeting error than those tested on phantoms or biological tissue, as Table 2.1 illustrates. This is because computational simulations are free from real-world uncertainties and system disturbance while phantoms do not replicate the inhomogeneity of real tissue. This inhomogeneity [AVP+14] and the anisotropy of needle-tissue [PBWA14] are, infact, causing variation in needle behavior during the insertion. Although using biological tissue provides a better representation of the operative environment compared to phantom, repetitions of the experiment are difficult to achieved as it is hard to perform multiple insertions on the same sample [TYLC18]. Looking at Table 2.1, it is possible to deduce that numerical methods are generally not evalutaed using a realistic clinical setting (i.e. simulation using medical imaging or experiment on *ex-vivo* with moving target or obstacles). On the other hand, sampling based method (RRT, AFT etc.) show high success rates, specially in complex anatomical environments.

- Target accuracy and precision

  In the context of minimally invasive neurosurgery, literature suggests that neurosurgical straight needle insertions with accuracy of 3.2 ± 1.4 mm are common when using stereotactic frames [DPK+10]. The accuracy of the insertion can be determined by the mean targeting error while precision corresponds to its standard deviation. Precision is more important as we could possibly calibrate or account for the estimated targeting error in the planning phase. While low precision decreases the possibility of success rate of the surgery (which depends on whether a path without collision can be found and whether the treatment is delivered to the allowable region) as the result is not repeatable or predictable.

  Accuracy also relies on planner ability to account for the uncertainties. In [PBWA14], the targeting error is compared between a closed-loop system and an open system. It is observed that open system leads to much larger targeting error, thus higher accuracy means better performance under the highly deformable environment. Additionally, in a real operational setting, systemic errors from different sources such as sensing sensors calibration, flexible needle modelling and needle curvature estimation contribute to the resulting target accuracy.

- Environmental and surgical constraints

  The performances of a path planner can be influenced by both the complexity of the considered search space and the surgical constraints on entry and goal pose. As shown in Table 2.1, the obstacle map could be either be static or deformable while the obstacles could either be geometrical or complex anatomical structures. On the other hand, the entry pose or position can be defined as a constraint; the same happens for the target. It should, therefore, be considered that user-defined constraints can increase the difficulty of the path search, thus influencing both the average rate of success and the average computational time. For instance, in Fauser et al. study [FSM18a], the performance of the proposed planners are discussed with respect to different surgical environments of increased complexity. The ability of the suggested planners in meeting headings constraints

is also evaluated.

Integration of local and global methods

Global path planning methods such as sampling-based methods are generally favoured with respect to local ones for needle steering applications since, beside reacting to local changes and unexpected obstacles, they are able to deal with the global problem of reaching an arbitrary goal. On the other hand, these methods recall a global path planner at high frequency during the needle insertion, thus increasing the computational cost and causing "path stability" issues. The term "path stability" can be used to refer to a measure of the difference a process induces between an original (source) plan and a new (target) plan. With regard to path stability to environmental changes during the procedure, several improvements to the conventional RRT method are proposed in [ZWZ⁺]. Between these, the Old Point Tracking System (OPTS) considers the former generated path when it calculates a new one, thus reducing the probability of long path detours and improving stability. A more elegant solution to this problem is offered by "Elastic Band" methods [QKb] which treats the reference path as a deformable object (i.e. an elastic), adjusting it only in response to changes in the environment while maintaining its overall smoothness. This technique benefits from an enhanced reactivity without limiting the ability to achieve global goals. By deforming the path when changes in the environment are detected, the computational cost of recalling a global path planner is avoided. The robot can react in real time to information obtained by sensors keeping complete clearance from obstacles. This technique provides a strong connection between the robot and its environment while preserving the global nature of the planned path. The elastic band concept was originally introduced by Quinlan and Khatib [QKb, Kha] to close the gap between global path planning and real-time sensor-based robot control. A variation of the elastic band technique known as "bubble bending" [LT11][TBV17] has also been proposed for real-time collision-free path planning for an autonomous small-scale helicopter flying through cluttered, dynamic 3D environments. The first step of the algorithm involves the computation of a initial path. Following this step, spheres (bubbles) are evenly inserted along the path labelled with ascending numbers from 0 (start) to bubbles N (goal). The bubble size creates a collision free channel around the path which

accounts for a safety margin from obstacles. The most recent information on the environmental static and dynamic obstacles can be used to modify the path in real-time. Two virtual forces are introduced to describe the interaction between bubbles or with external obstacles.

Each bubble's centre is attracted by two internal forces: one from its preceding bubble and the other from the following one. Moreover, external forces from the obstacles exist. Specifically, they are repulsive forces which deform the bubble band adequately and then keep the path collision-free. Only the closest obstacle to a node can influence its position. The Bubble Bending method, which has never been applied to steerable needle applications in the past, it will be extensively treated in Chapter 5 as part of a novel planning solution

2.2   Conclusion

The steering of flexible needles in soft-tissue interventions is subjected to uncertainties from medical imaging, imperfect actuation of the robot, complex tissue-needle interaction, tissue deformation and target/obstacle motion. Hence, to prevent the risk of collision with anatomical obstacles, intra-operative path planning methods should be implemented to adjust the pre-operative path.

Numerical methods require extensive calculation and numerical optimisation, resulting in higher targeting accuracy. However, because of the high computational cost, these methods are not easily adaptable to complicated environments. On the other hand, sampling based methods are associated to relatively fast algorithms which can search for multiple feasible paths simultaneously. Because of the relatively faster speed, sampling based methods can be used at high frequency intra-operatively. Additionally, they can be applied to complex environments containing irregular shaped obstacles as for surgical applications. However, they cannot guarantee full optimality and they often require smoothing as postprocessing step. It can be concluded that nowadays, path planning methods are mostly tested in static geometrical environments. Future research should focus on path planning methods for flexible needle insertions tested in realistic anatomical environments under tissue deformation [LKR18]. Finally, more importance

should be given to path stability during intra-operative replanning, favouring an adaptation of the existing plan to the updated context rather than replanning the insertion path from scratch. These future directions are explored in the remainder of this thesis.

Chapter 3

Path Planning for Steerable Needles: Entry Point Selection

In this chapter, a pre-operative path planner tool for steerable needles is presented. The research presented includes some edited sections from the research study previously published in:

Marlene Pinzi, Stefano Galvan, and Ferdinando Rodriguez Y Baena, "The Adaptive Hérmite Fractal Tree (AHFT): a novel surgical 3D path planning approach with curvature and heading constraints." International journal of computer assisted radiology and surgery, vol. 14, no. 4, pp. 659–670, april 2019.

3.1 Introduction

The blood-brain barrier features as the major limitation of routine drug delivery into the brain, owing to its effectiveness in blocking most of the drugs with the blood circulatory system. As a promising alternative, convection enhanced delivery (CED) has been developed to directly infuse the drug into the brain interstitial space as a method to bypass the blood-brain barrier. Although the feasibility and safety have already been reported in preclinical [APM07] and clinical [VA15] studies, the treatment efficacy of CED remains disappointing [ZW18a]. This is

especially due to the complex structure of brain tissue, resulting in the difficulty of controlling drug transport and disposition. Moreover, surgical operations are generally constrained to the straight-line trajectories, which limit the treatment choices available to the surgeon to those requiring a curved insertion to avoid obstacles as blood vessels and brain ventricles. This limitation is especially important for treating the tumours bedded in the deep brain. All these open issues fuel the European project, EDEN2020, to develop an innovative steerable programmable bevel tip needle (PBN) for the application to convection-enhanced drug delivery in minimally invasive neurosurgical procedures [SR16].

A drug transport model is developed, within the context of EDEN2020, to optimise the CED administration parameters for drug effective accumulation and homogenised distribution. Based on the theory of fluid and solid mechanics, and the mechanism of intratumoral drug transport, the model is design to predict the spatio-temporal profile of drug bioavailability by incorporating the patient specific information acquired from magnetic resonance imaging. The total drug distribution volume and the spatial characteristics of drug spatial distribution serve as the criteria to evaluate the delivery outcomes for the optimisation of catheter placement and infusion regime for each patient [ZW18a, ZDB19].

Once the model predicts the target pose of infusion, an entry pose, orthogonal to the patient's skull, is desired in order to facilitate the creation of a suitable burr-hole. In current straight needle based procedures, the target is usually a point with no specified orientation; the surgeon selects manually the entry point on the patient skull, trying to minimise the risk to damage functional and sensitive anatomical structures, while staying perpendicular to the skull surface.

In the context of steerable needles, this task is even less suitable to be performed manually since the flexibility of their trajectories, together with application dependant surgical constraints, makes the entry pose selection not intuitive to clinicians [VDTB97]. In fact, given a particular target pose and the kinematic constraints of a needle, port placement would become exceptionally challenging due to the difficulty of mental reconstructing the three-dimensional shape of brain structures. Furthermore, a needle displacement from the pre-operative planned trajectory may result in severe neurological complications. Therefore, it is desired to select

a pre-operative path with a minimum safety distance from critical structures such as blood vessels, ventricles and some of the major brain functional areas such as motor, sensory, vision and speech correlated brain cortex regions.

Surgeons would like to be able to know beforehand the feasibility of the target pose for a designated skull region. A computer-assisted planner is needed to aid surgeons in mapping the patient skull's possible accesses for a given target pose.

A patient-specific brain obstacle map is necessary in order to generate a safe trajectory. It allows the system path planner to attribute a score to feasible generated paths not only in terms of kinematic and dynamic constraints of the surgical tool but also in terms of safety for the patient. The obstacle map usually makes use of information coming from different imaging modalities such as magnetic resonance images (MRI), diffusion tensor images (DTI), functional MRI (fMRI) and angiographies (MRA). In Caborni et al. [CYD+12], the main brain structures of a segmented Magnetic Resonance Imaging (MRI)-based dataset were arbitrarily classified into six categories according to the risk associated with the insertion of the needle into each. The chosen categories were defined as "Avoid", "Dangerous", "Warning", "Careful", "Common", "Accessible", with each class represented by a unique grey value on the image, white being impenetrable and black meaning fully accessible. "Avoid" and "Dangerous" areas and optional user-defined restricted regions, such as patient-specific constraints, are set to "no-go" areas that the probe must avoid. Although they assign each candidate trajectory with a risk value based on a weighted sum, the main drawback is that no risk visualisation or quantitative feedback is provided.

Newer approaches use operator-defined criteria to visualise color-coded projections of the brain's internal sensitive structures on the patient skull. These structures are usually meshes or segmented volumetric data which we consider as "obstacles". In [Tro12] trajectories are calculated after segmenting structures such as blood vessels, ventricles and high-density fibre bundles. The risk-based map is the weighted sum of all these structures and contains for each optional entry point the summarised risk value. The safest entry points are selected from each region on the skull surface, and for visualisation, a colour coded trajectories and the head surface are

presented.

An additional feature is presented in this study [TDBF]. Here the surgeon can update, through natural language, rules that can be stored in order to prevent the probe from crossing structures and help to solve possible conflicts in the optimisation strategy. Additionally, the risk-based map can be updated with new knowledge after each intervention. This process is quite time consuming, especially if the goal isn't a single point but perhaps a 3D region from which multiple target points can be considered.
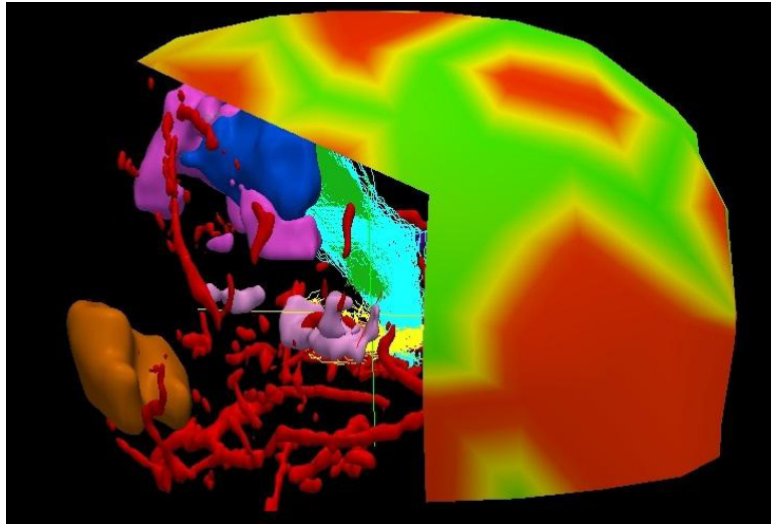
Figure 3.1: Segmented structures and color coded head surface: green describes low risk access area, yellow refers to medium risk access area while red is associated to high risk access areas on the patient's skull. [Tro12]

In order to avoid errors due to discrepancies between the pre-operative and the intra-operative images, the trend is to move the entry point selection and the path planning calculation into the operating room. From here, the need for a time-efficient GPU accelerated method, for mapping possible access areas on the patient's skull and be able to provide feasible solutions at interactive speed.

In this Chapter, we propose the so-called Ray-traced AFT algorithm: a combination of the standard Adaptive Fractal Tree (AFT) [LGCSR16] planner with a GPU accelerated ray-tracing algorithm. First, the obstacle map is expanded with a margin that takes into account both the needle ray and a safety margin from the obstacles. Then, the proposed AFT based path planner runs from the selected infusion pose generating a series of obstacle-free paths which

intersect the skull at different points within the needle reachability region, delimited by its maximum achievable curvature. Afterwards, a ray-tracing method, running in parallel on the GPU, considers the AFT obstacles-free generated paths and selects only the ones crossing the skull of the patient at a right angle (within a predefined tolerance) in order to match the burr-hole port requirements.

The classification of the successful intersection points allows identifying independent sub-regions on the patient skull from where paths matching both kinematics and surgical constraints can be found, thus leaving the final selection of a successful path within those regions to the clinician.

The assessment of the proposed method, through a computational simulated environment, has shown that our technique is robust and can generate curved paths starting from a mesh-based obstacle map representation. Figure 3.2 illustrates the method.

We believe that this is the first method to enable interactive calculation and visualisation of curved trajectories in a commercial neurosurgical software. Owing to its low computational time, the user can interactively explore a series of potential trajectories and target points, thus providing guidance during the preoperative path selection.

In the next sections, the obstacle map creation procedure (Section 3.2) is first discussed. Then the Ray-traced AFT algorithm (Section 3.3) is described in detail. The description of a path cost function, used to rank the generated paths follows, which is outlined in Section 3.4. Finally, the resulting skull entry-points mapping is demonstrated and discussed in Section 3.5 and 3.6, respectively.

3.2   Obstacle Map Creation

In this study, we propose a GPU accelerated, patient-specific skull mapping method for steerable needles called "Ray-traced AFT". Given a desired target pose, our technique is able to map corresponding feasible entry regions on the patient's skull accounting for obstacle avoidance, patient risk and probe curvature constraints. Successful entry regions are highlighted on the

patient's skull to aid surgeons during the entry point selection for a given target pose. The proposed Ray-traced AFT requires, as input data, a patient-specific rasterised 3D obstacle map which is generated through the following procedure:

- Diagnostic images segmentation: meshes of sensitive structures are generated from pre-operative diagnostic images. Brain ventricles and vessels are usually considered as in Figure 3.3. The skull is also segmented from a pre-operative computed tomography image (CT) and a mesh of its surface is generated.

- Voxelisation: a voxelization process [Ada20] which converts the multiple 3D triangular meshes into a volumetric obstacle map (a discrete grid) considering the skull surface edges as reference for the obstacle map size, is performed. A specified resolution, usually matching the one of the reference diagnostic image, is given as input to the voxelisation process which automatically selects an adequate grid size for the resulting obstacle map. A value equal to "2" corresponds to obstacles, "1" corresponds to free search space while the skull region is labelled as "0". Equal importance is given to all segmented brain structures within the discrete obstacle map. This affects the complexity of the path planning task, which aims for full obstacles clearance. The hard constraint on obstacles avoidance is justified by the enhanced flexibility attributable to steerable needles with respect to their straight counterpart; they can be programmed to reach a precise goal while avoiding sensitive regions along the way and adjust their trajectory intra-operatively.

- Obstacles dilation (Figure 3.3): the algorithm compensates for the non-volumetric nature of the calculated trajectories by expanding the obstacles with a margin equal to the size of the needle plus a given safety amount that takes into account real-world uncertainties during the insertion arbitrarily set to 30% of the PBN radius (0.43 mm). Given a rasterized binary obstacle map and the total margin, a proposed GPU accelerated algorithm is used to expand the obstacle map in 3D by the given amount. Every thread on the GPU is responsible for a specific voxel belonging to the given binary map. If the considered voxel belongs to the obstacle region (its value in the binary map is equal to "2"), then every surrounding voxel within a radius equal to the given margin, that is also obstacle free, is
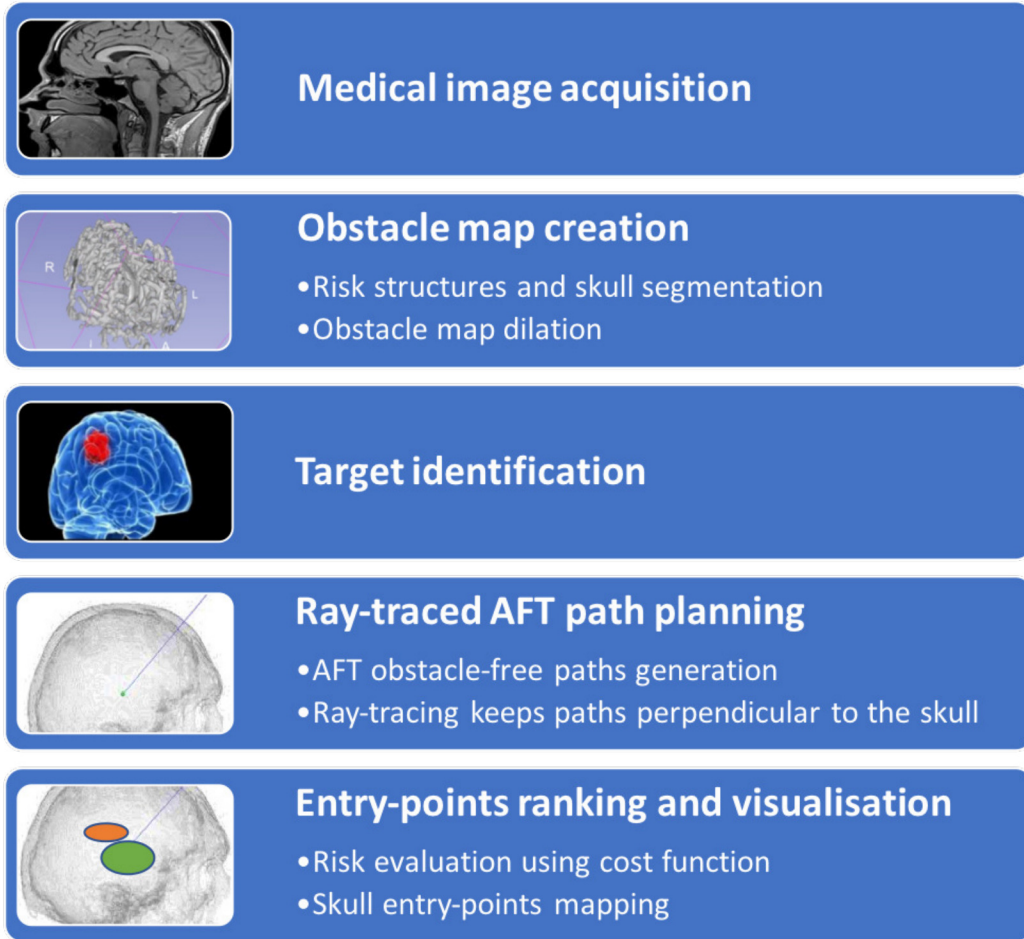
Figure 3.2: Workflow of the proposed Ray-traced AFT pre-operative planning tool. First, diagnostic images are acquired by clinicians, patient specific risk structures are segmented; the dilation of obstacles by a given safety margin and target identification (which is either manually selected by the surgeon or automatically through a drug diffusion model) follows. Finally, the Ray-traced AFT planner searches for obstacle-free paths, perpendicular to the skull (within a given tolerance); it evaluates and ranks them according to a cost function which accounts for safety of insertion. Feasible regions on the patient's skull, corresponding to successful paths are highlighted as a coloured overlay to clinicians in order to aid in path selection.

considered as part of the obstacle margin volume. A label equal to "3" is associated with the obstacle expansion volume to distinguish this margin from the original obstacles. The skull region is also expanded by a value equal to the selected map resolution, as explained in Section 3.3.
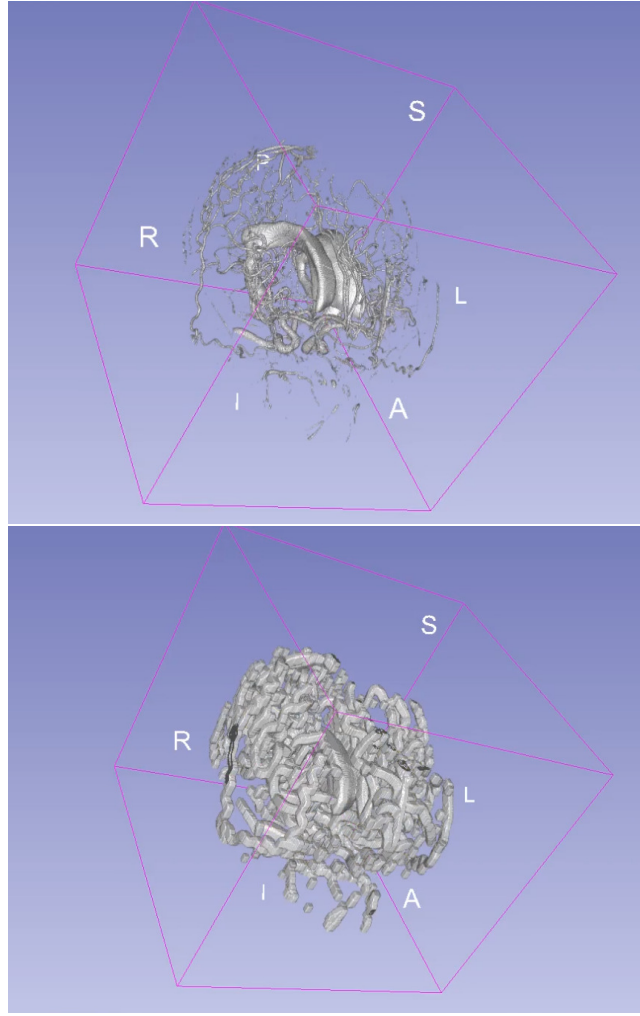
Figure 3.3: Brain obstacles before and after the addition of a margin which takes into account the needle diameter and a safety distance to compensate for real-world uncertainties.

3.3 Ray-traced AFT path planner

First, an optimised goal pose in the brain tumour's proximity is generated by a drug diffusion model [ZDB19, ZW18a] or, alternatively, it is manually selected by the clinician. The Ray-traced AFT algorithm, running on the generated dilated obstacle map (Section 3.2), can be divided into two different steps:

- AFT obstacle-free paths generation: an AFT-based path planner generates obstacles-free trajectories which start from the given target pose and meet the given kinematic and surgical constraints.

- Ray-tracing: a ray-tracing parallelised method evaluates the AFT obstacles-free trajec-

tories identify those which intersect at 90 deg (within a given tolerance).

The remaining paths are ranked with respect to a cost function. Then, their corresponding feasible entry points are used to create a skull overlay that allows neurosurgeons to interactively visualise the resulting skull mapping in a 3D rendered view to facilitate the selection of an optimal entry point.

In the next sections we will illustrate in more details the Ray-traced AFT stages and the algorithm potential use as a patient-specific skull entry point mapping tool during the pre-operative phase of steerable needle insertion.

3.3.1   Adaptive Fractal Tree based algorithm

The Adaptive Fractal Tree (AFT) [LGCSR16] is an algorithm built on the recursive generation of a self-similar (fractal) structure within the search space, which grows from a given initial pose (Figure 3.4). Each branch of the tree is associated to a GPU thread and runs in parallel on the graphics card, thus optimising the use of computational resources (Figure 3.5). The topological structure of the tree resembles the recursive nature associated with the motion of nonholonomic needles. At each step, all possible future motions depend on the current pose, a process that reverses recursively from the last branches back to the root via all tree levels. The basic tree structure with this fractal geometry features five possible motion directions: straight, up, down, right and left, represented by a straight line in the first case and arcs for all remaining cases, the curvature value of which can be chosen based on the needle's constraints. The search space between the straight line and the maximum curvature arcs can be explored by adding further arcs featuring lower curvature. For instance, if there are two arcs for each direction, the amount of possible motion directions, which is labelled as the tree density parameter (ρ), increases from five to nine. The tree's basic structure can be shaped according to any given scenario by tuning a set of fundamental parameters associated with the trajectory generation and the needle design parameters. These include the branch length l and the density of the tree ρ. An important factor in providing an efficient parallelisation is the enumeration of each tree

branch with an ID number. The fractal structure of the tree guarantees that parent and child IDs have a regular pattern. To each ID corresponds a control action or "type" which defines the rules for travelling up and down the tree explained in Figure 3.5.

In each GPU thread, a voxel-based collision check is performed for every branch in parallel at the resolution required. In particular, each branch interpolation point is checked for collision with respect to the obstacle map.

One sample colliding is enough to filter out the entire branch it belongs to. In addition to obstacles collision, in the proposed Ray-traced AFT algorithm, each sample is also checked for collision with the obstacle map skull region (labelled as 2). This step replaces the parallel calculation of the euclidean distance from the desired target point implemented in the standard AFT algorithm proposed by Liu et al. [LGCSR16]. In fact, the Ray-traced AFT is not looking for paths reaching a given target but for paths crossing the patient's skull in different locations as in Figure 3.7.

At this stage, the algorithm follows a GPU accelerated back-propagation process which exploits the fractal nature of the tree. As described in [LGCSR16] the back-propagation reconstructs continuous obstacle-free paths starting from a set of input branches going backwards until reaching the root of the tree. In the Ray-traced AFT implementation, we set as input branches all the segments that were labelled as colliding with the patient's skull. The modified AFT back-propagation method results in obstacle-free paths which intersect the skull in at least one interpolation point belonging to their last branch (as the green and the blue path of Figure 3.7).

Further filtering needs to be completed in order to consider only those paths which meet the given surgical constraint on the entry pose. In particular, the orientation of a given path in correspondence to its intersection with the patient's skull is desired to be perpendicular. A ray-tracing algorithm is implemented in the next section to adapt the AFT search to this constraint.
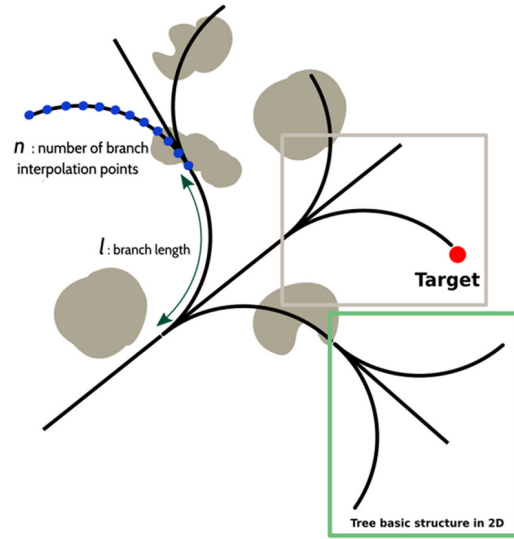
Figure 3.4: Geometry of the tree in 2D with a focus on the basic structure of the fractal geometry (within the green window).
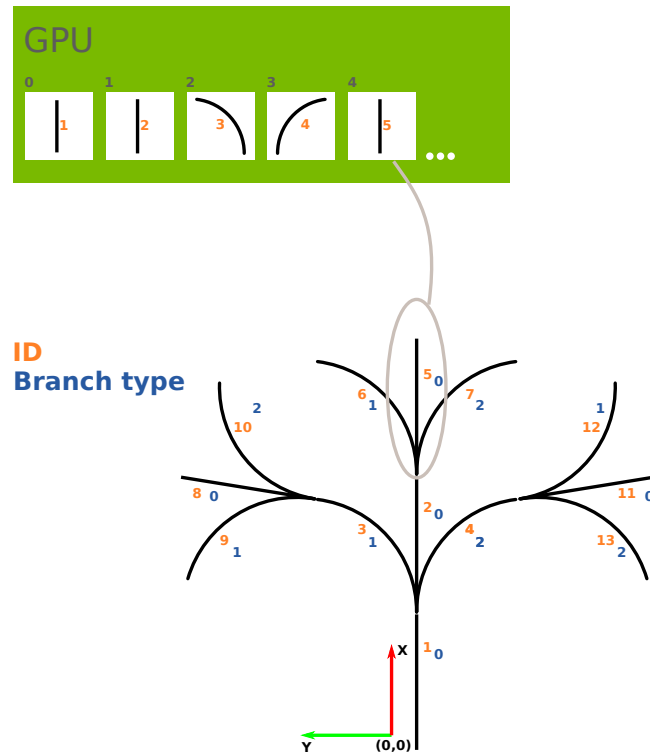
Figure 3.5: The fractal structure of the tree can be easily parallelised; each tree segment can be allocated to a GPU thread, as shown in the figure. Given the fractal nature of the tree, it is possible to attribute a certain "type" to each branch belonging to the tree's basic structure. Each branch features a different ID number, but its corresponding type can easily calculate dividing its ID number by the density parameter (ρ) value of the basic tree structure.
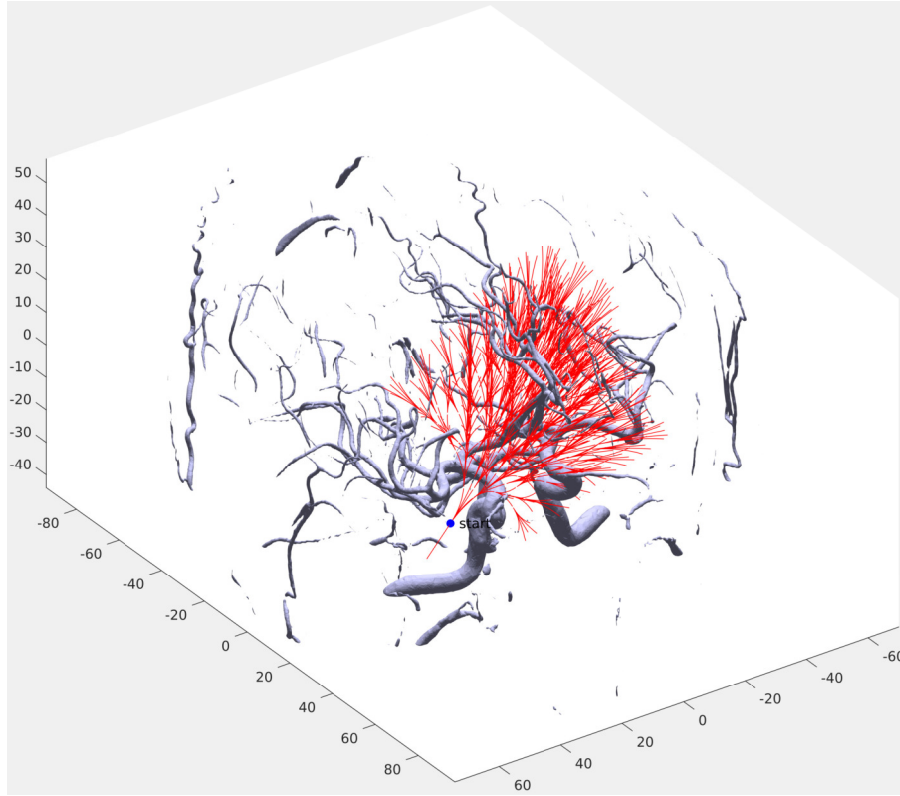
Figure 3.6: Adaptive fractal tree (AFT) extending through segmented brain vessels which constitute the obstacle map

3.3.2 Ray-tracing

Given the previously segmented patient's skull mesh and the resulting AFT based paths, a ray-tracing technique is now needed to evaluate the precise points of path-skull intersection and assess their approach angle with respect to the normal of the skull.

A well known ray-tracing method called Möller-Trumbore algorithm [MT05] is implemented in a GPU parallelised version. In particular, each skull-colliding branch, belonging to a resulting AFT based path, is evaluated on a separate thread. Therefore, this ray-tracing technique has also been adapted to fit with the AFT based path search results.

The Ray-traced AFT algorithm running on each GPU thread can be summarised as follows:

- Each AFT sample point is evaluated in parallel on the GPU. Each thread is checked for a potential intersection with the patient skull by assessing all the faces constituting the given skull mesh.
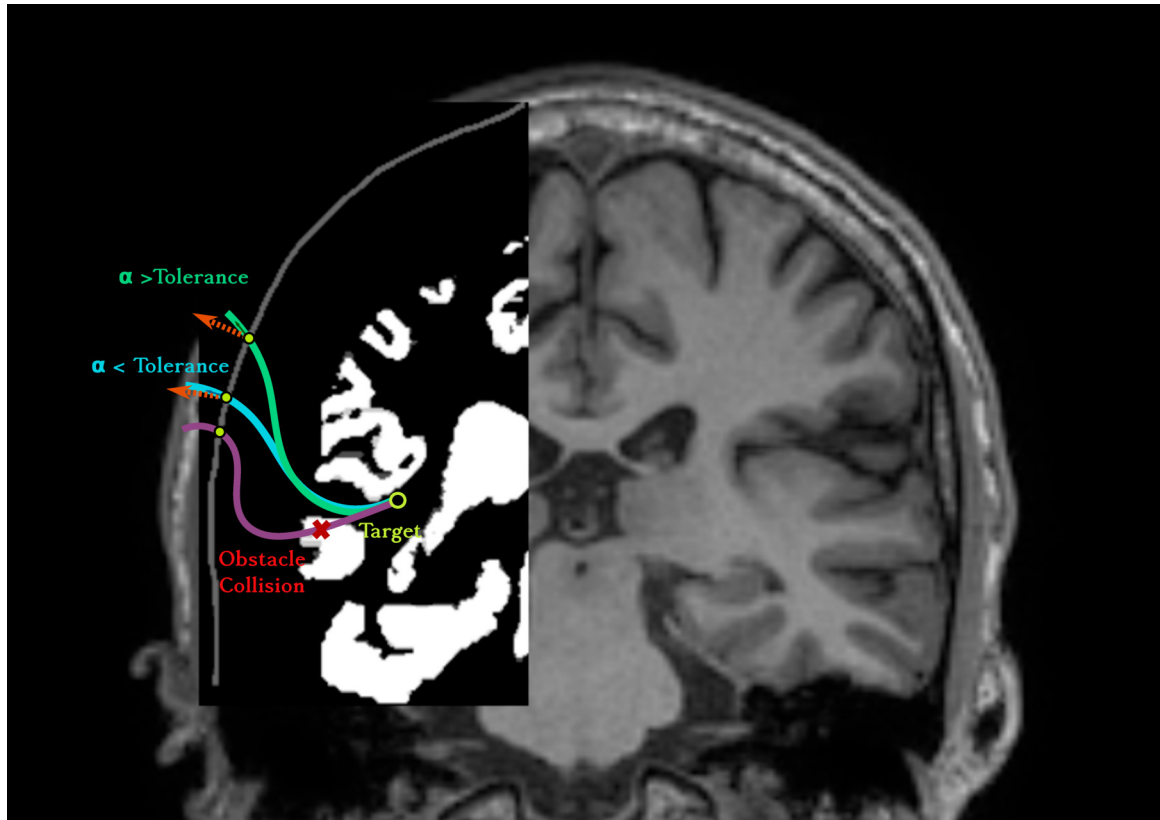
Figure 3.7: Three examples of AFT first-stage generated paths, starting from a given target pose and crossing the skull at different points, are shown. The green path intersects the skull with an angle outside the given tolerance with respect to the normal of the skull, while the pink path collides with an obstacle. The only successful path is the blue one, which is obstacles-free, and it also crosses the skull almost perpendicularly.

- For each given AFT sample point laying in the patient skull region and belonging to an obstacle-free path, the previous point along the same path is found, and the segment linking the two is considered and saved as *dir*.

- We look for the intersection point P between *dir* and the plane represented by each of the patient's skull mesh faces. $faces1, faces2, faces3$ are one-dimensional arrays featuring the indexes of the vertices delimiting the skull mesh faces. The corresponding 3D vertices coordinates are also inputted through three separate arrays called vx, vy, vz. For each face mesh, a cross product of its edges is performed to obtain the normal of that face/plane. The intersection point P, if it exist, lays on a ray directed along *dir* at distance t from its origin $(0, 0, 0)$. We can also assess that if P exists, it has to belong to the face plane considered, the standard equation for which is $ax + bx + cy + d = 0$. a, b and c are the components (or coordinates) of the normal to the plane we previously calculated and d is instead the unknown distance from the origin to the plane. Knowing the plane normal N and at least one of the three triangle's vertices $v0, v1, v2$ lying in the plane is enough to compute d. Consequently, we can substitute the expression for P within the plane equation and solve for t.

- If a point of intersection is found, its inclusion within the considered mesh face is evaluated. The so-called inside-outside test is used in this case. If a point P is laying on the triangle's plane then the dot product between the triangle's normal and a vector C is positive. To apply the technique we need to repeat the test for each edge of the triangle where C is the result of the cross product between $edge0, edge1, edge2$ and vectors $(P - v0)$, $(P - v1)$ and $(P - v2)$ respectively for each edge of the triangle. If the inside-outside test is verified for all the edges, P is within the considered face. The reader can find the geometrical detail in the study of Möller-Trumbore et al. [MT05].

- If the inclusion test is passed, then the misalignment between *dir* and the normal of the plane at the intersection point is calculated using the dot product formula.

- The considered branch and, therefore, its corresponding obstacle-free path is considered successful only if the misalignment is within a given tolerance (*tol*). A *label* equal to 1 is

associated with a successful path.

The following code implements the Möller-Trumbore ray-tracing method [MT05] to check the path intersection with each face of the patient's skull mesh:

Data: *dir*, *faces*1, *faces*2, *faces*3, *vx*, *vy*, *vz*, *tol*

Result: *label*

initialisation;

for *each face of the skull mesh* **do**
    find face vertices *v0,v1,v2* and normal *N*;

    ▷ Step 1: find segment-plane intersection: *P*

    RayDirection = dotProduct(N,dir);

    d= dotProd(*N*,*v0*);   ▷ compute *d* parameter

    *t = (*dotProduct(*N*,*orig*) *+ d) / RayDirection*;   ▷ compute t parameter

    *P = orig + t * dir*;   ▷ compute the intersection point P

    ▷ Step 2: Check triangle inclusion

    vp0 = P - v0; *vp1 = P - v1*; *vp2 =P - v2*;

    C = crossProd(*edge0*,*vp0*); C1 = crossProd(*edge1*,*vp1*); *C2* =crossProd(*edge2*,*vp2*);

    if *C0,C1 and C2 > 0* **then**
        inside-outside test is successfull;

        ▷ Step 3: Check crossing angle

        angle=atan(||crossProduct(N,dir)||, dotProduct(N,dir));

        if *angle < tol* **then**
            | *label*=1;   ▷ crossing angle is within tolerance

        else
            | *label*=0;

        end

    else
        | no intersection between *dir* and face;

    end

end

3.4 Risk evaluation using a cost function

In this study, a cost function measuring path length and smoothness is introduced with the aim of minimising patient risk and facilitating the control of the needle movement during the insertion. Each resulting path is evaluated via the following cost function (CF):

$$CF = w_1 * \sum_{i}^{n_{seg}-1} \frac{|C_{i+1} - C_i|}{2 * max_{curv}} + w_2 * \sum_{i}^{n_{seg}} \frac{|C_i|}{max_{curv}} + w_3 * \frac{length}{max_{length}} \qquad (3.1)$$

where n_{seg} represents the number of segments or tree branches composing the path. The cost function considers the preferential path characteristics, where the first term of the equation is the curvature gradient which is calculated as the sum of the difference between the curvatures (C_{i+1} - C_i) of consecutive branches constituting the path with respect to the maximum achievable value measured in the proximity of an inflection point between two arcs of maximum curvature ($max_{curv} = \frac{1}{70}$) and opposite sign. It measures the smoothness of the trajectory in terms of the absence of inflection points and curvature variability. This feature is preferred because it facilitates the control of the needle movement. The second term refers to the sum of the segments' curvature k with respect to the maximum curvature value, which reflects the linearity of the path. Trajectories presenting moderate curvature, away from the maximum constraint of the needle, are favored. The path *length*, which is normalised with respect to the maximum path length ($max_{length} = tree_{levels} * l$ with $tree_{levels}$ being the number of tree growth levels and l being its branches length), is minimized to favor short paths, with the effect of reducing potential tissue damage during needle insertion. The three function terms are weighted by their corresponding coefficient, where $w_1 = w_2 = w_3 = 1$ in order to give all the same contribution. Colour-coded information, added to the skull overlay, could contribute to the decision-making process by attributing different risk to the calculated trajectories and corresponding entry points. Optimal paths are the ones which minimise the cost function value, and they are therefore highlighted with a different colour on the skull overlay, thus providing visual feedback to the surgeons as in Figure 3.9.

3.5 Skull entry-points mapping simulation

The Ray-traced AFT algorithm has been first tested in simulation using real data acquired on a brain tumour patient and then implemented on the EDEN2020 neurosurgical interface (Chapter 6) to aid surgeons in selecting an appropriate entry point on the sheep skull accounting for kinematic constraints of the EDEN2020 probe and surgical constraints of the operation.
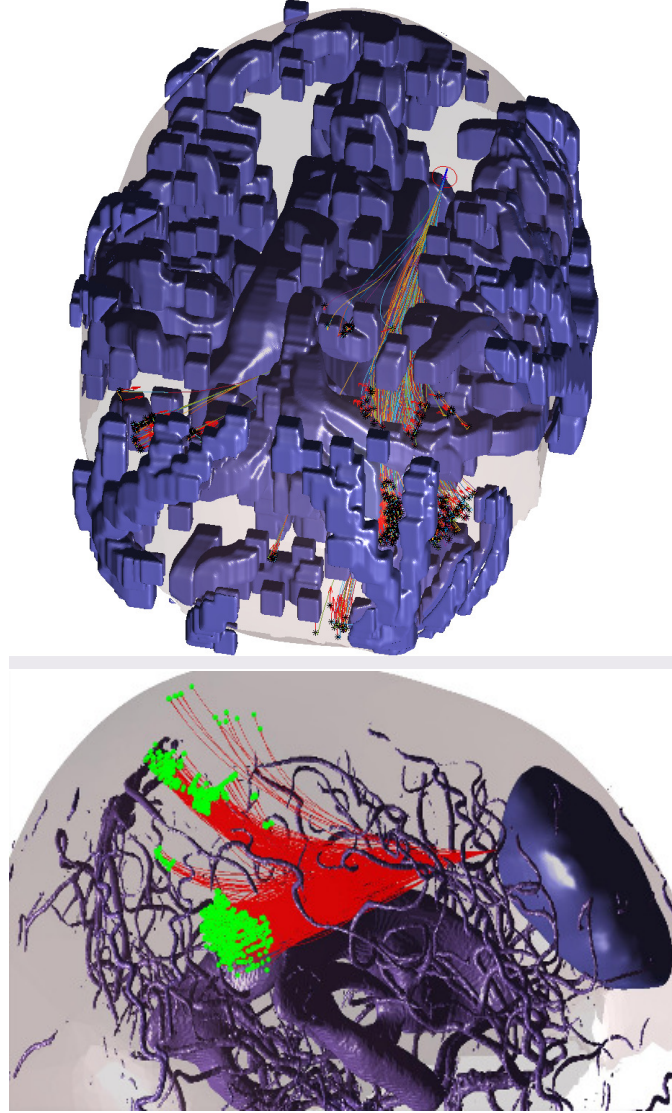
Figure 3.8: The obstacle map includes a margin that takes into account both the cross section of the needle and a safe distance from obstacles (Top image). In the bottom, the AFT obstacle-free paths (red trajectories) combined with a ray-tracing algorithm select those paths intersecting the skull perpendicularly (green points). The highlighted sub-regions on the skull (pink areas) contain multiple possible entry poses from which it is feasible to reach the required target pose meeting the kinematic constraints of the PBN.

In both scenarios, a similar procedure is followed to process the available medical images and
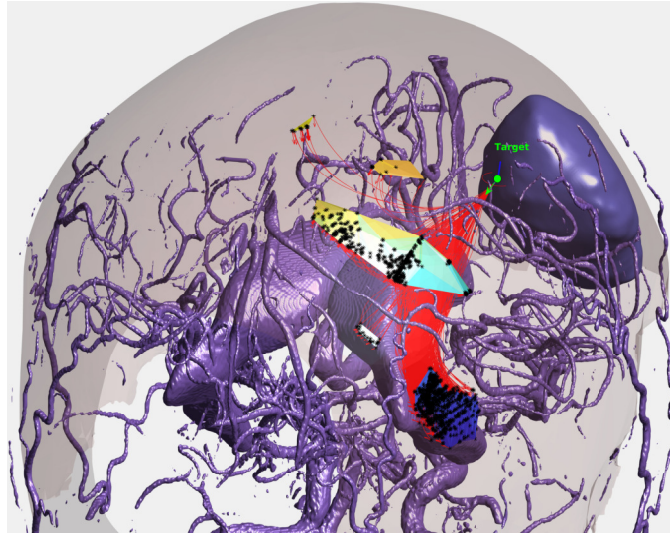
Figure 3.9: The Ray-traced generated paths are ranked according to a cost function accounting for maximum length and smoothness. This aims to aid the path selection by highlighting sub-regions on the skull contain the resulting entry points with different colours depending on their respective cost function value. The yellow region is associated with better results in terms of cost function.

create the expected path planner input data. Brain ventricles and vessels are segmented and saved as meshes with 3DSlicer (www.3DSlicer.com), using region growing and vessels extraction tools respectively. The patient CT image has, instead, been used to segment the skull by a thresholding method, creating a mesh from its surface. Then, a rasterised obstacle map, of size equal to a bounding box containing all the previously listed meshes is generated as described in Section 3.2. The resulting map is dilated by a value equal to 1.6 mm. This safety margin includes both the occupancy of the EDEN2020 catheter (1.25 mm in radius) and an arbitrary safety distance to account for real-world inaccuracies. The tumour segmentation and the optimised target pose generation is performed by the EDEN2020 convection enhanced delivery model [ZDB19]. At this stage, the Ray-Traced AFT is run from 61 different target poses originating from the same target position, laying on the same plane and uniformly covering multiple directions at 360 deg. In a real case scenario, clinicians could select the desired target pose or a number of acceptable ones. For each simulation the search tree expands throughout the obstacle map until eventually crossing the skull.

We ensure the AFT expansion to reach the skull by setting the total expansion of the tree to 100 mm, the maximum achievable length for our needle. A branch length of 20 mm and

a density of the tree of 17 were also set to increase the probability of finding obstacle-free solution within a very cluttered environment such as the human brain. A detailed tuning of the AFT fundamental parameters (such as branch length and density) with respect to the AFT performance can be found in Chapter 4.

A value of 15 degrees (*tol*) has been decided, in agreement with neurosurgeons, as maximum misalignment of the resulting AFT obstacles-free path with respect to the normal of the skull at the intersection point. A total of Ray-traced AFT paths can be seen in Figure 3.9; they all cross the skull with an angle within the given tolerance. The algorithm's computational time has been calculated on a workstation with an NVIDIA GeForce GTX 1080 Ti 11GB Pascal. Thanks to its GPU implementation, the computational time does not suffer from variations while the average computational time, calculated from the 61 simulations, is equal to 2.3 sec.

A fast computation allows the surgeons to interactively modify the target pose if needed and recompute the corresponding feasible paths. The resulting path entry points, on the skull surface, are classified into independent feasible entry point regions which are then exported as a unique mesh. The cost function (Section 3.4) can be used to rank the resulting paths and associated entry points. In particular, different colours can be attributed to them depending on their scores. This visual feedback can further aid clinicians in choosing the smoothest and shortest path to follow or more generally a region on the skull from where well-ranked paths begin.

3.6   Conclusion

The Ray-traced AFT algorithm is proposed as a valuable extension to the standard AFT path planner in the field of steerable needles for neurosurgery. In particular, the Ray-traced AFT meets both the kinematic constraints of a steerable needle and the surgical constraints on the required entry pose, target pose and obstacles' minimum clearance from sensitive structures. The Ray-traced AFT is, therefore, a valuable tool for neurosurgeons during the pre-operative phase of a steerable insertion. It allows them to visually map the patient skull, highlighting

those regions from where safe and feasible paths can be followed and finally select one of the proposed trajectories. However, it can happen that neurosurgeons want to manually select both entry and target pose. For this purpose, in Chapter 4, we will address the development of a second AFT-base preoperative planning called Adaptive Hèrmite Fractal Tree (AHFT) that is able to meet constraints on both selected entry and target poses. This technique can be either used alone for a given entry-target pair or, in combination with the Ray-tracing AFT. In the second case, the Ray-tracing AFT maps the patient skull with the successful entry-points while the AHFT refines these solutions by constraining the entry pose to be perfectly perpendicular to the skull and by generating multiple paths from a single entry pose.

Chapter 4

Path Planning for Steerable Needles: Adaptive Hérmite Fractal Tree

In this chapter, a pre-operative path planner for steerable needles is presented. The research presented is an edited version of research previously published in:

Marlene Pinzi, Stefano Galvan, and Ferdinando Rodriguez Y Baena, "The Adaptive Hérmite Fractal Tree (AHFT): a novel surgical 3D path planning approach with curvature and heading constraints." International journal of computer assisted radiology and surgery, vol. 14, no. 4, pp. 659–670, april 2019.

4.1   Introduction

The taxing kinematic constraints behind PBNs [LGCSR16, LOR16] and the complexity of a 3D anatomical obstacle map which includes both brain vessels, eloquent areas, and brain ventricles, contribute to making path generation within the EDEN2020 context particularly challenging. Moreover, in complex neurological planning such as the one proposed in EDEN2020, both the pose of the entry key-hole in the skull and the pose of the drug delivery target site might need to be defined *a priori*.

However, the original AFT and the proposed AFT Ray-traced (Chapter 3) algorithms are not able to deal with both starting and final heading constraints. Specifically, while the direction of growth of the tree can be changed according to the required starting heading, the final heading is not taken into account during path planning. For this reason the AFT Ray-traced technique is applicable to scenarios with no specification on the entry point or, as explained in the previous chapter, for skull mapping purposes followed by an entry point selection. Existing RRT-connect algorithms [FSM18b] can meet start and target heading constraints but they rely on geometrical techniques, such as Dubin's curves based methods, to meet the curvature constraint at the trees connection points. These geometrical techniques are not extendable to high curvature constraints which are required by the majority of existing steerable needles prototypes (i.e. [SBGW13, FKT+10a]).

Following these considerations, the Adaptive Hermite Fractal Tree (AHFT) path planner is proposed in this work. Thanks to some important properties related to a particular kind of Hermite curves called optimized geometric Hermite curves (OGH), the AHFT is able to account for both heading constraints accurately. The AHFT could be useful as a AFT Ray-traced refinement to find more path from the selected entry pose or, from scratch, in case both heading constraints are set from the beginning. Given two endpoints and two endpoint tangent vectors, a cubic polynomial curve is called an OGH curve with respect to the given endpoint conditions if it has the smallest strain energy among all cubic Hermite curves satisfying the conditions on starting and final pose and is also geometrically smooth [YC04]. This specific property allows us to use OGH curves to extend the AFT obstacle-free paths at different positions along candidate trajectories. For each linking position, the local tangent is computed, which is subsequently employed as the starting heading for the Hermit curve connecting the AFT path to the desired target pose. Finally, a voxel-based obstacle collision and a maximum curvature check are performed on the Hermite extension with the same voxel-based modality of the AFT but evaluating one path at the time. Only feasible paths are returned.

In this Chapter, the AHFT implementation is described in detail; it follows a quantitative robustness evaluation of the proposed preoperative planner by mean of a realistic computer-simulated environment. The flexibility provided by computer simulations under tunable condi-

tions allows to test the AHFT robustness to specific events or perturbations while eliminating the influence of other factors if needed.

4.2   Adaptive Hermite Fractal Tree Method

4.2.1   AFT automatic parametrization

Starting from the original AFT algorithm described in Chapter 3, Section 3.3.1, an automatic parameter tuning process for our AFT implementation is designed to maximize the number of paths generated in a neurosurgical scenario and to exploit the entire GPU memory available during fractal tree parallel construction. To do so, it is necessary to understand the relationship between the parameters l (branch length) and ρ (tree density) on AFT performance, an objective that we pursue through a brute force search of the parameter space.

The AFT density relates to the total number of segments composing the tree which, if beyond a threshold (Number of GPU cores * 10, and equal to 25600 for our workstation), can cause the GPU to have to iterate in order for all the segments to be processed, thus increasing computation time. On the other hand, l affects the number of subsegments composing each branch through which the obstacle collision has to be performed. This part of the code runs in parallel for every segment and influences the total amount of simulation time. In this study, the interpolation constant determines the resolution of the obstacle collision check performed for each tree branch. In order to set its value, blood vessels are segmented from a representative and anonymized MRI image volume [CF19] via standard thresholding (www.slicer.org). Next, the branch length l is assigned to one of the following values: 20, 30, 40, and 50 mm. This set is chosen in order to measure the AFT's behavior across a representative range. In particular, the minimum branch length of 20 mm comes as a result of two existing constraints, one on the maximum reachable needle length of 100 mm and the other one on the required GPU memory space which limits the tree growth to a maximum of 5 levels of increments of the fractal structure, with a density value of up to 17. Therefore, the lower limit of 20 mm has

been selected as the minimum acceptable branch length value in order to cover a distance of at least 100 mm in five steps of tree growth. On the other hand, the upper limit, which cannot be more than the total path length, has been set to 50 mm in order to cover the search space with the minimum number of 2 turns. Branch lengths of 30 mm and 40 mm are chosen to assess the performance in the case of 4 and 3 increment levels, respectively. Knowing the specified branch length and the corresponding necessary levels of tree growth to cover the maximum needle extension, we can then use the exponential law governing tree growth in order to compute the total number of AFT branches needed, each of which occupies a thread of the GPU memory (Equation 4.1).

$$AFT_{branches} = \sum_{i=0}^{tree_{levels}} (branch_{density})^i \tag{4.1}$$

where $tree_{levels}$ represents the number of levels of tree growth and $branch_{density}$ represents the density of the tree ρ. Ultimately, the density of the AFT is set to one of these values: 9, 17 or 33. These define the number of branches forming the basic fractal structure, which has to be equal to a multiple of 4 (up, down, right, left) plus 1 (straight). A high tree density increases the mapping capability of the AFT, but this value must be limited to 33 in order to meet the GPU (NVIDIA GeForce GTX 1080 Ti 11GB Pascal) memory constraints (3072 cores, 12288MB total memory), at least with the longest branch selection of 50 mm. Of particular importance is understanding the trade-off relationship between ρ and l in terms of computational cost and AFT outcome. We explore this via a brute force search of the parameter space, where the initial tree space orientation is also considered as variable. The tree can be oriented towards random points inside a circumference around the target, which lies on the plane perpendicular to the line subtended between insertion and target points. This further variability increases the number of cases explored.

We executed a total of 1260 simulations on our workstation, varying parameter values as discussed above. Each path is evaluated by the cost function (CF) described in Chapter 3, Section 3.4.

4.2.2   AHFT algorithm implementation

The AHFT is implemented with two main routines. The first identifies whether a given start-end pose combination is feasible. The second computes the optimum continuous path between the two, which meets the needle's constraints and is obstacle free.

Step I: Start and Target Pose Reachability Check   A feasibility check is performed once the path planner is invoked as a means to ascertain whether the start and target pose combination is feasible either in terms of maximum needle length or in terms of needle kinematic constraints, such as the maximum curvature constraint (k_{max}). We define a "reachable volume" by considering the intersection of the two bounding volumes which enclose all branches of the two AFTs, the first rooted at the start pose and the second at the target pose. If no intersecting volume which encompasses both poses is available, the algorithm cannot progress.

Step II: Optimized Geometric Hermite (OGH) Extension   Before defining an Optimized Geometric Hermite (OGH) curve it is appropriate to introduce the wider class of Hermite curves. The following paragraph refers to the results presented in [YC04], which are of particular interest for our application. The verbatim-copied parts are enclosed in quotation marks.

"A cubic Hermite curve Q(t), $t \in [t_0, t_1]$ where $(t_0, t_1) \in R$ and $t_0 < t_1$, is a cubic polynomial curve satisfying the following endpoint location and tangent vector conditions: "

$$Q(t_0) = P_0, Q(t_1) = P_1, \overline{Q}(t_0) = V_0 \overline{Q}(t_1) = V_1 \qquad (4.2)$$

where P_0 and P_1 are the start and end point coordinates, and V_0 and V_1 represent the desired approach direction for P_0 and P_1, respectively. Q(t) can be expressed as follows:

$$Q(t) = (2s+1)(s-1)^2 * P_0 + (-2s+3)s^2 P_1 + (1-s)^2 s(t_1 - t_0)V_0 + (s-1)s^2(t_1 - t_0)V_1$$
$$(4.3)$$

where $s = \frac{t-t_0}{t_1-t_0}$.

"The strain energy of a C²-continuous curve f(t) defined on $[t0, t1]$ is defined as follows:

$$\int_{t_0}^{t_1} [f(t)'']^2 dt \tag{4.4}$$

where $[f(t)'']$ is the second derivative of f(t). A Hermite curve is mathematically smooth because it has the minimum strain energy among all C¹ cubic polynomial spline curves satisfying the same endpoint conditions".

Between similarly smooth Hermite curves, we select the one with the minimum strain energy which is also mathematically smooth by optimising the magnitudes of the considered endpoint tangent vectors. This curve is defined in [YC04] as an optimized geometric Hermite (OGH) curve.

Given two endpoints P_0 and P_1, and two endpoint approach vectors V_0 and V_1, an OGH curve is the cubic Hermite curve Q(t), $t \in [t_0, t_1]$, with the smallest strain energy, and which also satisfies the following conditions:

$$Q(t_0) = P_0, Q(t_1) = P_1, \overline{Q}(t_0) = a_0 V_0, \overline{Q}(t_1) = a_1 V_1 \tag{4.5}$$

where a_0 and a_1 are arbitrary real numbers that relate to the magnitude of the curve approach vector in P_0 and P_1, respectively. In this study, we consider $a_0 = a_1 = a*$ to enforce similar conditions for both start and end pose alignment. In some cases, one might want to hold the ratio of the tangent vector magnitudes unchanged in order to maintain a fixed shape style on the resulting curve, avoiding higher curvature values at one proximity. Therefore, we give $a*$ the value suggested in [YC04].

$$a_0 = a_1 = a* = \frac{3[(P_1 - P_0)(V_0 + V_1)]}{2(V_0^2 + V_0 V_1 + V_1^2)(t_1 - t_0)} \tag{4.6}$$

In the AHFT, OGH curves are used as extensions which depart from the AFT obstacle-free paths at different positions along the trajectories and connect them to the target point with a predefined orientation (Figure 4.1). First, the optimized AFT algorithm described in Section
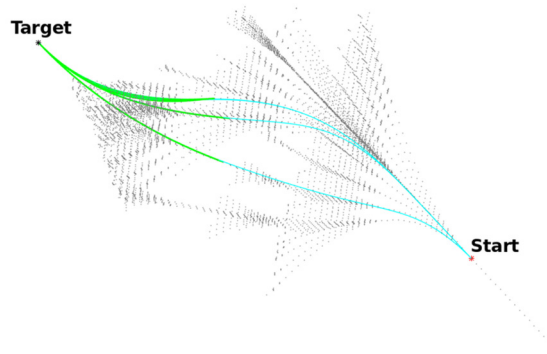
Figure 4.1: Three feasible paths, generated by the AHFT path planner, connect the requested start and target pose. In gray: the AFT tree branches laying between the feasible volume; in light blue: the AFT portion of the paths; in green: the OGH portion of the paths.

4.2.1 is used as a method to explore the search space. Only the branches which do not collide with obstacles and which lie within the "reachable volume" identified in Step I are considered, and candidate paths are computed as per the original AFT algorithm. At this point, every point of all trajectories found so far, is considered as the initial point during the AFT extension through OGH curves, which is described next. The OGH curves for all candidate extension paths are chosen such that each one is tangent to the AFT path on one side, and the desired target pose on the other. Subsequently, the generated OGHs can be easily expressed as a Bézier curves with four control points. The cubic polynomials, expressed in Bézier form, allow for an easier computation of the curvature values along the paths. Once a voxel-based collision check and a curvature checks are performed also on the candidate extensions, viable AHFT paths are considered as possible solutions and the cost function is employed to rank these in order of performance. Finally, we use a function called "interparc" (author: John D'Errico [D'E12]), available on the Matlab (Mathworks Inc.) file exchange server in order to obtain equally spaced points along the considered paths.

4.3   Results

4.3.1   AFT performance parameters significance

As already discussed in Section 4.2.1, we executed a total of 1260 simulations, 105 for each combination of parameters which can vary as shown in the table (Table 4.1). In particular, the AFT density ρ can take the following values: 9, 17 or 33, while the AFT branch length l can be equal to 20, 30, 40 or 50 mm, values which are associated to the following tree expansion numbers, respectively: 5, 4, 3, 2. In this specific scenario, start and target points are chosen to be at the maximum acceptable distance with respect to the needle length. Additionally, the AFT algorithm has been iteratively run rotating the tree around an axis corresponding to its root (the entry pose) for ten times in $pi/5$ degree steps in order to achieve a even more homogeneous and dense expansion through the 3D search space.

These first results show that the branch length or, more generally, the related number of tree increments, have a particularly strong influence on the memory requirements. Indeed, they directly affect the number of segments of the tree and, therefore, the number of generated paths (Figure4.1). Setting $l = 20$ mm, the maximum acceptable value of ρ within the memory constraint is equal to 17. This combination produces at least one AFT path 94.23% of the times, with an average computation time of 0.22 sec and an average number of solutions equal to 408.51; while, increasing the branch length, the percentage success rate decreases to 72.12% for $l = 30$ mm (4 levels of growth) and then drops to 36.54% for $l = 40$ mm (3 levels of growth) and to 25.00 % for $l = 50$ mm (only 2 levels of growth). For smaller values of AFT density, as for $\rho = 9$, the performance of the AFT is still high, with a 90.48 % success rate. The average number of paths found is only equal to 32.82, but this is in favour of a lower computation time of 10.65 ms. Because we are interested in maximizing the AFT's mapping ability in a complex environment, the number of generated paths together with the percentage success rate are considered as the most important indexes assessing the robustness of the method in finding solutions. Therefore, 5 levels of tree increments and $\rho = 17$ are selected as the best combination for future trials. The computation time in a pre-operative scenario is secondary with respect

to the quality and robustness of the planning. In addition, the difference in computation time for $l = 20\ mm$ between $\rho = 17$ and $\rho = 9$ is due to GPU overflow, as described earlier. This unwanted side effect of an excessive number of segments would disappear if using a multi-GPU implementation or a different GPU featuring a higher number of threads was employed. In other words, an increase in ρ would not affect the computation time for one GPU thread or the computation time for any given iteration, as long as the GPU features a sufficient number of threads to service all tree branches in one run.

Following these results, an automatic parametrisation method was developed to enable case-specific AFT efficiency optimization, as follows:

- Select the number of AFT levels (N) and AFT density ρ according to hardware constraints.

- Compute the branch length value necessary to cover the search space through the N-level AFT growth based on the distance between a given start and target positions (which can be less than the predefined $100\ mm$ used during the previous simulations).

This optimization method, applied to our test case, results in a 5-level AFT, with an AFT density equal to 17, which results in 1,508,597 tree branches. This resulting optimized AFT is used to demonstrate AHFT performance in subsequent sections. Three different tests were performed to assess the performance of the AHFT-based path planner. The first two focus on the robustness of the AHFT to changes in target pose and final heading, respectively, with no obstacles included in the search space. These tests explore the ability of the algorithm to respond to changes in the plan incurred due to, e.g., tissue deformation, deliquoration and pulsatile motion. These tests have been performed without the influence of obstacles in order to assess algorithm's performance and observance of constraints under perturbations.

The last test involves the simulation of a pre-operative scenario, which enables the assessment of the AHFT within a complex network of realistic obstacles. Here, the use of our "reachable volume" computation (Section 4.2.2) to automatically support user selection of a viable entry point is also described. Such a tool is expected to simplify the planning process in complex neurosurgical scenarios, where the range of feasible paths is highly restricted.

Length: 20 mm (5 Levels)

Performance	*Density*		
	9	**17**	**33**
success rate	90.48%	94.23%	out
avg n path	32.82	408.51	out
avg time	10.65 ms	223.28 ms	out
tot paths	3118	40034	out

Length: 30 mm (4 Levels)

Performance	*Density*		
	9	**17**	**33**
success rate	40.00%	72.12%	86.40%
avg n path	5.26	18.27	117.77
avg time	2.79 ms	18.41 ms	247.8 ms
tot paths	221	1370	10640

Length: 40 mm (3 Levels)

Performance	*Density*		
	9	**17**	**33**
success rate	20.95%	36.54%	53.39%
avg n path	1	3.71	8.47
avg time	1.41 ms	2.85 ms	10.76 ms
tot paths	22	141	481

Length: 50 mm (2 Levels)

Performance	*Density*		
	9	**17**	**33**
success rate	20.95%	25.00%	34.95%
avg n path	1	1.04	10.89
avg time	1.08 ms	1.32 ms	3.05 ms
tot paths	22	27	403

Table 4.1: AFT parametrisation: Success rate, average number of paths found, average computation time and total number of paths found for 150 trials, for each combination of length (l), and density (ρ).

4.3.2   AHFT robustness evaluation

Here we evaluate the ability of the AHFT to identify feasible paths for the following set of needle kinematic constraints: curvature continuity, maximum curvature ($k_{max}=\frac{1}{70}mm^{-1}$) and needle length ($l=100mm$). Starting with the trivial case of a straight line path between the entry and target pose, we then systematically alter both the position and the approach vector of the target pose to explore the bounds of the solution space. In doing so, we provide a visual and quantitative representation of needle performance, confirming correct execution within the solution space.

Target Orientation Sensitivity   To ascertain the sensitivity of the algorithm to target approach vector changes, a setup with coaxial start and end approach vectors is considered, then the target approach vectors are displaced with steps of one degree towards a certain direction until no solution is found. This is repeated for 21 displacement directions that constitute the rays of a polar grid where the angular spacing is equal to $\frac{\pi}{10}$. Each approach vector was then considered as the target approach vector for an AHFT run, maintaining the same target position and the same starting pose for all pairs within this test.

Results are provided in Figure 4.3, where the success rate for each displacement degree is calculated as the number of times at least a path is found with respect to the total number of directions evaluated. The green points identify those target approach vectors for which at least one path could be found, while red points correspond to those for which no paths were found (Figure 4.2). From these results, solutions could be found for all target coordinates within 23 degrees of the coaxial start and target scenario. The success rate, defined as the number of target points providing at least one AHFT solution, decreases to 66.66% for a deviation of 24 degrees, to 47.61% for 25 degrees and finally to 14.29% for 26 degrees, which is the maximum deviation for which we can still find some solutions.

Target Placement Sensitivity   To ascertain the sensitivity of the algorithm to target placement, the following setup was employed. Starting with the trivial case of a straight line path
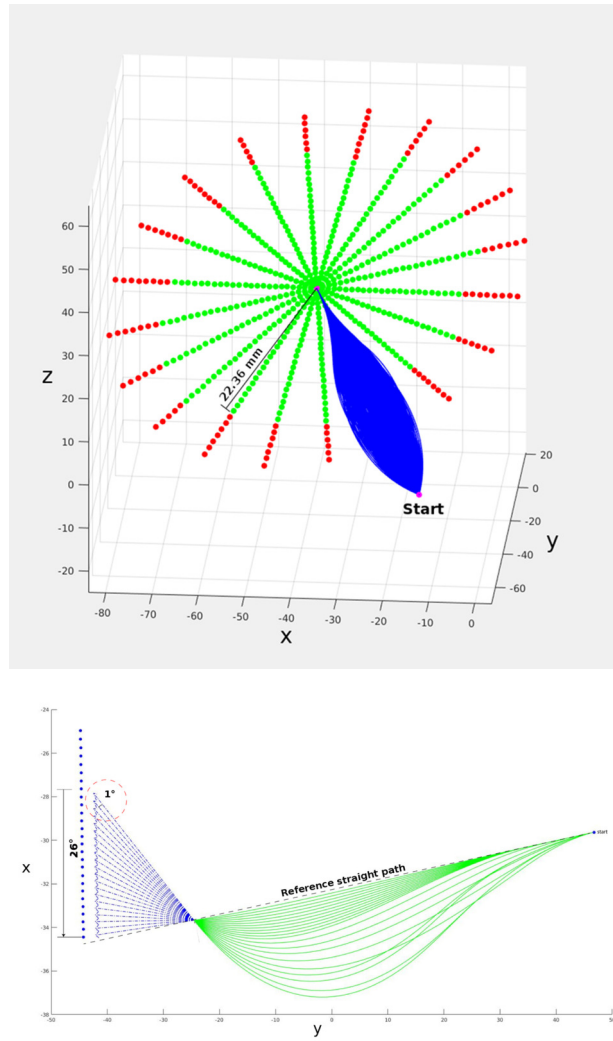
Figure 4.2: AHFT robustness evaluation for target approach vector: given a target position and an initial pose, the final approach vector is systematically oriented away from the trivial case until no solution is found. A red point corresponds to an approach vector for which no paths are found, while green points correspond to successful runs. At the bottom, the solutions corresponding to a single ray of the polar grid are displayed

with coaxial start and end approach vectors, target coordinates were discretized within the same polar grid described in Section 4.3.2, maintaining both approach vectors constant. Each point within the grid was then considered as the target for an AHFT run, maintaining the same starting pose for all pairs within this test.

Results are provided in Figure 4.4, where green points identify those targets for which at least one path could be found, while red points correspond to those for which no paths were found. From these results (Figure 4.5), it is evident that solutions could be found for all target coordinates within a 22.36 mm radius circle from the center. Once again, these results confirm
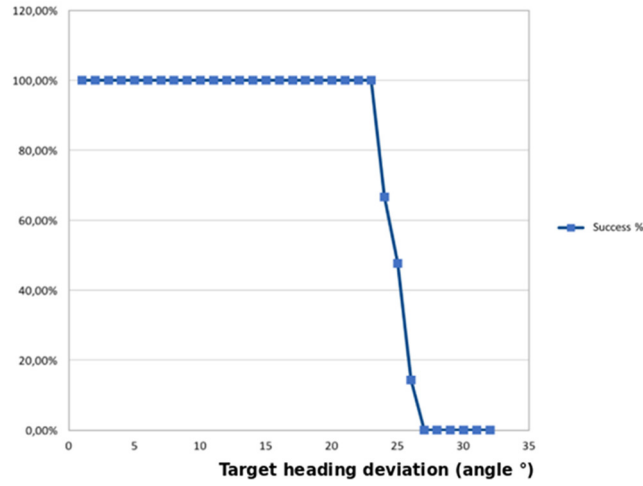
Figure 4.3: The graph shows the AHFT success rate with respect to an increasing deviation of the target heading from the coaxial start and target scenario.
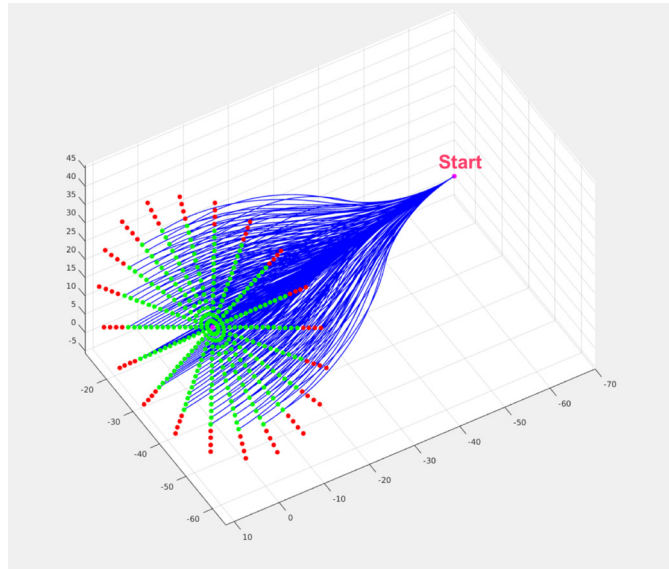
Figure 4.4: AHFT robustness evaluation for target placement: given a final approach vector and a fixed starting pose, the target position is systematically moved away until no solutions can be found. A red point indicates that no paths are found for the given target position, while a green point corresponds to a successful run.

the ability of the AHFT algorithm to identify suitable solutions within the feasible space.

Pre-operative Path Planning Simulation   In a pre-operative neurosurgical scenario, the operating surgeon would generally select a suitable entry point for the needle on the skull of the patient. Entry poses perpendicular to the patient's skull are calculated for each of the patient's skull mesh vertex points using the correspondent surface normals. The entry-pose decision has to account for the desired target pose (i.e. the position and orientation of the needle at the
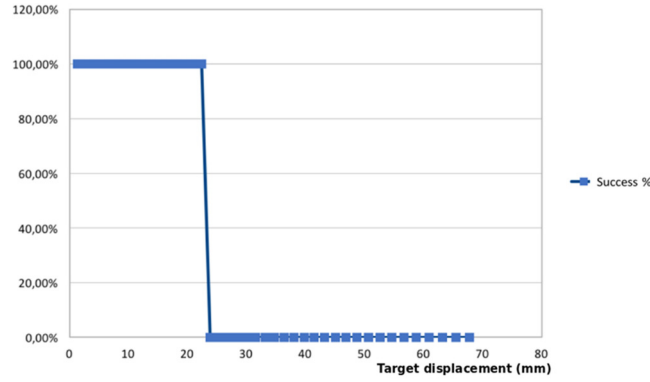
Figure 4.5: The graph shows the AHFT success rate with respect to an increasing displacement of the target away from the polar grid center.

point of application) and any cortical functional areas that must be avoided. Additionally, the approach angle at the start of the needle insertion process should be roughly perpendicular to the skull at the desired entry point in order to facilitate the creation of a suitable burr-hole. Consequently, the selection of a feasible starting pose is not straightforward. To aid in this process, each vertex of a homogeneously distributed skull mesh is considered in turn (total number of vertices = 1702), where the coordinates represent a possible entry point, and the associated vertex normal represents the corresponding desired start approach vector. All feasible entry points for a given target pose are then identified by executing the feasibility check for each pair, as per Section 4.2.2. The green dots within the light blue region are those for which the AHFT is able to find at least one trajectory, while the red dots are those for which no paths can be found because of obstacle collisions, which are not accounted for during the feasibility check. For illustrative purposes, a second mesh is produced out of the green successful vertices, in such a way as to highlight the skull region which would be suitable for a given target pose. Such a region is highlighted in light blue in Figure 4.6, as an illustrative case, alongside a complete set of feasible paths (dark blue) for a representative target pose close to a tumor.

The skull mapping was performed for 15 different target poses. The average computation time for every start and target pose pair was 24.67 *sec*, with a high standard deviation (25.76 *sec*) because the path planner was run until the first solution was found, leading to different times depending on task complexity. The target pose success rate for all runs is shown in Figure 4.6.

Each rate has been computed considering the number of feasible entry poses from which at least a path could be found with respect to the total corresponding amount of feasible points for the considered target pose. The fact that, for some target headings, few solutions could be found is mainly due to the density of the obstacle map and the complexity of the selected case in terms of start and target poses. These target poses are possibly those which a surgeon should exclude in favour of ones highlighted in the subregions, which would guarantee a better coverage of the feasible area on the patient skull (red dashed target pose in Figure 4.6).
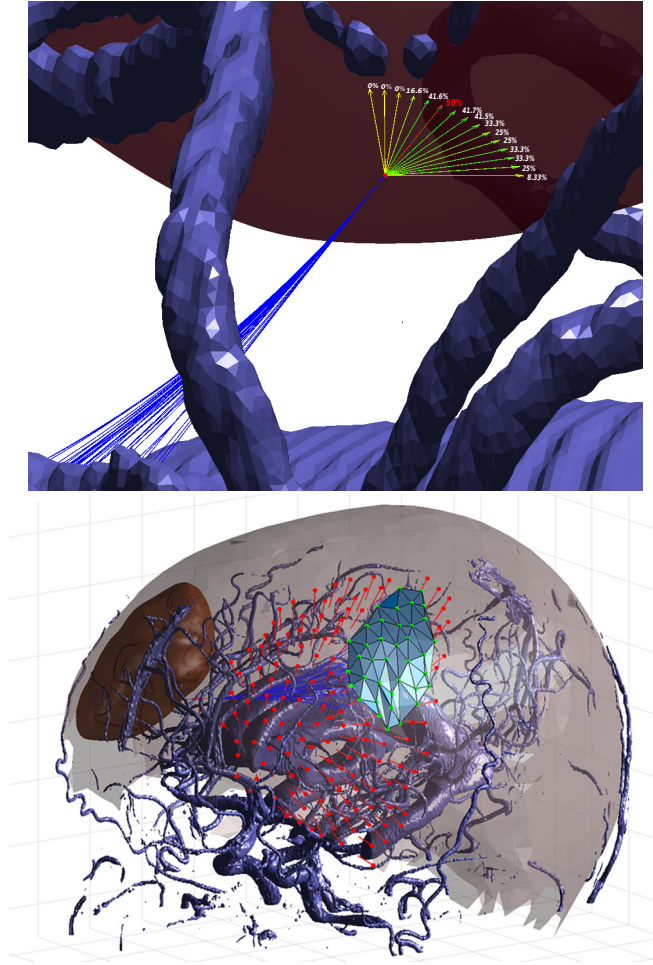
Figure 4.6: Pre-operative scenario simulation: For each one of the displayed target poses laying near the tumor (brown), a rate has been calculated considering the number of feasible entry poses from which at least a path could be found with respect to the total skull mesh vertices. On the bottom, the best target pose (in terms of rate) is considered, and a skull region (light blue) is displayed to highlight the surface area where a burr-hole could be placed. Within this highlighted region, all feasible paths between each mesh vertex and the target are depicted in blue. Vertices in green are associated to obstacle-free paths, while red vertices are those for which an obstacle-free path could not be found.

4.4 Discussion

Starting with the trivial case of a straight line path between entry and target pose, systematically changing both the position and the approach vector of the target pose resulted in a set of results which confirm the ability of the AHFT algorithm to identify suitable candidate paths, if they exist. As the simulated setup explored increasingly challenging pose configurations (i.e. those lying at the edges of the solution space), more complex trajectories were required to intersect the target pose, implying a greater risk of failure. The AHFT algorithm is thus able to find at least one path for a given set of needle constraints, as long as the AFT sampling space lies within the "feasible volume" identified in Section 4.2.2. The AHFT is a sampling based method which, because of its discrete nature, does not guarantee an optimum solution. However, the fractal tree structure provides a dense, invariant and organized exploration of the entire domain ensuring high robustness and success rate in path planning for highly constrained and complex environments. The top-ranked generated trajectories with respect to a specific cost function are those to be selected. The AHFT architecture also leads itself to full parallelization, unlocking the massive computational speedup capacity of the GPU, leading to a potential for intra-operative use. The differences in the experimental setup, ways to access the methods, software and hardware used make it difficult to compare the performance of path planning algorithms completely. Additionally, the very different constraints related to medical applications influence the complexity of the problem, making path planning algorithms very case-specific and even more difficult to assess. However, with respect to the pre-operative simulation scenario, the proof of concept results described in Section 4.3.2 demonstrate that the AHFT is able to identify a path planning solution if one can be found, and that the method can be used to identify a dense set of viable skull entry points within a preferable skull entry region, for a given target pose and set of needle constraints, automatically. Clinicians would still be free to select any other point within the highlighted skull region/s, as needed. The method, therefore, can offer an important tool to assist and facilitate planning in the most complex surgical scenarios. The surgeon can be assisted in identifying a suitable location for the burr hole, which is both clinically safe and feasible, with full control over both the entry

and target needle poses.

4.5   Conclusion

In this work, we proposed the Adaptive Hermite Fractal Tree, a novel parallelizable 3D path planning approach able to cope with the kinematic constraints of a steerable needle and predefined start and target poses. The performance of the algorithm to perturbations in the target position and approach vector were evaluated. Additionally, the AHFT was tested in a preoperative neurosurgical simulated environment, which demonstrates that multiple viable paths can be identified through a complex network of realistic obstacles. The method also enables easy identification of a suitable entry area on the patient skull for a given choice of target pose, which would be a useful tool for the surgeon. AHFTs can be applied to other fields where explicit control on entry and target poses, and a parallelizable architecture, are required. In Chapter 5 we will address the development of methods for intra-operative path adaptation. At this stage of the surgery, an algorithm's time efficiency is key. Furthermore, different solutions that account for occurring tissue deformations and real-world inaccuracies are needed to keep proximity to the preoperative path and accurately reach a desired target, specially when both start and target pose are predefined.

Chapter 5

Adaptive Path Replanning for Orientation-constrained Needle Steering

Chapters 3 and 4 focused on pre-operative path planning solutions. In this chapter, a intra-operative path planner for steerable needles is presented. The aim of this study is to develop a new intra-operative planning approach and test its computational performance both in simulation and in-vitro, together with its integration in a surgical robotic setup, which is presented in Chapter 6. In-vitro trials were carried out to evaluate planner's performances in finding feasible solutions at a time rate that is acceptable for its integration within the EDEN2020 robotic system.

Ex-vivo and in-vivo experiments were planned to further assess the proposed intra-operative planner, but they have unfortunately been postponed due to COVID19 outbrake.

The research presented is an edited version of recently published study:

Marlene Pinzi, Tom Watts, Stefano Galvan, Riccardo Secoli and Ferdinando Rodriguez Y Baena, "Path Replanning for Orientation-constrained Needle Steering" Transaction in Biomedical Engineering (TBME), February 2021.

5.1   Introduction

Minimally invasive surgery and treatment represents a major trend in current neurosurgical procedures, minimizing patient trauma, and thus the risk of complications and recovery time [APM07]. Steerable needles are a promising technology within this field, allowing clinical access to previously inaccessible anatomical targets. By steering along low-risk preoperatively computed paths, the safety of percutaneous procedures is increased. To control the insertion during steerable needle procedures, the surgeon usually operates with the aid of a robotic platform. With a suitable interface and model of the needle, surgeons can intuitively control steering without needing to understand the specific needle mechanics. However, the accuracy of the needle insertion with respect to the preoperative selected path is affected by several factors. The first factor is tissue deformation, primarily caused by fluid loss occurring during the creation of the burr-hole port on the patient's skull, a phenomenon known as "Brain shift" [IYS+14]. Targeting accuracy is also affected by poor quality medical imaging, unpredictable needle-tissue interactions, and surgeon errors [LKR18]. Steerable needles must also avoid colliding with anatomical structures such as brain vessels and ventricles which may deform during insertion.

Due to these considerations, the path selected preoperatively should be reassessed during the procedure to verify its feasibility with the new deformed obstacle configuration.

To account for the surgeon's preoperative evaluation of the necessary surgical intervention, it is desirable to design a replanning algorithm which adjusts the existing surgeon-defined path rather than replacing it, compensating online for deviations of the tip and tissue deformation while maintaining high "path similarity": a measure of the deviation a process induces between an original path and a new (target) path. Preserving path similarity reduces the cognitive load on users observing the planned activity, by ensuring coherence and consistency of behaviors, even in dynamic environments [NKS+]. Also, less changeable plans reduce stress on hardware execution components, facilitating the PBN's motion.

On the other hand, a comprehensive computer-assisted planning method should be able to meet new constraints deriving from precision neurosurgery applications which demand high accuracy

in target orientation, such as in Convection Enhanced Delivery (CED) [ZW18b] or Deep Brain Stimulation (DBS) [SPF+19b].

Global path planning methods are generally favored with respect to local ones for online needle steering applications since, besides reacting to local changes and unexpected obstacles, they can deal with the global problem of reaching an arbitrary goal. The most common technique is to apply a single-query planner that is fast enough to be used intra-operatively to replan the trajectory from imaging or sensing feedback information as in [PBWA14]. As we discuss in the literature review (Chapter 2) Rapidly Exploring Random Tree (RRT) based solvers are generally favored because they maintain good performance even in a 3D anatomical environment [PBWA14]. However, their maximum run time is user-defined, leading to a trade-off between speed and success rate. Therefore, at equal maximum run time, a more complex obstacle map would lead to a decrease in success rate [FSM18a]. Additionally, RRTs generally do not include needle curvature constraints and target orientation accuracy is generally not considered. Only recent RRT spline-based solutions can meet constraints on both a specified target orientation and on a maximum curvature radius, without requiring further smoothing [YMY+14, FSM18a]. However, these solutions are limited by their geometrical approach which, as in the case of Dubin's curves [PHB17], bound the maximum curvature radius up to half the distance between the start and target point [Moh15].

"Bubble Bending" algorithms [QKa][LT11], coupled with optimised trajectory smoothing methods [ZSP15] provide an elegant solution to these problems. In general, "Bubble Bending" is based on the online modification of a predefined path. The path behaves as an elastic band, reacting in real-time to local changes in a dynamic environment. The power of this framework is that it avoids the computational cost and the risk of long path detours associated with re-calling a global path planner as is required in RRT based methods: local modifications to the original path do not limit the ability to achieve global goals. A disadvantage of the approach alone, however, is that the resulting path curvature is generally not bounded. Constrained path smoothing methods, such as the Convex Elastic Smoothing (CES) algorithm, has been developed to address this and implemented for 2D car-like robot applications [ZSP15].

In this study, we present a modified version of the "Bubble Bending" which has been adapted to the surgical environment to be able to compensate for both tissue deformation and real-world uncertainties. Additionally, an extension of the CES for 3D scenarios is incorporated, which can find a curvature constrained solution suitable for steerable needle navigation. Our replanning method continuously generates an updated path which meets the desired target orientation and position constraint accuracy while meeting surgical and curvature constraints. The "path similarity" is also optimised to make the algorithm more predictable to users and interaction with the front-end potentially easier.
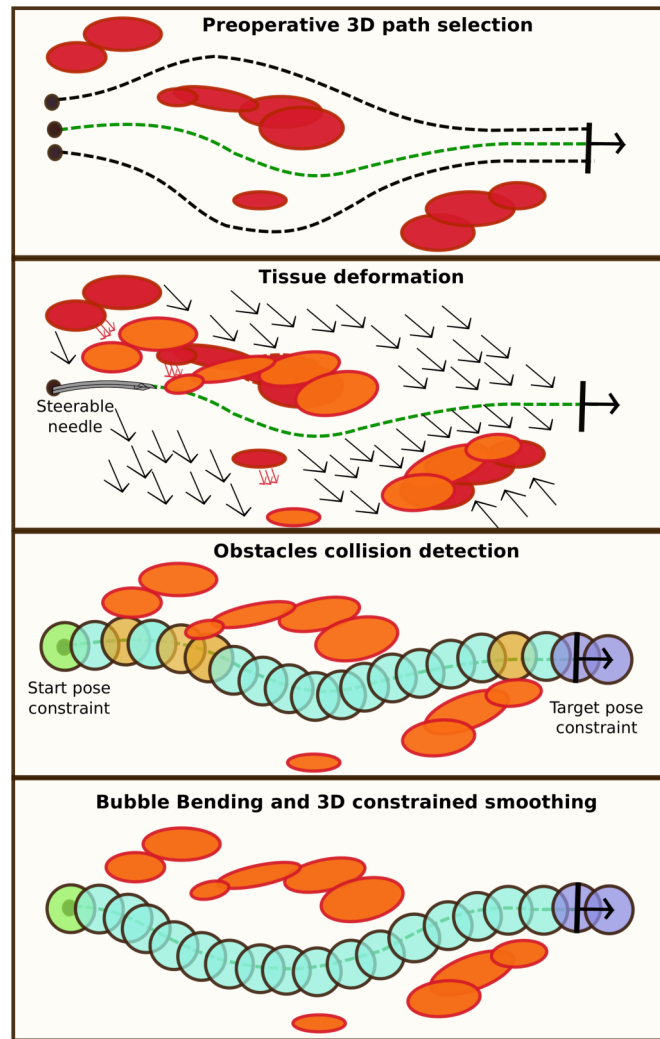
Figure 5.1: Our application of the "Bubble Bending" technique can be summarised as follows (starting from the first frame on the top): (i) a preoperative path is selected by the surgeon, (ii) a virtual channel of overlapping spheres around the preoperative path, starting from the current needle tip position (green sphere), adapts to compensate for obstacles deformations; the orange spheres represent a collision with the surrounding obstacles causing a channel adjustment. On the other hand, the violet spheres are static, thus constraining the target approach vector.

Finally, our algorithm is integrated within the EDEN2020 robotic suite through a "Replanning as Control" framework [PBWA14], which automatically steers the needle during insertion. We first test the algorithm's performance in simulation, using a deforming image volume, and then *in-vitro*, with a programmable bevel tip needle (PBN) [SRB18, WSB18], to capture its behavior under real-world uncertainties. Additionally, we believe our method can be applied to other systems where explicit control on entry and target 3D poses and bounded curvature are required.

5.2 Extended Bubble Bending Approach

Input:

$\quad \mathbf{q}_{p,i}$: preoperative path $\qquad \triangleright$ for $i = 1$ to n

$\quad \mathbf{T}_{tip}$: tip pose

$\quad \mathbf{T}_{tar}$: target pose

$\quad \mathbf{M}_{obs}(\mathbf{x})$: obstacle binary map

$\quad \mathbf{D}(\mathbf{x})$: deformation field

Output:

$\quad \mathbf{q}_{u,i}$: updated path

1: **procedure** Extended Bubble Bending
2: $\quad \mathbf{q}_{u,i} \leftarrow \mathbf{q}_{p,i} \qquad \triangleright$ Updated path **while** $\mathbf{T}_{tar}$ *is NOT reached* **do**
$\quad\quad$ **end**
$\quad\quad$ *Find bubble centres*
3: $\quad \mathbf{q}_{b,j} = \text{BubbleReorganisation}(\mathbf{q}_{u,i}) \qquad \triangleright$ for $j = 1$ to m
4: $\quad (\mathbf{q}_{d,j}, \mathbf{T}_{tar}, \mathbf{M}_{obs}) \leftarrow \text{ApplyDef}(\mathbf{q}_{b,j}, \mathbf{T}_{tar}, \mathbf{M}_{obs}, \mathbf{D}(\mathbf{x})))$
5: $\quad \mathbf{q}_{c,j} \leftarrow \text{BubbleBending}(\mathbf{q}_{d,j}, \mathbf{T}_{tip}, \mathbf{T}_{tar})$
6: $\quad \triangleright$ *Apply smoothing with constraints*
7: $\quad \mathbf{p}_{c,j} \leftarrow \text{ConstrainedSmoothing}(\mathbf{q}_{c,j}, \mathbf{T}_{tip}, \mathbf{T}_{tar}, R_{min})$
8: $\quad \mathbf{q}_{u,i} \leftarrow \text{Interpolate}(\mathbf{p}_{c,j}, n)$ **if** $\mathbf{q}_{u,i}$ *is NOT found* **then**
9:
$\quad\quad$ **end**
$\quad\quad$ *STOP insertion* $\qquad \triangleright$ Safety check
10:
11:
12: **end procedure**
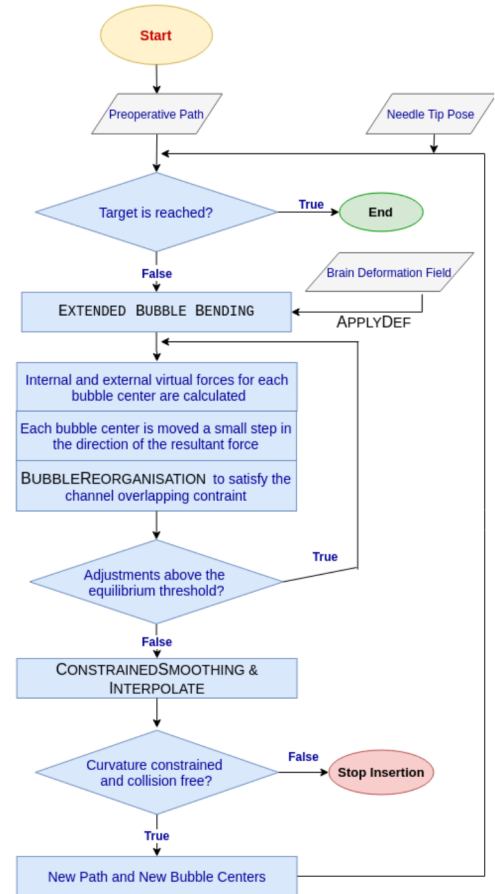
Figure 5.2: The "Extended Bubble Bending" algorithm. Given a preoperative path, $\mathbf{q}_{p,i}$, the algorithm calculates an updated path, $\mathbf{q}_{u,i}$, which accounts for (i) Needle minimum radius of curvature R_{min} (ii) Tissue deformation $\mathbf{D}(\mathbf{x})$ (iii) Clinical obstacles via a binary map $\mathbf{M}_{obs}(\mathbf{x})$ and (iv) Needle and target orientation constraints, within $\mathbf{T}_{tip}$ and $\mathbf{T}_{tar}$ respectively

In this section, we first discuss the details of the proposed replanning algorithm. The algorithm

initialisation is described in Section 5.2.1 and followed by a step-by-step description in Section 5.2.2. Secondly, we propose a metric to evaluate the risk during the insertion (Section 5.2.3). Finally, the experimental setup is discussed in Section 5.2.4. In particular, our replanning method is first evaluated in a computational simulation (Section 5.3.1) to assess its robustness in a deforming environment; then *in-vitro* in Section 5.3.2, to assess the algorithm's integration within an experimental robotic surgery setup.

5.2.1   Initialisation

The following overview of the preoperative phase introduces the concepts relating to surgical constraints and the initialisation of the relevant replanning algorithm parameters.

First, patient-specific diagnostic images are considered to build a binary anatomical obstacle map ($\mathbf{M}_{obs}$) composed of sensitive brain structures such as segmented arteries and brain ventricles. Subsequently, a safety margin is added to obtain an expanded obstacle map taking into account both the needle's footprint and a safety distance to obstacles, which can be set by the clinician. Finally, a preoperative path planner algorithm [PGR19a] is run on the expanded obstacle map to identify a suitable path between a set location, perpendicular to the patient's skull, and a predefined target pose. This becomes the first reference path for our online replanning technique. The initialisation of the standard "Bubble Bending" algorithm requires that the reference path is enveloped within a series of spheres of radius equal to R_b, with a minimum overlapping value, Δ, between consecutive spheres.

In our study, R_b and Δ are chosen to obtain a bubble channel (according to Equation 5.1), the radius of which R_c corresponds to the amount of margin previously introduced with the expanded obstacle map.

$$R_c = \sqrt{(R_b)^2 - (R_b - \frac{\Delta}{2})^2} \tag{5.1}$$

Hence, the channel is initialised to be collision-free with respect to the original obstacle map

$\mathbf{M}_{obs}$.

5.2.2   Extended Bubble Bending Approach

We propose a modified version of the "Bubble Bending" algorithm which makes use of a defor-mation field that can be acquired intraoperatively via an online imaging system (i.e. intraoper-ative ultrasound) [RHM+17] and calculates an obstacle-free path with a flexible constraint on the target pose. In particular accuracy on the target orientation is prioritized with respect to the target position and respective tolerances are provided (Fig. 5.1). The "Bubble Bending" algorithm assumes the path behaves like an elastic band, deforming to accommodate external forces and reacting with internal forces to keep its original shape. The path is discretised as a succession of 3D points, each of which is the centre of a sphere/bubble of a specified radius. Two virtual forces are introduced to describe the bubbles' interaction with the deforming en-vironment. The main virtual forces acting on the path are due to external forces caused by obstacles intersecting the volume of any number of spheres. These generate repulsive forces along the main direction of the obstacle distribution, which keep the path collision-free. Since we consider a binary and discrete obstacle map, each voxel belonging to a certain obstacle contributes with a repulsive force that acts along the line connecting it to the respective bubble centre. The external forces are compensated by internal forces between consecutive bubbles, which act to reduce their displacement and to keep the overlapping region within the predefined minimum value. The internal forces guarantee an elastic response of the bubbles channel to external interactions. (see [LT11] and supplementary material for details about the algorithm). In summary, the position of each sphere is modified according to the total amount of forces act-ing on it until an equilibrium is reached. In this way, the initial path is continuously adjusted in line with the updated obstacles map. However, as the path replanning algorithm presented here is intended for steerable needles in neurosurgery, the method must take into account surgical constraints, such as the required target vector approach and the need for maintaining a safety margin from the brain's sensitive structures. Additionally, it must account for a deforming environment affecting not only the obstacles' position but also the target pose $\mathbf{T}_{tar}$ and the

needle tip pose $\mathbf{T}_{tip}$ which can change due to deformations of the surrounding soft tissue and the high compliance of beveled-tip flexible needles. It should be noted that $\mathbf{T}_{tar}$ and $\mathbf{T}_{tip}$ are 7-dimensional arrays including both the points position information in 3D coordinates ($\mathbf{T}_{tar_c}$, $\mathbf{T}_{tip_c}$) and their orientation, with respect to a reference axis, as 4-dimensional unit quaternions ($\mathbf{T}_{tar_q}, \mathbf{T}_{tip_q}$) .

We address the neurosurgical requirements with an "Extended Bubble Bending" approach that proceeds as follows (Fig. 5.2):

Bubble Reorganisation

The preoperative path is calculated taking into account a safety margin from known anatomical obstacles. A channel of overlapping bubbles $\mathbf{q}_{b,j}$ is generated around the current reference path by BUBBLEREORGANISATION($\mathbf{q}_{u,i}$). New bubbles are inserted when the overlapping value between consecutive bubbles is below the predefined threshold. In the same way, redundant bubbles are removed, as explained in [LT11].

Applied Deformation

The obstacle map $\mathbf{M}_{obs}$ is updated according to the brain displacement field, defined by $\mathbf{D}(\mathbf{x})$ intraoperatively. Unlike the standard "Bubble Bending" method, we opted to contribute to the path adjustment by applying the deformation field directly to the bubble centres' position to allow the channel to adapt to the changing environment. Therefore, target pose $\mathbf{T}_{tar}$ and bubble centres $\mathbf{q}_{b,j}$ are also transformed via APPLYDEF($\mathbf{q}_{b,j}, \mathbf{T}_{tar}, \mathbf{M}_{obs}, \mathbf{D}(\mathbf{x})$). In particular, the Mathworks Matlab2019b$^©$ function *imwarp* is used to transform these points according to the displacement featured at their specific position, resulting in $\mathbf{q}_{d,j}$. The tip pose $\mathbf{T}_{tip}$ is continuously input to the system from the EM sensing.

Bubble Bending

The bubble centres are constantly adjusted following the "Bubble Bending" method
BUBBLEBENDING($\mathbf{q}_{d,j}, \mathbf{T}_{tip}, \mathbf{T}_{tar}$). Virtual internal and external forces are computed for each
bubble center, the position of which is moved by a discrete step in the direction of the respec-
tive resultant force. In our application, this applies to all of the bubbles except the two at the
beginning and the two at the end of the bubble channel, which keep the correct initial and final
orientation respectively. This is an iterative procedure that runs until the total channel adjust-
ment is below an equilibrium threshold and is also entirely collision-free. At every iteration, a
reorganisation of the bubble channel is performed. The result at this stage is an obstacle-free
bubble channel represented by $\mathbf{q}_{c,j}$.

Constrained Smoothing

The bubble center positions act as way-points. They must be smooth and satisfy curvature
continuity and the constraint on the minimum radius of curvature $\mathbf{R}_{min}$
(function CONSTRAINEDSMOOTHING($\mathbf{q}_{c,j}, \mathbf{T}_{tip}, \mathbf{T}_{tar}, R_{min}$). The CES approach has already
been applied in previous studies to smooth the bubble center positions (BCPs) for "Bubble
Bending" algorithm implementations in 2D scenarios. Here, we extend the CES to 3D and with
adjusted constraints on the convex optimisation. Our convex optimisation aims to minimise
two objective functions O_1 and O_2 simultaneously, as defined in Equation 5.2.

$$O_1 = \sum_{k=2}^{n-1} \left\| 2\mathbf{p}_k - \mathbf{p}_{k-1} - \mathbf{p}_{k+1} \right\|^2$$
$$O_2 = \sum_{i=3}^{n-2} \left\| \mathbf{p}_i - \mathbf{q}_i \right\|$$
$$\underset{\mathbf{q}_3 \cdot \mathbf{q}_{n-2}}{\text{minimize}} \; (O_1 + O_2) \tag{5.2}$$

$$s.t. \qquad \mathbf{p}_1 = \mathbf{T}_{tip_c};$$

$$\mathbf{p}_2 = \mathbf{T}_{tip_c} + d\,\mathbf{V}_{in}; \qquad\qquad \mathbf{p}_{n-1} = \mathbf{T}_{tar_c} - d\,\mathbf{V}_{fin} \qquad\qquad (5.3)$$

$$\|2\mathbf{p}_k - \mathbf{p}_{k-1} - \mathbf{p}_{k+1}\| \leq \frac{d^2}{R_{min}} \qquad\qquad (5.4)$$

$$(\mathbf{p}_n - \mathbf{T}_{tar_c})^2 \leq \epsilon^2$$

$$\mathbf{V}_{fin}(\mathbf{p}_n - \mathbf{T}_{tar_c}) = 0 \qquad\qquad (5.5)$$

Here, $\mathbf{q}_i$ represent the BCPs ($\mathbf{q}_{c,j}$) resulting from the BUBBLEBENDING() function (Fig. 5.2); while $\mathbf{p}_i$ represent the set of optimisation variables, initialised as $\mathbf{q}_i$, which will eventually converge to the solution and be the output ($\mathbf{p}_{c,j}$) of the CONSTRAINEDSMOOTHING() function. In particular, the minimisation of O_1 is, in the CES approach, a geometrical method to reduce the curvature "peaks" along the path, thus leading to a much smoother result. O_2 represents the distance from the bubble centers, minimised to keep the smoothed curve within the obstacle-free bubble channel and as close as possible to the reference path. Equation 5.3 sets optimisation constraints on both the current tip orientation ($\mathbf{T}_{tip_q}$) in the form of directional vector $\mathbf{V}_{in}$ and the current target orientation ($\mathbf{T}_{tar_q}$) in the form of directional vector $\mathbf{V}_{fin}$; Equation 5.4 represents a CES approach to enforce the geometrical constraint to bound the minimum curvature radius $\mathbf{R}_{min}$ of the generated path. Finally, in Equation 5.5, the target point $\mathbf{p}_n$ is constrained to be located on a plane that includes the original target point $\mathbf{T}_{tar_c}$ and has the constrained target orientation as the normal. Furthermore, a maximum distance tolerance, ϵ, from $\mathbf{T}_{tar_c}$ is included, which can be tuned according to the required target accuracy. The replanned path is, therefore, a curvature constrained approximation INTERPOLATE($\mathbf{p}_{c,j}, n$) of the new BCPs resulting from the iterative bubble channel deformation. Additionally, the accuracy of the desired target approach angle is prioritized. If these criteria are not satisfied (worst-case scenario) then the algorithm interrupts, indicating that the patient's safety may be at risk. The surgeon can then decide either to progress manually or to move backward until a new path that meets the constraints is found.

5.2.3 Online Risk Metric

A risk metric for curvature constrained steerable needles was developed in this study, which measures how feasible it is for the current PBN tip pose to reach the target pose while meeting the kinematic constraints of the needle. In other words, this metric quantifies the robustness of the current path to further deviations and therefore the risk of an inaccurate outcome.
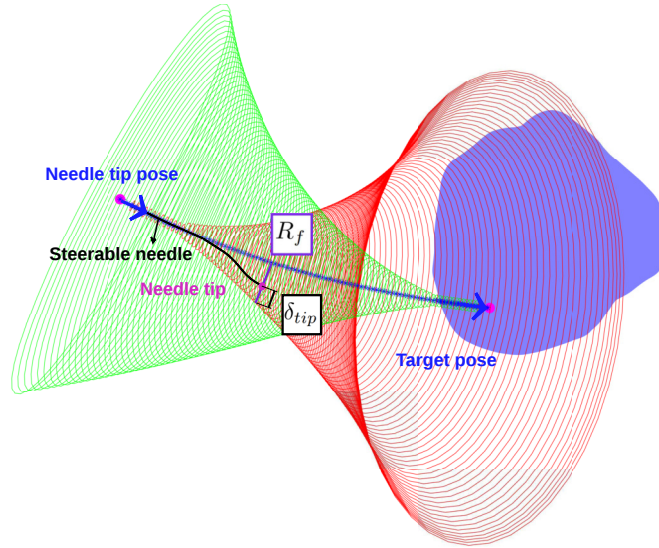
Figure 5.3: This figure shows the feasibility volumes starting respectively from the tip pose and the target pose. The intersection represents that region of feasibility the needle should aim to stay within, during the insertion, to satisfy both curvature and orientation constraints. The distance of the needle tip (δ_{tip}) from the boundaries of the intersection with respect to the feasibility volume radius at that height (R_f), gives us a metric of risk during the insertion.

The needle tip position is evaluated with respect to a feasibility or reachability volume, starting from the current target pose, and directed along with the target orientation in the direction of the path. Conversely, the target point is evaluated with respect to a feasibility volume starting from the current tip location, directed along with the corresponding tip orientation in the direction of the target (Fig. 5.3). These volumes have the shape of a horn torus, the radius of which is equal to the minimum radius of curvature the needle can follow (R_{min}). The inclusion of both points within the corresponding feasibility regions ensures that the target orientation requirement is achievable from the current tip pose.

The risk metric ρ, normalised in the range [0,1], is computed as the ratio between the minimum distance of the tip from the edges of the boundaries of the feasibility regions intersect (δ_{tip}) and

the radius of the feasibility volume (R_f) at the same distance from the target (Equation 5.6).

$$\rho = \frac{\delta_{tip}}{R_f}; R_f \geq \delta_{tip} \qquad (5.6)$$

This metric can be used to provide the surgeon with feedback about the current path related risk.

5.2.4   Path Replanning Simulation

The robustness of our path-planning algorithm to brain-shift deformations was evaluated in a simulated environment.

Preprocessing

Anonymized medical images (MRI/CT) of a healthy subject from a patient dataset acquired within the context of the Horizon 2020 EDEN2020 European project [CF19] were used. We performed segmentation of the skull and key anatomical structures, such as the brain vessels and ventricles, to produce a realistic obstacle map. The AHFT preoperative path planner algorithm [PGR19a] was run on the expanded obstacle map to find paths starting from different entry-point locations perpendicular to the patient's skull directed to a set of target poses. For the subject in this study, a total of 165 paths (Fig. 5.4) were obtained from the AHFT using an expanded obstacle map with a margin equal to 1.68 mm, computed as the sum of the radius of the PBN used in the *in-vitro* experiments (1.25 mm), and a safety margin, arbitrarily set to 30% of the PBN radius (0.43 mm). This distance also guarantees some maneuvering space in case of replanning. The 165 paths were used to simulate the same number of insertions.

As mentioned previously, tissue deformation is an important factor that can influence targeting accuracy. To account for this, a simulated deformation field was generated, taking into account that the mean displacement of the brain surface during neurosurgery is found in the literature to be up to 15 mm. In Reinges et al. [RNK+04] brain-shift measured 6.1±3.4 mm on average
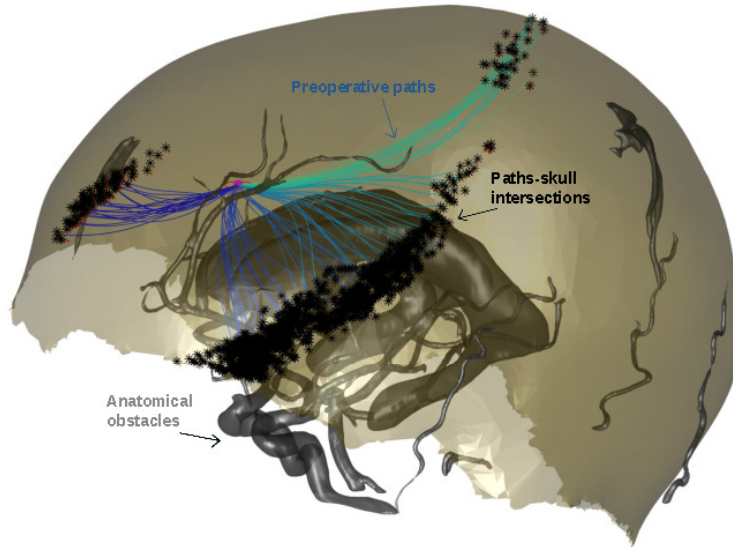
Figure 5.4: The figure shows the generated AHFT [PGR19a] preoperative paths reaching the target with different vector approaches (different shades of blue). These paths intersect the patient skull perpendicularly within a tolerance of five degrees.

after approximately 50 minutes after dura opening, where a comparison between superficial and sub-cortical brain-shift at 20 mm distance over the same time period is also performed. They found that deep brain structures experience a smaller deformation compared to cortical structures, with a decreasing deformation rate of 0.59 mm per millimeter depth. Consequently, we utilised a simulated deformation field of magnitude equal to 15 mm at the dura mater, which progressively decreases at 0.59 mm per millimeter of depth, towards the stem.

Computational Simulation Protocol

A fraction of the deformation field was progressively applied to the obstacle map at each step of the simulated insertion so as to achieve complete deformation at the point the target was reached. This approach was adopted to replicate the average amount of brain-shift experienced by a patient during neurosurgery. During these trials, the main direction of the applied deformation (coinciding with the gravity vector in a real-life scenario) was randomised for each simulation to increase the variability of the test. The 165 preoperative paths were used as sequential inputs to the path replanning algorithm simulations, which were run five times each, for a total of 825 simulated insertions.

Table 5.1: Path Replanning Parameters

R_b	Δ	R_c	R_{min}	tar_{tol}	α_{tol}
3 mm	0.96 mm	1.68 mm	70 mm	2.5 mm	10°

A replan was performed at every insertion step (arbitrarily considered to be 1 mm in length) just after deformation was applied to the entire obstacle map, target pose, tip pose, and the BCP. As in Table 5.1, we set R_b equal to 3 mm in order to react only to obstacles very close to the catheter body (Fig. 5.5). The overlap Δ was chosen as 0.96 mm and the minimum channel radius R_c was, therefore, equal to 1.68 mm (Equation 5.1), matching the value of the obstacle margin included in the preoperative expanded obstacle map. This guarantees that the channel is initialised as obstacle-free. However, this minimum distance from obstacles is constrained by the algorithm during the entire operation. Additionally, target orientation accuracy is prioritised within an arbitrarily defined tolerance of α_{tol}. Finally, a tolerance tar_{tol} of 2.5 mm is used for the target position, which is within the acceptable accuracy for minimally invasive neurosurgical treatment and comparable to the results in [PBWA14]. The simulations were run on a workstation with an NVIDIA GeForce GTX 1080 Ti 11GB Pascal using Matlab2017b (Mathworks inc.) and the CVX package available in Matlab [cvx] for the smoothing convex optimisation.

5.2.5   Path Replanning Experiments

These trials aim to demonstrate the integration of our algorithm within the EDEN2020 robotic suite. In particular, we chose the "Replanning as Control" framework as a tool to create a challenging testing environment for our replanning. Successful implementation of this framework depends upon a low computational replanning time and high robustness in correcting for real-world perturbations while finding feasible and safe paths at each insertion step. In contrast with the standard practice of planning a feasible path and then using a feedback controller for correcting uncertain perturbations, we want our path replanner to be able to correct for real-world inaccuracies (i.e. needle tip deviation, dynamic model inaccuracies, and hardware acquisition uncertainties). On the other hand, the "Replanning as Control" framework removes
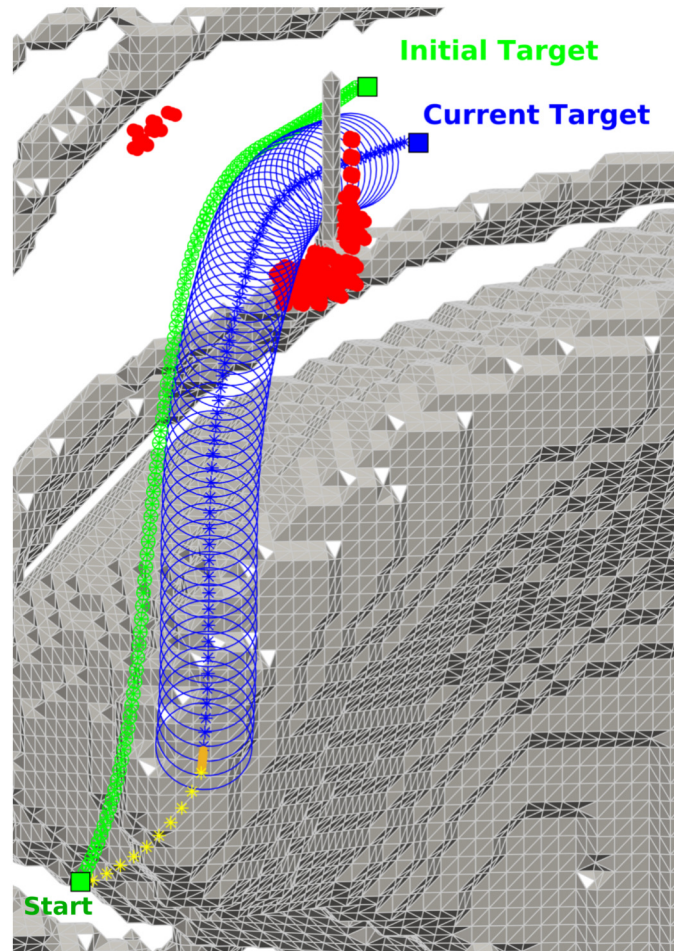
Figure 5.5: The path replanning algorithm generates a new path at every step (yellow dots) along with the insertion. The current path (blue stars) starts from the current Tip_{pose} (orange arrow) and reaches the "Current Target" pose which is deformed with respect to the "Initial Target" due to the simulated brain shift. In this figure, the current path is shown as the centerline of the obstacle-free bubble channel (blue cylinder). The red dots identify obstacles that fall within the bubble channel, thus contributing to the repulsive force that triggers channel deformation.

the need of a user guiding the needle insertion, thus avoiding external influence on the resulting accuracy. The system automatically steers the needle along paths that avoid obstacles of known location.

System Components

We describe the experimental protocol starting from the experimental setup shown in Fig. 5.6.

- Bevel-Tip Steerable Needle: our PBN is a passive catheter with a finite orientation velocity and a bio-inspired insertion mechanism [FKT$^+$10b]. Particularly, the offset measured at the tip between its four segments influences its bending direction.

- Needle Steering Robot: the EDEN2020 robotic suite (www.eden2020.eu) comprises four actuators that activate the four segments of our needle independently to provide the desired motion [MSB$^+$18].

- Electromagnetic Tracking System: four electromagnetic (EM) tracking sensors (Aurora 5DOF catheter, type 1, external diameter 0.3 mm, position accuracy 0.9 mm/0.3; Northern Digital Inc., Canada), inserted one in each of the four needle segments, were employed to estimate the probe tip pose $\mathbf{T_{tip}}$ continuously during the insertion process, thus providing the path-replanner with the start pose constraint for its subsequent path generation.

- Gelatine Box: a 6% by weight bovine gelatin (Chef William Powdered gelatine) was placed into a cuboidal block of approximate 20 cm x 10 cm x 25 cm for our experiments.

- Front-end Visualisation Software: the EDEN2020 visual interface [EM19] provides an intra-operative modality featuring three standard MRI orthogonal views and an interactive simulated perspective of the current path with respect to the needle tip pose.

In-vitro Experiments Protocol

The experiment block diagram in Fig. 5.7 shows how the "Replanning as Control" block receives the current tip pose as input and generates a new path from there. The generated

path is then expressed in the Parallel Transport Frame as in [WSB19a].   The frame assumes

Figure 5.6: Experimental setup [FSRyBDew]: the needle insertion is driven by the actuation system, comprising 4 linear actuators that can independently control each one of the four needle segments. A 6% by weight bovine gelatine sample is used to simulate a soft-tissue insertion. Four EM sensors are placed within our PBN to track the insertion.
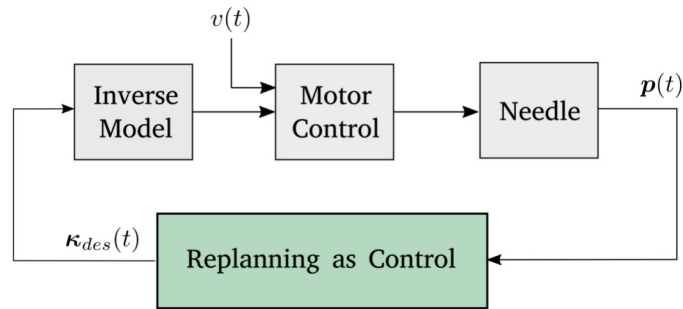
Figure 5.7: Block diagram showing how the 'Replanning as Control' framework fits within the proposed semi-automatic PBN insertion method.

that the tangential vector field $\mathbf{T}(s)$ (with s being the arc-length parameter) is unique, thus providing freedom in choosing any arbitrary basis $[\mathbf{N}_1(s),\mathbf{N}_2(s)]$ as long as the components are perpendicular in the normal and binormal planes. In our replanner, we constrain the first frame $\mathbf{T}(0)$ to match the current tip pose. Then, the curvatures $\mathbf{k}_{des(t)}$ describing the change of the

tangent vector $\mathbf{e}_z$ in the $\mathbf{e}_y$ and e_x directions, as defined in the body-attached frame of Fig. 5.8, are calculated. The PBN inverse model, as explained in [WSB18], takes $\mathbf{k}_{des(t)}$ as input and returns the best relative offset between the four-needle segments to achieve the desired curvature.
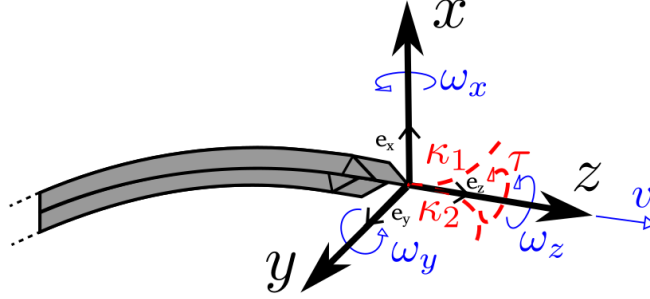
Figure 5.8: The PBN body frame coordinates are shown (top) as described in Watts et al. study [WSB19a]. In particular angular and linear velocities, ω_x, ω_y, ω_z and v are shown along with the corresponding curvatures κ_1, κ_2 and torsion θ (assumed to be zero for our needle).

To test the system *in-vitro*, three preoperative plans are generated using our surgical planning software. A total of fifteen needle insertions (five insertions for each path) are performed in gelatin with virtual anatomical obstacles. The virtual environment used is in this case static, as any simulated deformations would not be reflected in the EM sensor positions, as would be expected in the real scenario.

In fact, in a real world scenario, we would expect the needle tip to deviate according to the passive displacement of our flexible catheter within a deforming tissue. However, the aim of these trial was to demonstrate that our path replanner is fast enough to be used in a "Replanning as Control" framework while correcting for perturbations caused by real world uncertainties. This enables the system to automatically steer the needle along paths that avoid obstacles of known location. In these trials, the needle is actuated by motors at an insertion speed of 0.4 mm/sec, while the replanner is constantly generating new paths. Clinical parameters such as the proposed risk metric and the distance from the target are provided to surgeons during the procedure. To evaluate our algorithm's performance we acquired the following key data during both simulated and *in-vitro* insertions (Table 5.2 and 5.3).

- Replanning time ($T[sec]$)

It measures the computational time associated with the proposed replanner. It has to fulfill the minimum requirement of an update per millimeter of insertion for a constant maximum of 0.4 mm/sec needle insertion speed.

- Success rate ($S[\%]$)

  It measures the algorithm's robustness in reaching the target within the constraints (tar_{tol}) while maintaining the minimum distance from obstacles (R_c).

- Target accuracy ($C_{Loop}[mm]$ error)

  Target orientation accuracy is considered along with target position accuracy. They both have to be within the given tolerances: tar_{tol} and α_{tol} respectively.

- Path similarity ($Fr[mm]$)

  Proximity to the previously calculated path is constantly maximised during the insertion. The Frechet distance provides an appropriate "path similarity" evaluation criteria. the Fréchet distance is a measure of similarity between curves that takes into account the location and ordering of the points along the curves. Given two curves P and Q, "Fr" is defined as the minimum cord-length sufficient to join a point traveling forward along with P and one traveling forward along with Q.

5.3   Results and Discussion

5.3.1   Computational Simulations Evaluation

We aim to demonstrate that our technique can accurately guide the needle to the a desired target not only in terms of position but also in terms of final heading while avoiding complex 3D deforming obstacles. In doing so, we tested our solution in a constantly changing simulated environment and measure its robustness in reaching the target within the constraints (Success rate ($S[\%]$)).

From a total of 825 tests, 93.6% were successful. The remaining 6.3% resulted in unfeasible

scenarios where an obstacle-free solution that meets both kinematic and surgical constraints was not able to be found. At the point during the insertion this occurred, the simulation stopped.

Table 5.2: Extended Bubble Bending: computational simulation results

O_{Loop}	C_{Loop}	$T[sec]$	$S[\%]$	$Fr[mm]$
$8.10\pm0.31mm$	$0.65\pm0.46mm$	0.53 ± 0.03	93.6	0.24 ± 0.06
$18.81\pm24.5°$	$3.25\pm5.23°$			

Table 5.3: Extended Bubble Bending: experimental results

C_{Loop}	$T[sec]$	$S[\%]$	$Fr[mm]$
$1.81\pm0.51mm$	0.51 ± 0.02	100	0.48 ± 0.11
$5.9 \pm 1.42°$			

The average computation time was 0.53 ± 0.03 seconds, which fulfills the minimum requirements. Finally, the final distance from the target pose C_{Loop} is compared to the error we would have in an open-loop situation O_{Loop} when there is no replanning involved (our ground-truth). This comparison is conducted in simulation (Table 5.2). With an independent two-sample t-test, we measured a statistically significant mean reduction in targeting error over the open-loop results (P<.0001), with O_{Loop} mean equal to 8.10 ± 0.31 mm compared with 0.65 ± 0.46 mm in the case (C_{Loop}) case. These results meet the given tolerance of 2.5 mm target position error we set for this task. Furthermore, the target orientation error was computed, with a closed-loop mean of 3.24 ± 5.23 degrees, versus 18.81 ± 24.5 degrees in the open-loop case. The total improvement in target orientation accuracy is also statistically significant (P<.0001). Finally, the average Fr, calculated at each step of insertion is equal to 0.24 ± 0.06 mm. Since the simulated deformation will inevitably cause a difference between the current and the updated path, we can only aim to minimize Fr value.

5.3.2   In-vitro Experiments Evaluation

An average target position error of 1.81 ± 0.51 mm and a mean target orientation error of 5.9 ± 1.42 degrees were measured at the end of 15 insertions (Fig. 5.9). The average computational replanning time of 0.51 ± 0.02 seconds confirms our algorithm's performances *in-vitro*.

Then, a Frechet distance of 0.48±0.12 mm is measured. These values are substantially higher than the respective simulation errors. We believe this discrepancy arises primarily from the inaccuracies in our needle dynamic model. However, all the tests were considered successful, since our technique constantly guided our PBN to the desired target pose within the given tolerances and above the previously set minimum R_c.
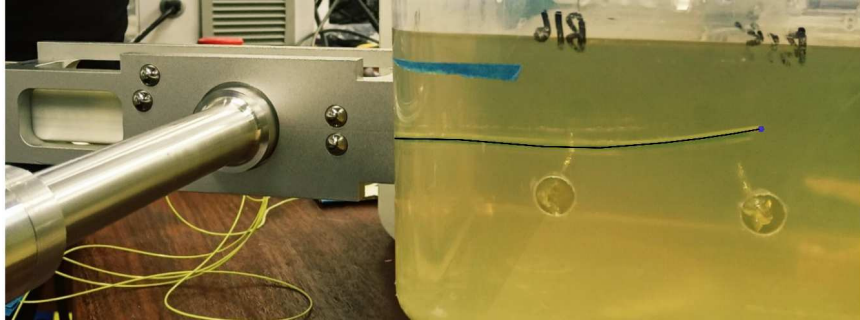
Figure 5.9: Our flexible needle at the end of the insertion is shown.

5.4   Conclusion

This study describes a novel 3D path replanning technique optimised for soft-tissue surgical interventions and applicable to curvature bounded steerable needles. The algorithm can smoothly adjust a preoperative path intraoperatively, while meeting constraints on both target position and orientation. Furthermore, this system reacts smoothly to ongoing tissue deformations and real-world uncertainties. Its ability to compensate for local changes, while meeting the constraints on its global goals, removes the risk of long path detours affecting the more common RRT-based techniques. A complete implementation of the method was tested in both simulation and *in-vitro* experiments demonstrating acceptable target position accuracy for minimally invasive neurosurgery [PBWA14]. These results confirm its performance as an online replanning tool and building block in a "Replanning as Control" needle steering framework, with the novel addition of a target orientation constraint.

Chapter 6

An Enhanced Delivery Ecosystem for Neurosurgery

In this chapter, the EDEN2020 robotic platform for steerable needle neurosurgery is briefly presented. The system has been developed by the whole EDEN2020 team at Imperial and a general description of the platform and the surgical workflow is an edited version of research currently under review:

Riccardo Secoli, Tom Watts, Marlene Pinzi, Stefano Galvan, Eloise Matheson, Abdul Donder and Ferdinando Rodriguez Y Baena, "A Modular Robotic Platform for Precision Neurosurgery with a Programmable Bevel-Tip Needle" The International Journal of Robotics Research (IJRR), under final review.

On the other hand, the experimental work presented in this chapter, which aims to evaluate the path planning integration, is a contribution of this thesis. Section 6.2 and Section 6.3 are not part of previous publication but have been included in this thesis to extend the path planning integration assessment to a real-world scenario.

6.1   EDEN2020 clinical motivation

A new class of steerable needles, composed of a highly flexible material, can allow the surgeon to steer avoiding sensitive structures, thus reducing patient trauma. The EDEN2020 technology features a novel flexible needle consisting of four axially interlocked parts, independently actuated, that can slide relative to one another. By defining appropriate axial offsets between needle segments, steering in two dimensions [SR13b] and three dimensions [SR13a] has been demonstrated. This structure also allows biologically inspired motion profiles to be investigated, where each segment is moved reciprocally rather than simultaneously. The reciprocal motion has been shown to be advantageous due to the tensile support offered by segments being retracted to those being inserted; a phenomenon used, for example, in drills designed for interplanetary exploration [PG15]. A reciprocal motion actuation strategy, where each segment is moved forward in turn cyclically, can be performed with this configuration to reduce tissue deformation during the insertion process [20114].
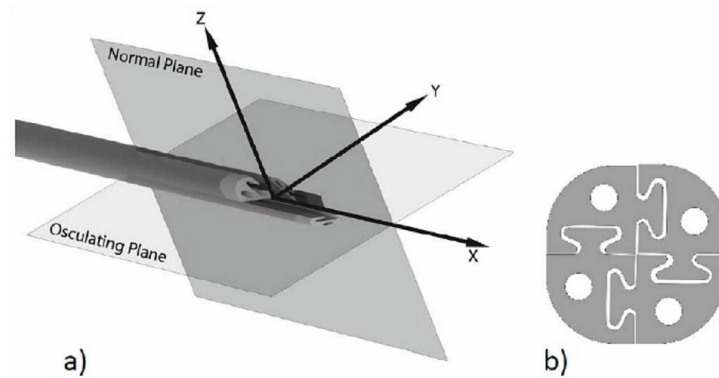
Figure 6.1: EDEN2020 bio-inspired needle (a): it consists of four interlocking segments (b) where each segment is moved reciprocally rather than simultaneously

Existing robotic neurosurgical platforms can undertake a variety of procedures, including instrument delivery, resection, and electrode implantation. However, there is currently no existing pre-commercial solution for the delivery and control of steerable catheters, in particular, programmable bevel-tip needles [SR16]. The EDEN2020 system presents the first modular robotic system Fig 6.2 that can perform neurosurgical procedures using a programmable bevel-tip needle in a sterile setting.

The EDEN2020 surgical system supports a procedure akin to stereotactic surgery. This is a type of minimally invasive surgery characterised by the use of 3D spatial coordinate systems to facilitate precise positioning of equipment. The EDEN2020 consortium works in partnership with Renishaw (Renishaw plc, UK) and uses three of their products in the surgical process: a modified version of the Neuroinspire software, the Neuromate robot and a stereotactic frame. The Neuroinspire software allows surgical planning and brain scan visualisation. The end effector of the Neuromate robot is used to precisely position surgical equipment, and the stereotactic frame attaches to the base of the Neuromate robot.

This chapter focuses on the integration within the NeuroInspire of both proposed pre-operative (Chapter 4 3) and intra-operative planning softwares (Chapter 5).

The EDEN2020 full system integration made possible to accomplish different studies, especially to test our intra-operative planning solution. First, multiple users simulated insertions (Section 6.2) have been performed to validate the EDEN2020 front-end interface and in particular the influence of path re-planning integration on users performance. Then, *in-vitro* trials (Section 6.3) have been performed to assess the advantages of a trigger-base path re-planning modality with respect to the automatic "re-planning as control" technique outlined in Chapter 5. A surgical workflow for both pre- and intra-operative an assessment *ex-vivo* of the full system on an animal model is also illustrated.
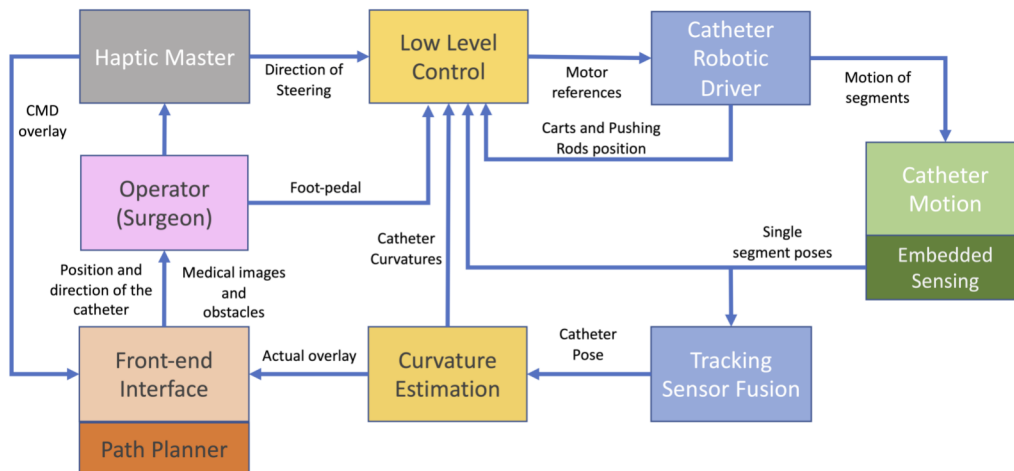
Figure 6.2: Human-in-the-loop architecture of the robotic module ecosystem

EDEN2020 PBN and Catheter Segment Mapping
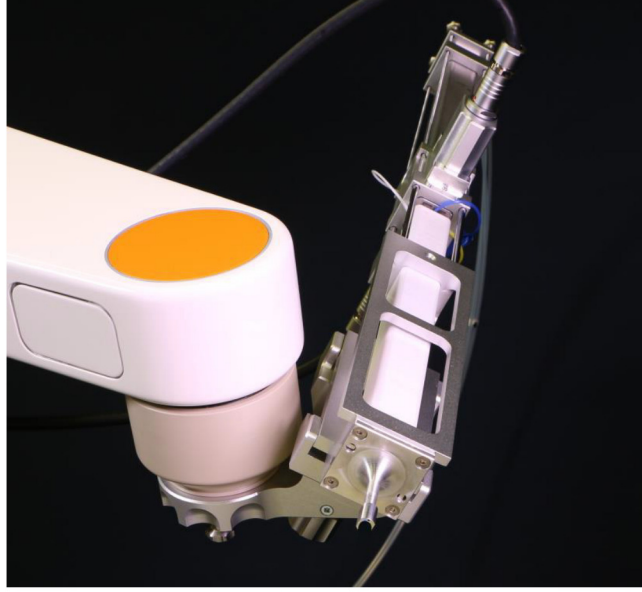
Figure 6.3: End-effector for programmable bevel-tip needle mounted on the neuromate® arm

The EDEN2020 PBN is designed for the specific application of Convection Enhanced Delivery (CED) of chemotherapy drugs directly into brain. It is designed with two lumens per segment (8 lumens in total), one reserved for embedded sensing (e.g. shape sensing or electromagnetic position tracking sensors) and the other to insert an infusion catheter, as show in Figure 6.4. The PBN is made of nanocoated, medical grade, implantable PVC, with each catheter segment colour coded to facilitate interaction with the clinician, as the intra-operative software guides their actions during the infusion process (e.g. screen message: "Insert infusion tube into the BLUE catheter segment").

The mapping between the direction of steering imposed by the user and the direction of the catheter has been extensively reported in [WSyB18] and here briefly summarised for clarity: The relationship between the steering input (catheter configuration) and the resultant curvature vector may be described by a non-linear function $\mathbf{f}$:

$$\kappa = \begin{bmatrix} \kappa_1 \\ \kappa_2 \end{bmatrix} = \mathbf{f}(\Theta) \tag{6.1}$$

where the curvature vector κ contains the two components of steering corresponding to the
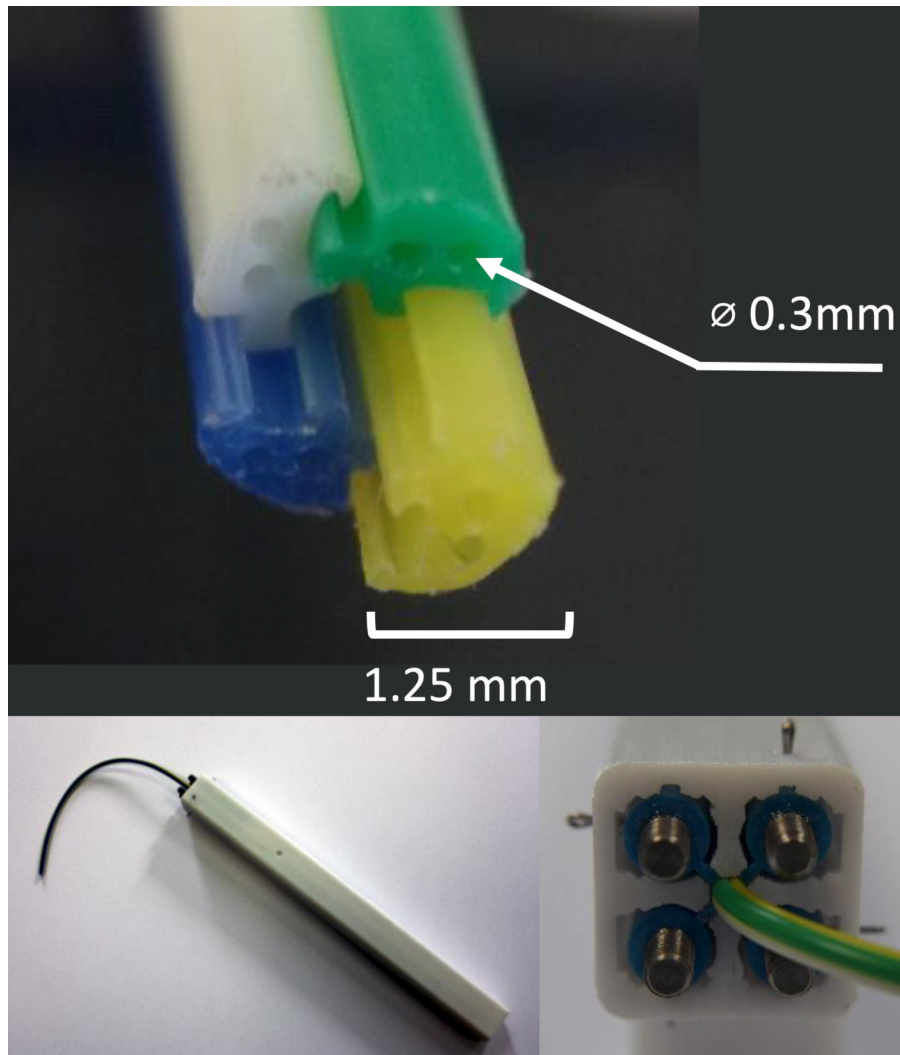
Figure 6.4: Top: Cross-section of the 4-segment PBN with two 0.3mm diameter working channels per segment. The overall PBN diameter is 2.5mm. Bottom-Left: trocar with embedded medical grade PBN. Bottom-Right: connection mechanism between the PBN wings and the push-rods of TB

two orthogonal axes of the joystick. To steer with a commanded direction and magnitude, a corresponding steering input Θ is found. As there may exist more than one catheter configuration to achieve a commanded steering, we formulate the problem as a non-linear programming problem. By optimising a measure of catheter steerability, whilst constraining the commanded curvature with (6.1), the optimal required steering input is found. In the case that a curvature above the maximum achievable is commanded, the optimisation fails to find a solution and the previous steering input is used.

6.1.1 Front-end interface:

The front-end interface was designed on top of the commercial neurosurgical planning and intra-operative software neuroinspire™ (Renishaw plc, UK). The standard functionalities of the software such as the pre-operative registration of MRI and CT images, displays of medical image dataset using conventional three orthogonal views, and renders of the three dimensional volume on a fourth view were kept as the original software.

The new visual interface incorporates the rendering of tractography computed from Diffusion Tensor Imaging (DTI), obstacles segmentation definition or import (e.g. vessels from angiography and other structural area) both for pre- and intra-operative planning. Custom views to support planning (drug selection, target selection, planner options, burr-hole port placement, path selection and visualisation, etc.), devices initialisation and intra-operative navigation were added. In particular, the new visual interface includes the pre- and intra-operative planning method decribed in Chapter 4, Chapter 3 and in Chapter 5.

Pre-operative plan:

The workflow of the pre-operative planner is as follows:

- An MRI scan of the patient's head is performed.

- The stereotactic frame is fitted onto the patient's skull.

- A CT scan is performed. Note that the positions of the IR markers are visible on the CT scan as this is needed for the patient registration step.

- The user follows imaging registration steps in the software

- The Neuroinspire software allows a user to select the position of the IR markers on the CT scan so that the coordinates of the IR markers with respect to the CT reference frame are known.

- The stereotactic frame is fixed to the base of the Neuromate robot. The coordinates of the IR markers with respect to the reference frame of the Neuromate are hardcoded into the Neuroinspire software.

- The coordinates of the markers are known in both the CT and the Neuromate reference frames. Therefore, the transformation between these reference frames can be calculated. This is used in later steps to allow the Neuromate to position surgical tools relative to the patient's head accurately.

- The MRI scan is segmented to isolate any areas in the brain, which may be especially sensitive to surgery. These sensitive areas will be referred to as obstacles and usually consist of ventricles and blood vessels.

- The CT scan is segmented to isolate the skull of the patient.

- The tumour is found and segmented from the MRI scan and the user chooses the infusion drug type and volume

- The back-end software computes and display the infusion catheter target point and direction, and the drug flow rate according to Zhan et al. [ZDB19]

- The skull, obstacles and target pose can be either displayed as a overlay of the three standard surgical planar views or as a 3D rendering view.

- The back-end software computes a set of candidate entry points, that are perpendicular to the skull's surface with a 15% degrees tolerance. The user select the preferred one. There are options to freely modify or manually redefine the entry point if required. A model of the burr-hole port is displayed to facilitate the positioning according to the user's preferences

- The back-end software computes and ranks all feasible paths according to a specific metric. The front-end display the best 10 candidate paths

- The user selects a preferred path among the proposed candidate paths

The software was developed with the extension of adding intra-operative ultrasound (US) imaging guidance, but for the purpose of this assessment, it has not been used. During the pre-operative planning, further steps are dedicated to the optimal position of the US probe. The workflow for the intra-operative part and intra-operative planner are summarised in the following section, while here we describe the intra-operative view for the navigation, rendered on the 4th view of the front-end interface. This fourth view
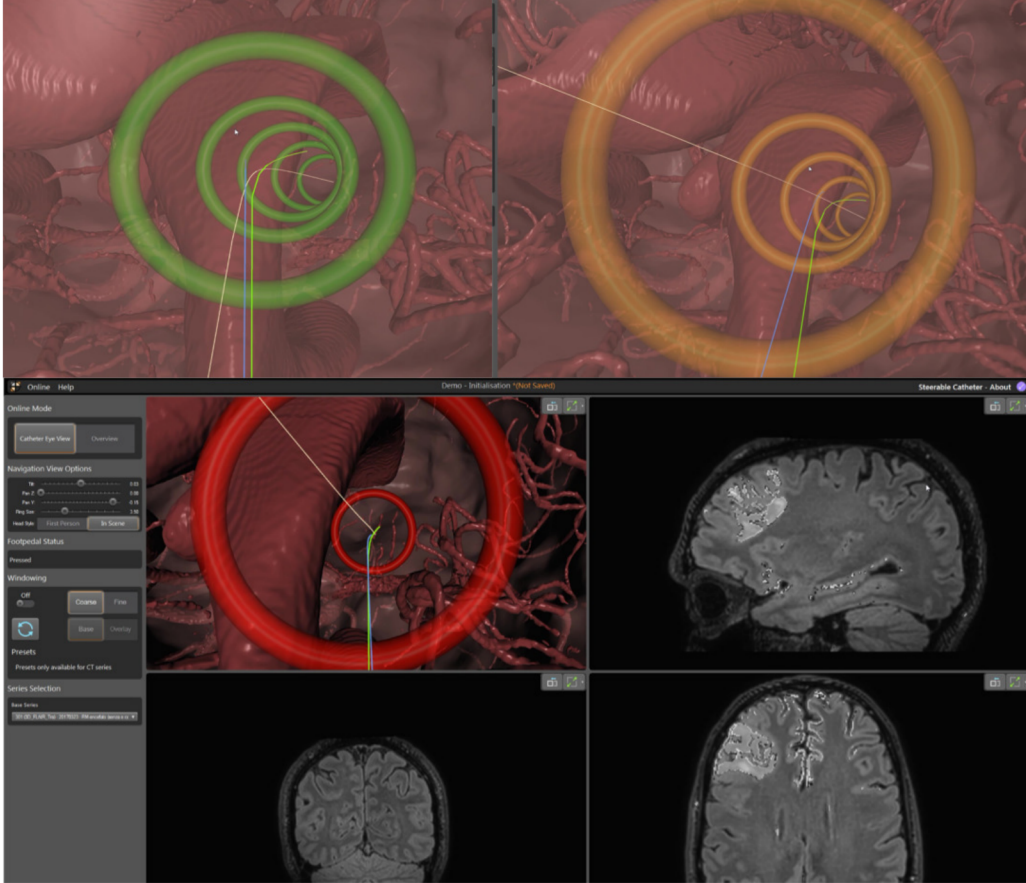
Figure 6.5: Catheter view mode when error is low (top left), getting higher (top right) and high, hence triggers path re-planning (bottom)

renders the anatomical features of the brain as well as the catheter and cues for intuitive steering. Specifically, the pre-operative MRI images are segmented in order to create 3D obstacles maps. With the additional use of the US intra-operative imaging, these 3D obstacles are deformed in real-time according to measurements of the US [GNH18]. The surgeon can then steer through this map in order to reach the desired target, shown in Figure 6.6.

A path planner generates the path the surgeon should follow as in [PGR19a] described in Chapter 4 and integrated in the NeuroInspire, which avoids all obstacles within a safe radius. If the surgeon deviates from the path by a predefined magnitude, then the system will re-plan a new path, (Chapter 5) to the target if one exists. If no such path exists, then the last generated path is displayed to the surgeon, see Figure 6.5. The path that the surgeon should follow, as well as the current configuration of the tip of the catheter, can be visually depicted to the surgeon in multiple ways. In this design, the navigation window shows a 2D render of a 3D environment, where the surgeon has a first person viewpoint when navigating the catheter (called 'Catheter View Mode', see Fig 6.6), though they can also choose to stop steering and look from a third person view (called 'Overview Mode', see Fig 6.7) in order to see the wider environment.
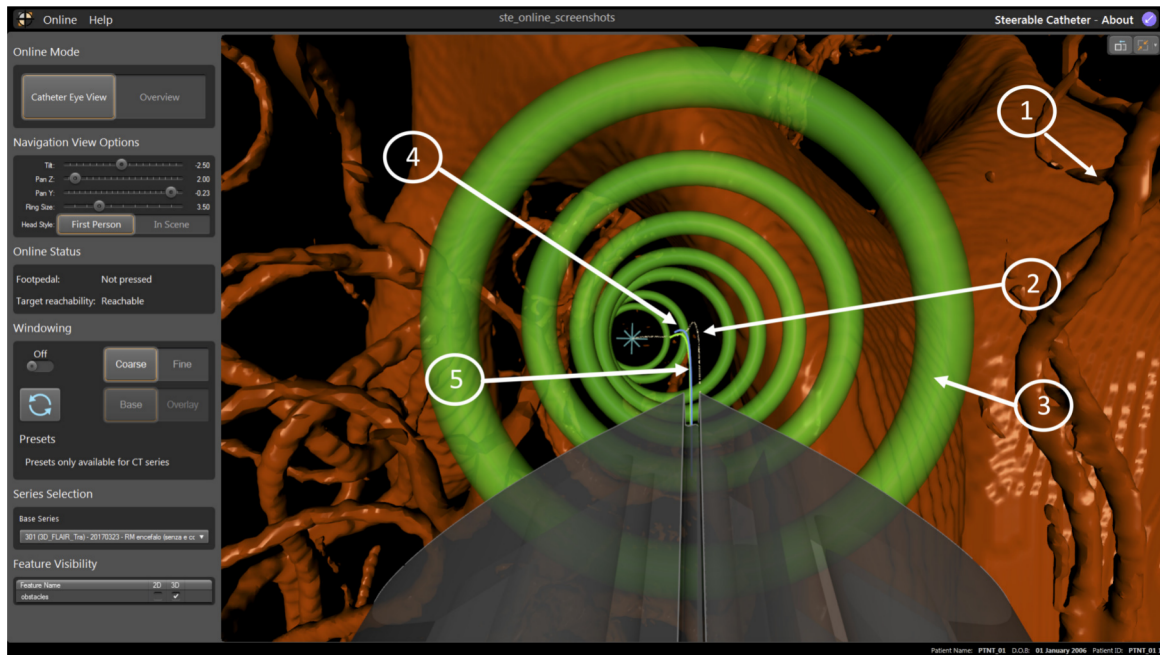
Figure 6.6: Visual interface with Catheter View Mode

This design was chosen based on feedback from an advisory group of neurosurgeons, as it was hypothesized that it would be more intuitive for a surgeon to navigate in first person view, though the third person overview was also desired in order to show a similar viewpoint as normally seen when looking at standard MRI volumes. For the same reason, the selected image (MR, CT) is cut along the three orthogonal planes and displayed in the other three windows. The cutting point is defined by the current position of the catheter tip, as detected
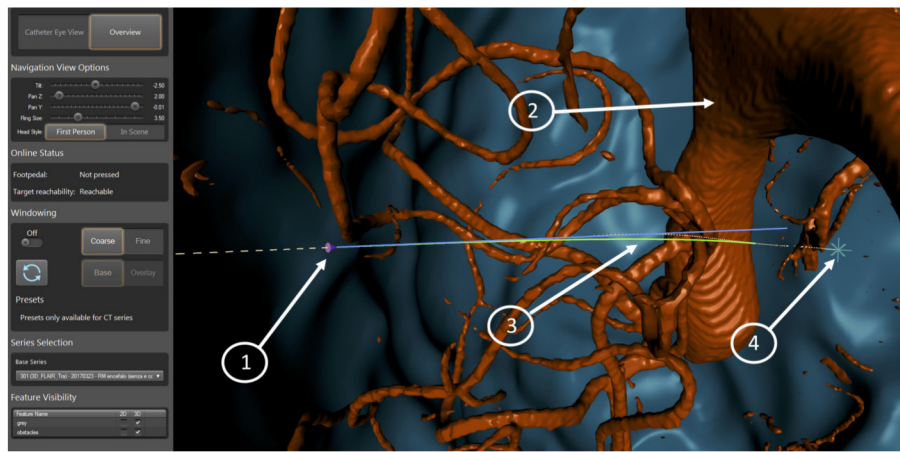
Figure 6.7: Visual interface with Overview Mode

by the sensing. The catheter tip and the outline of the segmented obstacles and target area are overlayed on the slices to give additional feedback to the surgeon. Each of the four individual windows can be maximized as needed. The navigation window in Catheter View Mode (Fig 6.6) has the following visual components:

- Selected segmentations representing the obstacle (e.g. anatomical arterial tree, ventricles, no-go areas)

- Optimal path depicted as a white line

- Waypoints represented as rings, where the centre of the ring lies on the optimal path. The colour of the rings representing the error of the catheter tip pose to the path

- Blue ray representing the 'Actual Overlay'

- Green ray representing the 'Commanded Overlay'

The navigation window in Overview Mode (Fig 6.7) has the following visual components:

- Current pose of the catheter tip shown as a purple cone

- Selected segmentations representing obstacles

- Optimal path (dashed white line) and overlay rays

- Target position represented as a star

The 'Actual Overlay' represents the current path the catheter is following based on a local reconstruction of the curvatures in Parallel Transport frame. This is further described in the next section. The 'Commanded Overlay' represents the path the catheter should follow based on the configuration of the joystick and inverse kinematic described . The colour of the ring represents a metric for the error indicating how far the catheter is from the path, and fuses the magnitude of position and orientation error into a value between 0 (directly on the path) and 1 (far from the path, in which case a path re-planning event is triggered)(Chapter 5, Section 5.2.3). Quantitative and qualitative results from a user studies trial for the visual interface are reported in a previous work of [EM19].

6.2   Multiple users simulated insertions

To validate the EDEN2020 front-end interface and in particular the influence of path re-planning integration on users performance, a set of computational simulation trials were carried out. First, three pre-operative paths were defined using the pre-operative path planner presented in Chapter 4 [PWS$^+$ew] on an anonymised patient dataset [CF19]; then five non-expert users performed six simulated insertions on the three different paths for a total of 18 insertions. All the insertions were executed with visual feedback, but only half of the insertions were integrated with the EDEN2020 intra-operative re-planning method [PWS$^+$ew] and the corresponding on-line visualisation of the adjusted path. Steering was controlled with the joystick and insertion speed was set at a constant 1 mm/s, with start/stop controlled by a foot pedal.

In these trials, the user should follow the displayed path which is adjusted only if the deviation of the tip pose from the path exceeds a predefined magnitude. This magnitude is calculated by mean of a risk metric in the range [0,1] (Chapter 5, Section 5.2.3) which triggers the re-planning when greater than 0.5. The subjects were asked to reach the target with the best accuracy possible; it was not stated whether they should prioritise position or rotational accuracy. What follows is a summary of the instructions given to the users:

- You will be able to train with five insertions for each of the following conditions: path

re-planning on, path re-planning off.

- You will be asked to do three insertions of each of the above conditions over three different paths. The insertion modality will occur at random.

- The foot pedal enables movement

- The 3D navigation window can be maximised or minimised at will

- You can change to overview mode, but you must release the foot pedal

- Follow the position of the path, to reach the position of the target

- Arrive at the target with the same orientation as the target –this is best seen in the overview mode

- Reach the target in the shortest time possible

Two error metrics were calculated for each insertion: (i) The target reaching error, including position and rotation. The position error is measured as the minimum distance between the resultant needle path and the original target location. The rotation error is the angular difference between needle tangent vector and target vector at the closest point. This metric is chosen to disregard an additional error due to target overshoot, which future developments to the visual interface hope to minimise. (ii) The path tracking error, measured as the mean position error along the whole length of the needle path with respect to the original pre-operative path. The standard deviation is also calculated. The overall target reaching error along all the trials and users result equal to $0,59 \pm 0,52$ mm (median value) in position and $7,29 \pm 5,7$ deg in rotation in case of "re-planning on" modality while it reaches $0,67 \pm 0,75$ mm (median value) in position and $8 \pm 6,1$ deg in rotation in case of no re-planning. As evident in the means, the re-planning modality resulted in 11.9% improved target reaching position and 8.87% in rotation compared to no re-planning modality. An analysis of variance showed the difference in target position is statistically significant with p <0.05 (F = 2.109, p = 0.0179). The results in Figure 6.8 suggest that users seem to prioritise position over rotation accuracy, although re-planning modality provides more coherent results. They also show that, in case of re-planning (Figure 6.8 and

6.9), the error in target and pose rotation and their interquartile ranges are generally reduced across users except for User 4 which does not seem to benefit from re-planning modality.
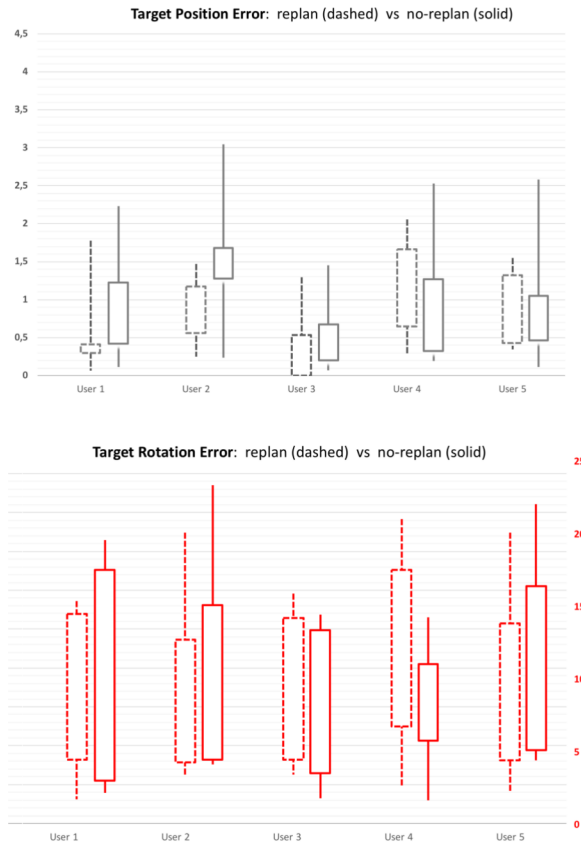
Figure 6.8: Target position (up, in mm) and rotation error (bottom, in degree), in case of no path re-planning (solid line) and with path re-planning (dashed line). The users boxplots include their performances as overall error considering all the insertion of that user in that modality.

The re-planning modality provides better results across paths in terms of target and path tracking accuracy, which are visually highlighted in the next figures (Figure 6.10 and 6.11). Both target and path tracking accuracy and its variance seem to benefit from the re-planning integration, with a significant improvement in case of path 2 target position error ($p < 0.05$, $p = 0.0088$). It is also clear that different paths are associated to statistically different performances due to their different complexity and that good path tracking performances reflect on good target accuracy results.

It can be concluded that path re-planning integration within the front-end is generally advantageous for non expert users, aiding them in reaching the target pose in a more robust and
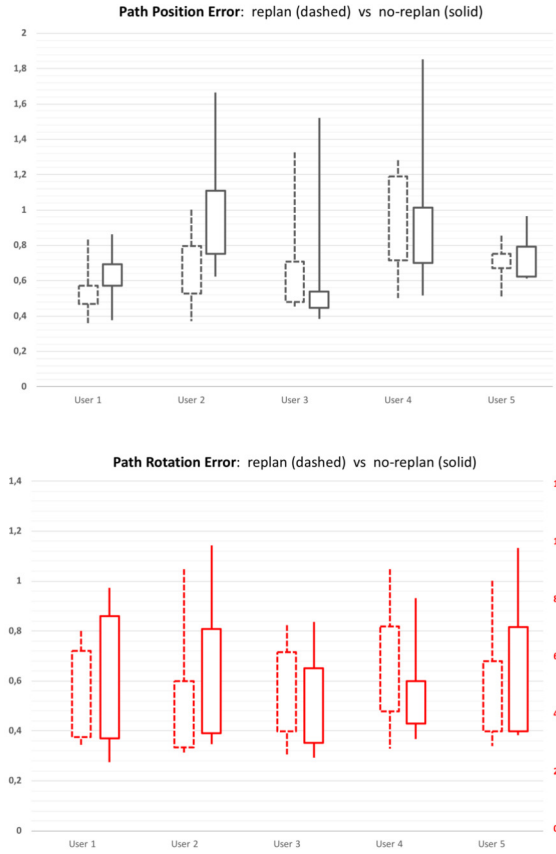
Figure 6.9: Path tracking position (up, in mm) and rotation error (bottom, in degree), in case of no path re-planning (solid line) and with path re-planning (dashed line). The users boxplots include their performances as overall error considering all the insertion of that user in that modality.

accurate way. Adjusting the current path with a new path that compensates for deviations and keeps proximity with the reference one, guides the user towards a specific target pose. It is expected that future trials with a better description of the task, as well as system indications on the desired position and orientation/rotation, would result in lower rotational errors. Also, different risk metric re-planning triggering thresholds could be assessed in future studies to evaluate the influence of different levels of guidance.

6.3   Full system *in vitro* validation

To validate the system, a set of *in vitro* trials were performed in 6% by weight bovine gelatin (Chef William Powdered Gelatine) with a setup as in [AF20]. The reference paths were defined
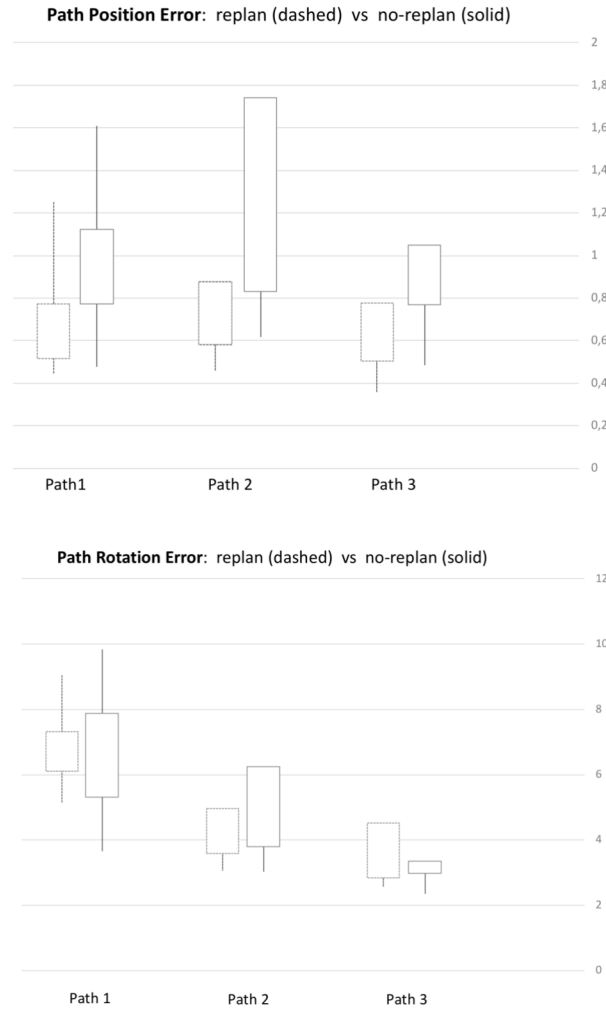
Figure 6.10: Path tracking position (up) and rotation error (bottom) in case of "re-planning" (dashed line) and "no re-planning" (solid line) modalities. The path related boxplots include the performances as overall error across all the users.

using the pre-operative path planner presented in Chapter 5 [PWS$^+$ew] on an anonymised patient dataset [CF19]. An expert user performed five trials on three different paths, for a total of fifteen insertions with an average insertion length of $110mm$. To assess the usability and performance of the system, all insertions were executed with visual feedback. An investigation of the performance of fully automated steering is presented in [PWS$^+$ew], where the proposed path re-planner was used to generate steering inputs and replace the user. In this context, the threshold of activation of the path-planner was set at 2 mm error from the reference path.

The achieved position error is calculated as the average euclidean distance between the tip of the catheter and the target, with overall resulting values of: [0.9439 1.324 1.337] mm respectively
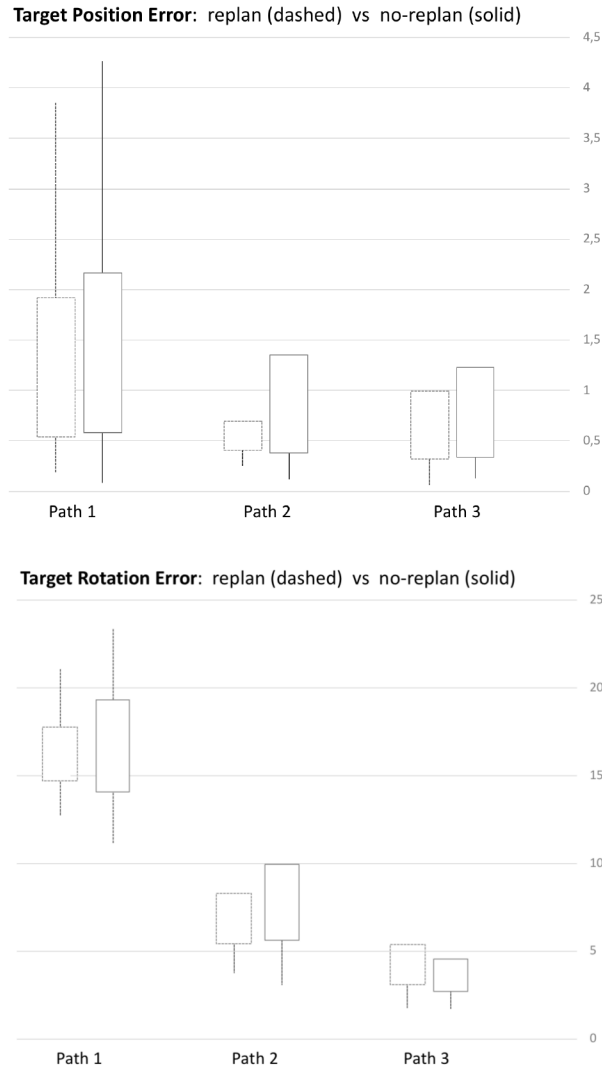
Figure 6.11: Target reaching position (up) and rotation error (bottom) in case of re-planning (dashed line) and no re-planning (solid line) modality. The path related boxplots include the performances as overall error across all the users.

for the 25th, 50th and 75th percentiles.

On the other hand, target rotation error is calculated as the angular difference between needle tangent vector and target vector at the closest point. Its overall value results equal to [4.545 8.337 11.35] deg respectively for the 25th, 50th and 75th percentiles.

We decided to compare user in-vitro performances, aided by the trigger-base path re-planning modality with respect to the automatic "re-planning as control" results outlined in Chapter 5. In that case, the same three path geometries were considered but the insertion was automatic, with the user responsible only for pressing the pedal to start and stop the operation. The overall

target position accuracy value for the automatic re-planning modality is [0.9554 1.213 1.410] mm respectively for the 25th, 50th and 75th percentiles with a target rotation error that reduces to [1.959 6.338 10.93] deg with respect to the trigger-based re-plan scenario.

Looking at Figure 6.12 it is possible to conclude that the interquartile ranges of target position errors are less spread in the case of automatic re-planning but there is no statistically significant difference between the two modalities' performance. On the other hand, the analysis of the updated target error, which corresponds to the last point of the last updated path, results in statistically significant better performances for the automatic fast re-planning modality (t-test, $p < 0.05$, $p = 0.01$).

This can be explained by the fact that the automatic re-planner guides the needle along the current path which is constantly updated during the insertion. Its real aim is, therefore, reaching the final pose associated to the last path update, which is constrained to be at a maximum 2.5 mm from the original target, featuring the same approach angle. On the other hand, the user, by means of a joystick, has no real constraint and could either aim for the original target (still visible on the front-end) or stick to the updated path until the end of insertion as the automatic modality.

With regard to target rotation accuracy, which is independent from the target considered, a two-ways Anova t-test shows there is a statistically significant difference on target rotation error means between the two tested modalities ($p < 0.0001$)(Figure 6.13), with better accuracy results for the automatic re-planning.

It can be concluded that expert user joystick guidance (trigger-based re-planning) and automatic fast-re-planning modalities are both associated to low target position errors although the automatic insertion modality results in a significantly higher target rotation accuracy. Automatic fast re-planning modality should be taken into account as a high potential alternative to trigger-based replanning, especially in case of very complex navigation tasks or when high target orientation accuracy is desired.
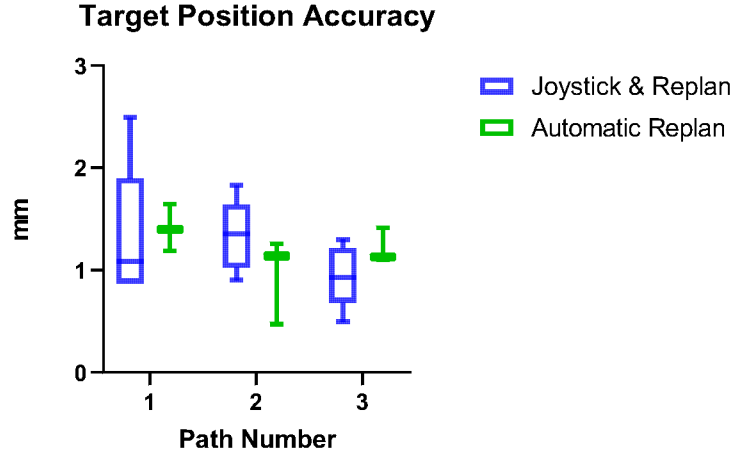
Figure 6.12: Target position errors of *in vitro* validation of the system calculated for trigger-based path re-planning insertion with joystick controlled by an expert user (joystick re-plan) and automatic fast re-planning insertion across three different paths
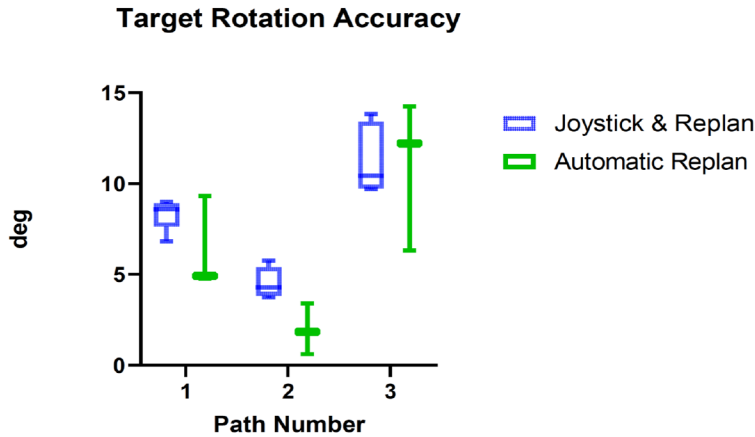
Figure 6.13: Target rotation errors of *in vitro* validation of the system calculated for trigger-based path re-planning insertion with joystick controlled by an expert user (joystick re-plan) and automatic fast re-planning insertion across three different paths

6.4 *Ex-vivo* and surgical workflow assessment

A validation of the full system in an *ex-vivo* clinical setting was performed using an animal model *ovis aries* (average $70\,kg$, female, one year old). This study was conducted under the European Communities Council Directive (2010/63/EU), adhering to the laws and regulations on animal welfare enclosed in D.L.G.S. 26/2014 and approved by the Italian Health Department with authorization n° 635/2017.
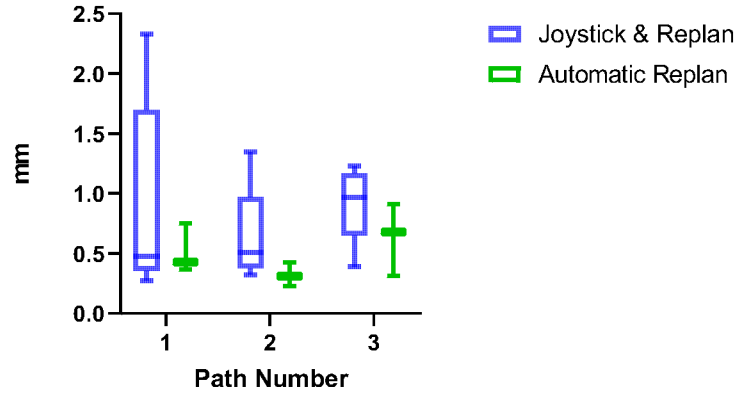
Figure 6.14: Updated path and corresponding new target position errors calculated for trigger-based path re-planning insertion with joystick controlled by an expert user (joystick re-plan) and automatic fast re-planning insertion across three different paths

The trial assessed the surgical workflow for forthcoming *in-vivo* trials, therefore for this work, the description of some steps such as anesthesia and animal preparation have been omitted for brevity.
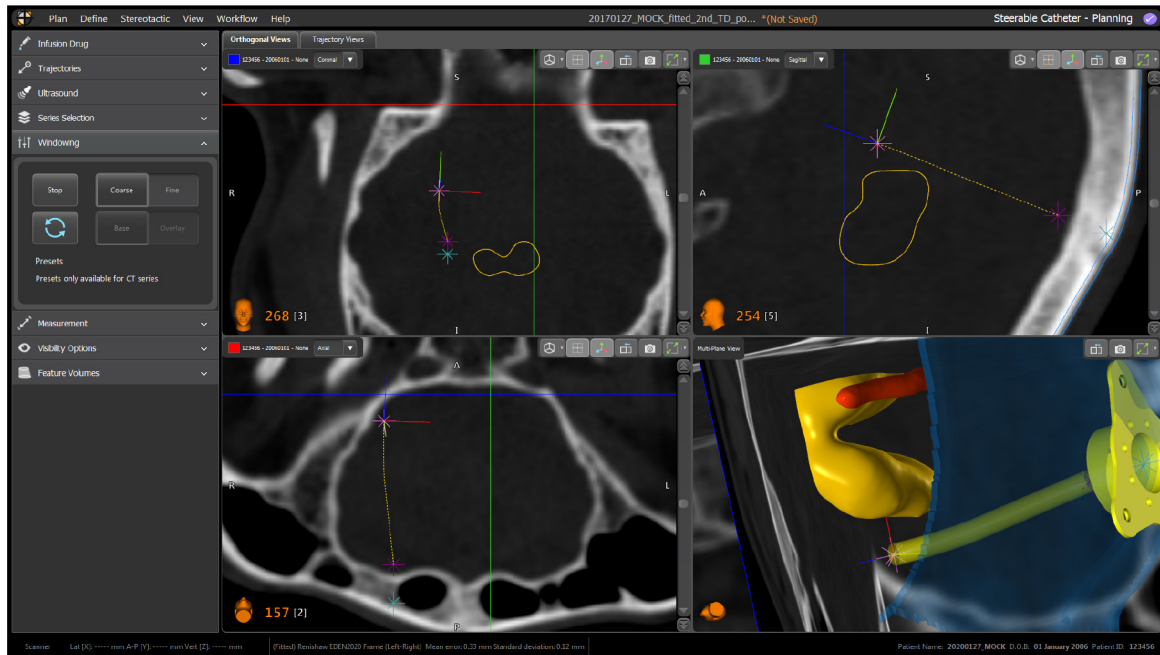
Figure 6.15: Software interface for pre-planning: conventional image view (in in clockwise order from the top left: axial, sagittal, 3D rendering and coronal). The marker T represents the target; the orange meshes are the obstacles (ventricles and veins); the blue mesh is the skull surface. In yellow a feasible entry points

The embedded sensors used were FBG fibres as in [KDG+20a]. The fibres were inserted inside

one of the two working channels of each segment and secured at the tail end of the catheter to avoid relative motion during the insertion. The procedure is divided into seven macro steps as follows:

- The sheep is located on a spinal stretcher (acrylonitrile butadiene styrene, ABS stretcher, Millenia, Ferno) and is secured in a prone position on a vacuum mattress with extended legs, via two straps.

- The Head Frame System of Figure 6.16 described in [TBZ⁺ew] is placed onto the stretcher and secured using a bespoke fixture system

- The animal head is fixed into the Head Frame System

- Acquisition of the pre-operative CT imaging sequence (CT-pre - GE Healthcare CT system, 16 slices helical scan). The imaging sequences were acquired with standard display field of view (DFOV), matrix of 512x512, slice thickness of $0,625\,mm$, 120 kilovolt (KV), 220 milliampere (mA), pitch $0,562:1$ and $1/s$ tube rotation. The images were collected using a soft tissue algorithm)

- Acquisition of a pre-operative MRI (Siemens 1.5T, 3DT1 Fast-Field-Echo (FFE), DTI, TOF). DTI imaging is loaded from a dataset of a previous study [PTC⁺19]

- The surgeon performs the pre-operative planning sequence following steps in section 6.1.1

- The surgeon performs the intra-operative planning and navigation sequence in section 6.4.1

- A second CT imaging sequence is recorded (post-CT) to assess the positioning of the catheter

6.4.1   Intra-operative planning sequence

The following procedure (Step 6) is carried out once the pre-operative planning is completed:
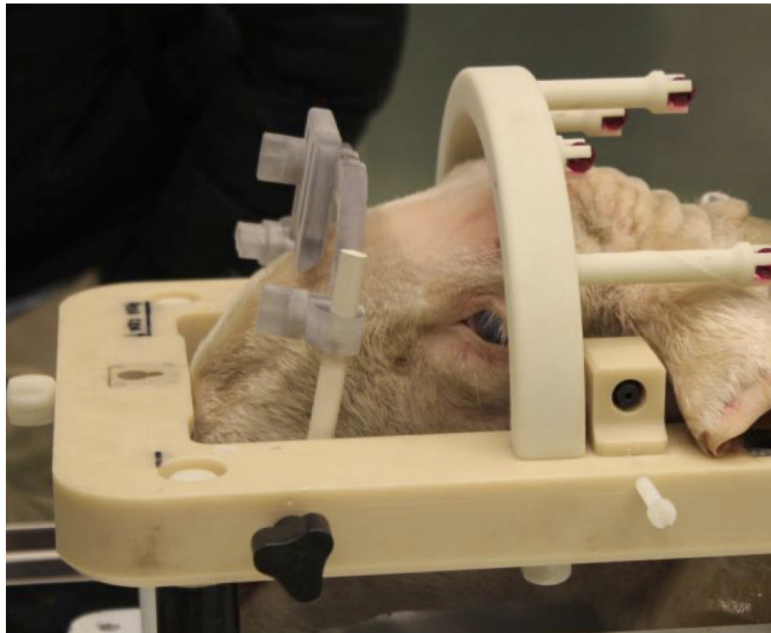
Figure 6.16: Ovine head clamping system described in details by [TBZ$^+$ew].

Figure 6.17: Surgical perforator mounted at the end-effector of the neuromate$^{\circledR}$. On the zoomed window: the profile left on the skull by the surgical perforator.

- The surgical pre-operative plan is loaded into the front-end interface

- A bespoke drill holder for the neuromate$^{\circledR}$ is mounted and, once the robot is placed in position, a keyhole on the skull is made as in Figure 6.17 (the tools to perform the keyhole
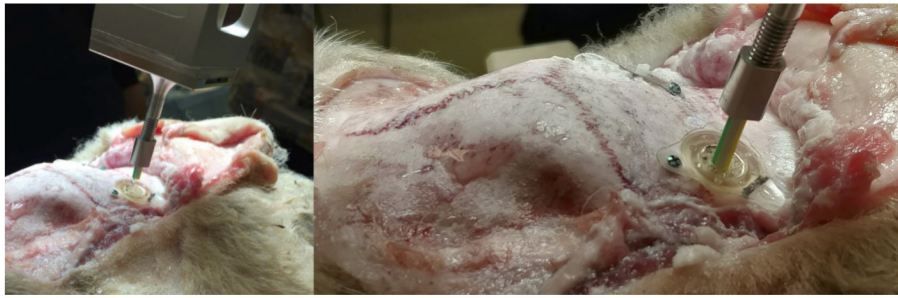
Figure 6.18: Catheter during entry point on the skull. Once the catheter reaches the target, it is secured to the skull by means of a bespoke port.
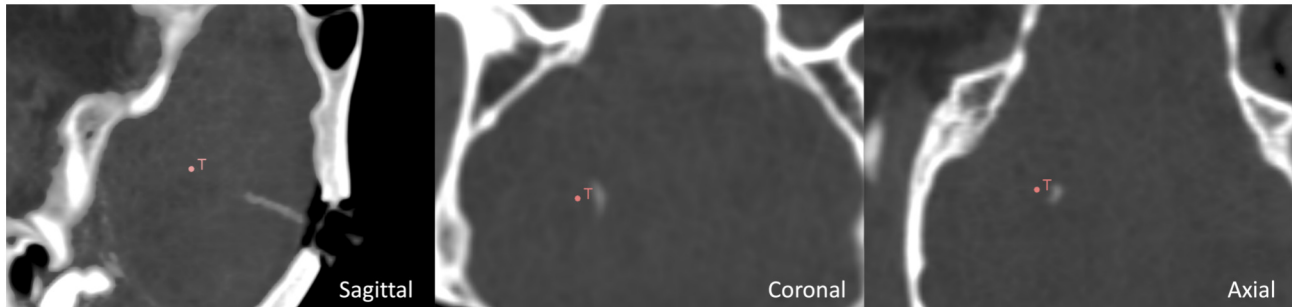
Figure 6.19: Ex-vivo post CT image. T define the target point, while the white shadow is the catheter

are: J&J Anspach® EMAX® 2 Plus with gearbox reduction and a cranial perforator model Codman 14mm).

- The surgeon creates a small incision on the dura

- A bespoke burr-hole port is placed into the keyhole and secured using titanium screws as in Figure 6.18.

- The neuromate® end-effector is moved back to the parking position, and the drill holder is replaced with the robotic catheter driver end-effector as in Figure 6.3

- The neuromate® end-effector is positioned over the burr-hole port and the catheter is automatically driven to the entry-point position in the brain as shown in Figure 6.18

- The front-end interface is switched in the catheter-view mode as in Figure 6.5 and the control of insertion is passed to the surgeon

- The surgeon starts the insertion by pressing a foot-switch pedal. The PBN is inserted at a constant speed of 1mm/s, and the direction is controlled by the haptic-joystick operated

by the surgeon. If the foot pedal is released, the catheter pauses the insertion. If the foot-switch pedal is pressed again, the insertion is restarted.

- The intra-operative planner described in Chapter 5 constantly adjust the insertion path depending on the current tip and target pose.

- Once the target is reached, the surgeon secures the catheter on the skull by using an inner locking mechanism in the burr-hole port

- The sensing embedded in the catheter is removed by pulling the fibres from the tail of the catheter

- The catheter is cut flush to the top surface of the burr-hole port and the robot end-effector is moved to the parking position

At the final step of the procedure, the front-end interface provides a message reporting which coloured segment of the PBN is suitable for the infusion. The infusion of the drug is delivered with an additional catheter with an outer diameter of 0.3mm and an inner diameter of 0.1 mm, inserted in the desired segment's working channel. This latter part of the protocol, as well as the infusion performance, are out of scope for this work. Following the surgery, a CT image is collected to define the final position of the catheter with respect to the surgical plan (Step 7). As shown in Figure 6.19 representing the post-CT imaging of the *ex-vivo* trial, the catheter has reached the target with an error in position of 1.42 mm. The *ex-vivo* target position accuracy is, therefore, in line with *in-vitro* results (Section 5.3.2). More *ex-vivo* tests are needed to statistically compare *in-vitro* and *ex-vivo* perfomance and to assess the influence of a more realistic *ex-vivo* setup on the PBN performance.

6.5   Conclusion

In this chapter, the EDEN2020 full modular robotic ecosystem is presented, which is used for neurosurgical applications and employs a programmable bevel tip needle. The design has

taken into account the functional requirements of the operating theatre (OR), from ergonomics to sterilisability. The front-end interface, as well as the workflow, have been developed in collaboration with a clinical team within the European consortium EDEN2020, to provide a system which is employable in the OR, without disrupting the current clinical flow. The path planning methods described in the previous chapters are integrated within the EDEN2020 ecosystem and tested first in a simulated environment and then both *in-vitro* and *ex-vivo*. Our intra-operative solution demonstrated its potential in guiding not expert users to a precise target pose. Particularly, replanning-as-control technique provided better *in-vitro* results than trigger-base path replanning, confirming that stronger guidance approaches might be preferable for less intuitive technologies as steerable needles even in the case of expert users. Overall, these trials confirmed the overall performance in position accuracy of the catheter, which are comparable to the results of analogous systems [MVO$^+$18a], both in bench-testing and *ex-vivo* assessment.

The system will require further investigation and *in vivo* trials to improve the efficiency in catheter placement and to assess the performance in CED applications. Future works will include an extensive evaluation of the system in ex vivo and in vivo models, with additional sensing such as Ultrasound Imaging to provide measurements of tissue deformation during operation. The additional sensing will also be fused with the embedded sensing to provide intra-operative localisation of the catheter tip. This integration will allow the system to compensate target migration from tissue deformation, that can affect the final positioning accuracy of the catheter at the target and along the path.

Chapter 7

Computer Assisted Planning for Curved Laser Interstitial Thermal Therapy

In this chapter, a CAP method for curved interstitial thermal therapy or LITT is presented. This neurosurgical application demands not only for target accuracy but for optimal ablation of a target volume. The research presented is an edited version of research recently pubished:

Marlene Pinzi, Vejay Vakharia, John Duncan, William Anderson, Brian Hwang and Ferdinando Rodriguez Y Baena, "Computer Assisted Planning for Curved Laser Interstitial Thermal Therapy" Transaction on Biomedical Engineering (TBME), Jan 2021.

7.1   Introduction

Several surgical disciplines have seen significant advances in the last decade, with the introduction of novel robotic and endoscopic tools that have aided more extensive resections through minimally invasive corridors [WGJD08, ABB20]. Amongst these, steerable needle technologies have been tested for different neurosurgical applications. Stereotactic needle-based

brain biopsies [MVO⁺18b], deep brain stimulation [HBM⁺19, PRH⁺16, SPF⁺19b], stereoelectroencephalography, stereotactic needle-based aspiration [BSL⁺13], stereotactic brachytherapy [KDH14] and intracerebral drug delivery [ZDB19, HAE⁺15] could all potentially benefit from steerable needle technologies. Another needle steering application, yet to be investigated, is laser interstitial thermal therapy (LiTT). LiTT provides a minimally invasive alternative to conventional open surgery [HWH⁺17] for drug-resistant mesial temporal lobe epilepsy (MTLE), which is the most common drug-refractory focal epilepsy [Cen05]. Recent studies suggest that higher seizure freedom rates are correlated with maximal ablation of the mesial hippocampal head, whilst sparing of the parahippocampal gyrus (PHG) may reduce neuropsychological sequelae. Current commercially available laser catheters are inserted following manually planned straight-line trajectories, which cannot conform to curved brain structures, such as the hippocampus, without causing collateral damage or requiring multiple insertions. The clinical feasibility and potential of curved LiTT trajectories through steerable needles has yet to be investigated. This is the focus of this chapter.

7.2 Background

Selective amygdalohippocampal complex (AHC) ablation with LiTT is currently performed by means of a straight catheter featuring a laser tip which is inserted through the brain along the longitudinal axis of the hippocampus to the anterior border of the amygdala. The extend of the ablation can be modulated through MR-thermography to generate an ablation diameter between 5 to 15 mm. Recent studies demonstrated that post-ablation seizure freedom (defined as "Engel I" outcome) are correlated with maximal ablation of the mesial hippocampal head, amygdala and the entorhinal cortex (EnCx), while sparing of the parahippocampal gyrus (PHG) and collateral structures may reduce the probability of neuropsychological complications [WJC⁺19a, DLV⁺15]. Additionally, a multi-center validation study by Galovic et al. [GBWG⁺19] supports the importance of resecting the temporal portion of the piriform cortex (PiCx) during temporal lobectomy, resulting in increased odds of achieving seizure freedom by a factor of 16. The most common LiTT-related neurological complications are visual field

deficits, ranging from 5 to 29% of total cases [JKS+17, WOS+15]. Visual deficits arise from heat transfer to the optic radiation or the lateral geniculate nucleus (LGN) during the ablation process.

Automated computer assisted planning (CAP) for straight tools has been proposed by Vakharia et.al [VSL+18, LVS+19] to generate optimized paths that maximize AHC ablation, spare the PHG and maintain a safety distance from the brainstem, LGN, sulci and vasculature. The machine learning-based method was validated in a multi-centre retrospective study [VSL+19] in which three automated straight trajectories and corresponding outcomes, featuring different entry point and target constraints, were compared to manually planned and implemented paths in 95 MTLE patients. The results showed a significant improvement in safety parameters and amygdalohippocampal complex ablation volumes and blinded external expert reviewers preferred the CAP trajectories over the manually planned trajectories.

However, the hippocampus features a distinctive curved shape that is generally very challenging to ablate in one single trajectory without damaging nearby structures, avoiding vasculature, transgressing the ventricular ependyma, as well as not being feasible in patients with abnormal anatomy. A trade-off between total target ablation coverage and minimum collateral damage is difficult to achieve even for automated methods based on straight tools. In some circumstances, more than one trajectory is necessary to achieve a successful ablation [CPG+17], thus increasing operative time and surgical risk. Additionally, a suboptimal ablation, due to the limited flexibility of currently available laser tools, resulted in 46% of patients requiring follow-on surgeries to achieve seizure freedom in some series [GAL+19].

A curved trajectory through a steerable needle could provide a better trade-off between coverage of the target area and damage reduction to collateral structures, while facilitating the inclusion of EnCx and PiCx, as recently reported in terms of Engel I outcomes for correlated structures [JKS+17, WJC+19b]. D.Comber et al [CPC+17] proposed a patient-specific design of concentric tube needles for a transforamenal approach to access the hippocampus. In this study, for each of the 20 selected hippocampi, a concentric tube robot was designed and optimized to traverse a trajectory from the foramen ovale to and through the hippocampus, from head to tail. Patient-

specific needles were rapidly fabricated featuring a precurved of up to 32.4 mm^{-1}. However, the insertion path was selected to simply match the hippocampus centerline and ablate the AHC. Consequently, to date, there are no studies proposing the computation of curvature-bounded optimized paths for steerable needles in the context of LiTT, taking into account ablation parameters and the optimization of chance with respect to seizure-free outcomes.

Here, we propose a computer assisted planning (CAP) algorithm able to maximize AHC, EnCx and PiCx ablation whilst minimizing damage to the PHG and surrounding structures. Surgeons will be able to fine-tune LiTT related parameters during the preoperative phase and interactively assess the generated path looking at the corresponding expected ablation of brain structures, both in the standard surgical 2D view and in a 3D rendering. In this work, a three-dimensional path planner for systems with nonholonomic constraints in complex environments is developed. A Bevel tip needle is considered to be a nonholonomic system, that is to say, one with nonintegrable velocity constraints [RJWKC+06]. Our own design is that of the EDEN2020 programmable bevel tip needle (PBN) [FKT+10c]. PBNs are able to steer along three-dimensional paths without duty cycle spinning along the insertion axis (as in [MEFR07]), and thus offer an ideal solution for the path planning technique described in this work. With this study we aim to show the potential of steerable needles, such as the EDEN2020 PBN, to improve the efficacy of LiTT procedures whilst improving safety. This is the first clinical application of preoperative planning for steerable needle based LiTT. Among its novel features we distinguish:(1) A GPU accelerated algorithm for patient-specific optimisation of curved LiTT ablation volume; (2) Ablation of the piriform temporal portion (PiCx) which is included for the first time in a LiTT CAP assessment; (3) Optimisation of the laser ablation diameter for each ablation step to achieve more precise targeting of the lesion; (4) The introduction of a new combined cost function for curved LiTT to rank the generated paths with respect to both patient risk and path smoothness. Finally, we assess generated curved CAP LiTT trajectories on five patients with hippocampal sclerosis (HS) and compare the results of target structure ablation (Amygdala, Hippocampus, EnCx and PiCx), collateral damage (temporal white matter, PHG and fusiform gyrus) and associated trajectory risk metrics with respect to a previously published straight CAP LiTT studies method [VSL+19, LJL+17b].

7.3   Curved Computer Assisted Planning

In this chapter we introduce a novel curved LiTT CAP which optimizes a path for mesial temporal lobe epilepsy treatment. The principal mechanism behind LiTT is to selectively ablate tissue of interest by heat produced from an optical fiber. The optical fiber is inserted into the mesial temporal lobe through a small hole made in the skull and its location is confirmed under MRI guidance. The tip of the laser fiber produces heat, resulting in an approximately spherical ablation of the surrounding target tissue area. The fiber is then pulled back in small interment steps and the procedure is repeated to cover the complete target volume. Our method aims to minimize path length, overall curvature, ablation of PHG and surrounding critical structures such as the LGN, fusiform gyrus (FuG) and temporal white matter (WM). On the other hand, the algorithm maximizes the ablation of the hippocampal head and body, amygdala, EnCx and the PiCx, which are structures correlated with the Engel 1 outcome in MTLE patients [JKS+17, WJC+19b]. Trajectories that do not meet the constraint of a 120 mm maximum length and $\rho = \frac{1}{35} mm^{-1}$ maximum achievable needle curvature are rejected. The latter was chosen on the basis of a previous study [CPG+16], which estimated the average curvature of the AHC complex for steerable needle designs to have a radius of 49.015 ± 14.79 mm, from which we derived a reasonable minimum radius of 35 mm. Furthermore, simulation and experimental results on the EDEN2020 PBN [WSB19b, TDR+20] show that similar curvature can be reached by increasing the needle stiffness, reducing its size and tuning the tip offset [TDR+20]. Paths colliding with obstacles such as the atrium of the lateral ventricles, vasculature and sulci, or less than 7.5 mm away from the brainstem and LGN, are also rejected, as in [LVS+19, VSL+19], to prevent excess heat transmission.

The distance from critical structures such as the vasculature and sulci is optimized by means of a risk score, first introduced in [VSL+18, LVS+19]. This metric, normalized to to be within the [0,1] range, measures the overall path risk as the cumulative distance from critical structures along the entire intracerebral trajectory. The minimum distance here is set to be 3 mm, as in Li et al. [LVS+19], so that a path having a risk score equal to zero is constantly at more than 10 mm distance from obstacles, while a risk of 1 corresponds to a path being continuously at

3 mm from obstacles.

The proposed CAP consists of a combination of two different planners. The first one addresses the optimization of the portion of the path in correspondence of the target ablation area, which we will refer to from now as the "ablation path". It aims to calculate a trajectory which optimizes the overall ablation of the targeted area, while reducing collateral tissue damage. The second is based on the previously presented adaptive fractal tree [LGCSR16] and adaptive hèrmite fractal tree (AHFT) [PGR19b] path planner techniques and aims to find a curvature-bounded obstacles-free path to connect the ablation path to a suitable entry point on the patient skull; we will refer to this portion of the path as "AFT-connection".

7.3.1 Ablation Path

The first step involves the generation of a so-called "ablation field map" (Figure 7.1). A GPU accelerated algorithm evaluates each voxel of the obstacle map in parallel. On each thread, given an homogeneous ablation diameter D_a, a sphere centered on a specific voxel is considered. The search space within the sphere is evaluated; the number of voxels belonging to obstacle regions N_d are counted as unwanted tissue damage; the voxels belonging to the ablation target area N_a are counted as successful tissue ablation; while the voxels not belonging to the previous categories are counted as additional tissue damage N_r. A normalized score S_v in the range [0,1], computed as the weighted positive contribution of the percentage of damage and additional tissue ablation plus the negative contribution of percentage ablated target area, is associated to each voxel, thus generating an ablation field map (Equation 7.1). The weights associated to damage W_d, target area ablation W_a and additional tissue ablation W_e can be tuned by clinicians to capture the desired trade-off between target ablation and collateral damage.

$$S_v = -W_a * \frac{N_a}{N_T} + W_d * \frac{N_d}{N_T} + W_e * \frac{N_r}{N_T} \tag{7.1}$$

Given the generated ablation field map, the ablation path can be optimized accordingly. Specifically, the search map section delimited by the tectal plate (which generally identifies the tran-
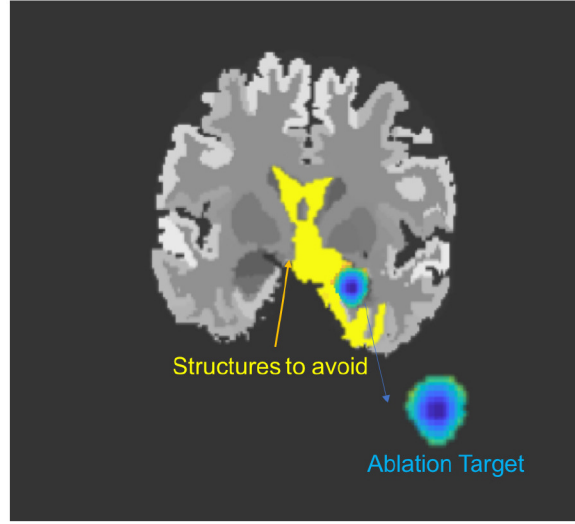
Figure 7.1: A coronal slice of the generated ablation field is shown as an overlay of the brain parcellation. The ablation target region features a darker area corresponding to lower "S_v" values, thus better ablation performances and less collateral damage.

sition between the hippocampal body and tail) and the anterior border of the amygdala, is selected. Then, for each cross section, the first ranked voxel position in the corresponding ablation field map is included as part of the optimized ablation path, which is then smoothed using a convex optimization based technique [MP20] that accounts for the given curvature constraint. At this stage, we extend the optimization to the more complex case of a non-uniform D_a. This provides an improved LiTT clinical scenario in which clinicians could benefit from fine tuning the ablation diameter value at each step of the catheter insertion, within a range between 5 and 15 mm, thus increasing their ability to precisely conform the ablation to the target structures. Given a predefined ablation pullback (7 mm is our default value), a second GPU accelerated algorithm is implemented to optimize the laser ablation diameter value for each step along the ablation path. In this process, each ablation step is represented as a series of overlapping spheres, thus approximating a cylindrical ablation volume around the given path (Figure 7.2). The spheres' radius is progressively increased in steps of 0.5 mm from 2.5 to 7.5 mm. A score S is associated to each cylinder, as in Equation 7.1, so that the first ranked cylinder dictates the value of the optimized D_a associated to that portion of the ablation path. At the end of the computation, the optimized D_a for each ablation step is provided. Additionally, the volume overlap with the amygdala, hippocampus, EnC, PiCx, PHG, FuG and WM, as determined from
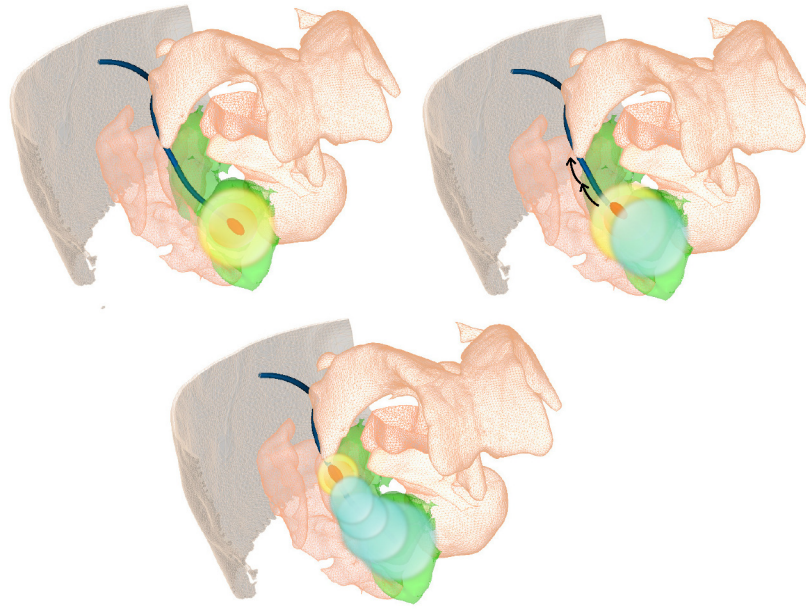
Figure 7.2: The series shows LiTT performed along a curved path. The ablation field around the laser tip is represented by a yellow sphere. Starting from the deepest target point, the laser fiber is progressively extracted at a predefined step and the laser power is tuned to cover the desired laser ablation diameter. The overlapping ablation spheres finally result in a beam-shaped ablated volume (light blue)

the brain parcellation, is automatically calculated. Finally, the estimated ablation volumes are normalized by the preoperative volume to provide the percentage of ablation for each structure and an overall target % ablation as the sum of the contributions of all target structures.

AFT-connection

An adaptive fractal tree (AFT) based planner is used to find a path connecting the patient's skull to the initial pose of the ablation path. Surgical constraints for this portion of the path capture the angle of insertion with respect to the the skull normal, which should be close to perpendicular in order to prevent skidding of the cranial perforator, and the predefined safety margin from sensitive brain structures along the entire trajectory. In addition, the kinematic constraints of the flexible catheter require the generation of a curvature-bounded path which is assessed in terms of smoothness and length through a cost function. In this study, we are interested in trajectories matching not only the desired target position (corresponding to the first point of the ablation path) but also its orientation, in order to guarantee tangent

continuity on the overall trajectory. To do so, we implemented some of the techniques discussed in [PGR19b], which optimize the choice of AFT parameters specifically for neurosurgery and provide different methods to take into account the goal pose accuracy, which includes both target position and target approach angle accuracy. A fractal tree is grown from an entry pose perpendicular to the patient's skull, then a "reachability volume" with the shape of a horn torus is placed in correspondence of the goal pose and directed towards the patient skull to filter only those samples laying within. The horn torus radius corresponds to the maximum needle achievable curvature and ensures that the AFT obstacle-free paths, laying within, meet the desired target pose and curvature constraint. The full path obtained from the combination of the ablation path and the AFT-connection is finally smoothed to guarantee continuity and avoid potential misalignment. The generated paths are evaluated by mean of a normalized score S_p (Equation 7.2), which corresponds to the weighted contribution of two terms: Sm and $Risk$ for all N path samples. The first corresponds to a cost function, introduced in [PGR19b], that measures the path smoothness in terms of overall curvature (C_i), gradient of curvature between consecutive points (C_{i+1} - C_i) and length of the given trajectory ($length$). More linear and shorter paths are favoured to reduce the extent of tissue damage and facilitate the needle insertion. The second term is taken from the study by Li et al. [LVS+19] and captures the risk of a given path in terms of overall distance from vasculature and sulci, with a minimum distance $Dist$ of 3 mm. Paths that are further away from vessels are favoured, since they reduce the chance of a potential hemorrhage. Both terms are normalised within the [0,1] range and their weight W_s and W_r can be tuned according to surgeon preference.

$$
\begin{aligned}
S_p &= W_s * Sm + W_r * Risk \\
Sm &= \sum_i^{N-1} \frac{|C_{i+1} - C_i|}{2 * max_{curv}} + \sum_i^{n_{seg}} \frac{|C_i|}{max_{curv}} + \frac{length}{max_{length}} \\
Risk &= \begin{cases} \sum_i^N \frac{10 - Dist(i)}{N(10-3)}, & \text{if } Dist(i) > 3 \\ 1 - \sum_i^N \frac{3 - Dist(i)}{3*N}, & \text{if } Dist(i) \le 3 \end{cases}
\end{aligned}
\tag{7.2}
$$

7.3.2   Dataset

Following ethics approval provided by the National Research Ethics Service Committee, with approval reference 12/LO/0377, five patients from the National Hospital for Neurology and Neurosurgery epilepsy surgery program were included in this study. For each patient the following diagnostic images were provided: single T1 MPRAGE acquisition with a voxel size of 1 mm isotropic (TE/TR/TI = 3.1/7.4/400 ms; flip angle 11; parallel imaging acceleration factor 2), whole-brain parcellation and synthetic CT (pseudo-CT), images were generated using geodesic information flow [CMW+15] and a multi-atlas information propagation scheme [BCM+13], respectively.

7.3.3   Simulations

Patient-specific 3D models of the ventricular system, sulci, brainstem, PHG, FuG, AHC, EnC, WM and PicX were extracted from the whole brain parcellation. In particular, the brain stem (including LGN) was expanded by 7.5 mm to avoid any ablation related damage while ventricles, PHG, FuG, WM and sulci were merged with the vasculature segmentation to create an obstacle map, which is then expanded with a tunable safety margin, set as 1.5 mm by default (Figure 7.4). This takes into account both the needle occupancy and real-world uncertainties and it is more or less conservative depending on the geometry of the flexible tool considered. Currently used straight needles are about 0.8 mm in radius (i.e. Medtronic Visualase^{TM}), while flexible catheters are generally larger, reaching up to 2.5 mm in diameter [FKT+10b, SMG+20]. Similarly, 3D models of the amygdala, hippocampus, EnC and temporal PiCx constitute the ablation target area for the proposed curved CAP LiTT (Figure 7.3). The ablation path is calculated for each patient's anatomy, W_a and W_c are set to 1 and 0.5 respectively, while W_d is progressively increased in steps of 0.5 starting from zero until the PHG damage rate reaches a maximum of 16%. This threshold has been arbitrarily fixed looking at clinical accepted values and optimized straight LiTT CAP results from the literature, which show average PHG damage rate of 21% for manual insertions and 12% for straight CAP trajectories [VSL+19]. The ablation step is set to 7 mm by default and the best ranked D_a is generated for each

insertion step, as previously described. The overall % of damage and % ablated target area, corresponding to the calculated ablation path, can be interactively assessed by neurosurgeons, and both a 3D rendering and a 2D overlay aid them during this process. A pseudo-CT is used to segment the patient's skull through simple threshold-based segmentation. A uniform mesh is then created from its surface, where the vertex coordinates represent possible entry points, and the associated normals represent the corresponding start approach vectors. Between these, a feasibility check with respect to the desired target pose is performed, as in [PGR19b]. This ascertains whether the start and target combination is feasible either in terms of maximum needle length or the maximum curvature constraint. The AFT-based planner runs over each entry pose to look for a connection with the given target pose, which coincides with the first pose of the ablation path. The resulting curvature-bounded and obstacle-free paths are merged with the previously calculated ablation path and ranked by means of the S_p score (Equation 7.2). Finally, the first ranked path and the corresponding ablation and damage areas are offered to clinicians for review (Figure 7.5).

7.4   Results

Following the implementation of a 5 mm to 15 mm variable laser ablation diameter, ablation results for the generated curved CAP trajectories are compared to their straight counterparts, generated with the machine learning based straight CAP described in [VSL+19]. A one sample t-test is used to analyse the difference between the means while an F-test evaluates the difference in the standard deviations. As illustrated in Figure 7.7 and Table 7.1: curved CAP results in a significant improvement in terms of greater % ablated, on amygdala, hippocampus, EnC (t-test, $p \leq 0.05$) and on the overall target area (t-test, $p \leq 0.01$); While a higher standard deviation was registered for the amygdala (F-test, $p \leq 0.05$) with respect to straight insertions [VSL+19]. Additionally, PiCx ablation is included for the first time during LiTT planning optimization, resulting in a great rate of ablation of its temporal portion for both curved and straight CAP, with no statistical difference.
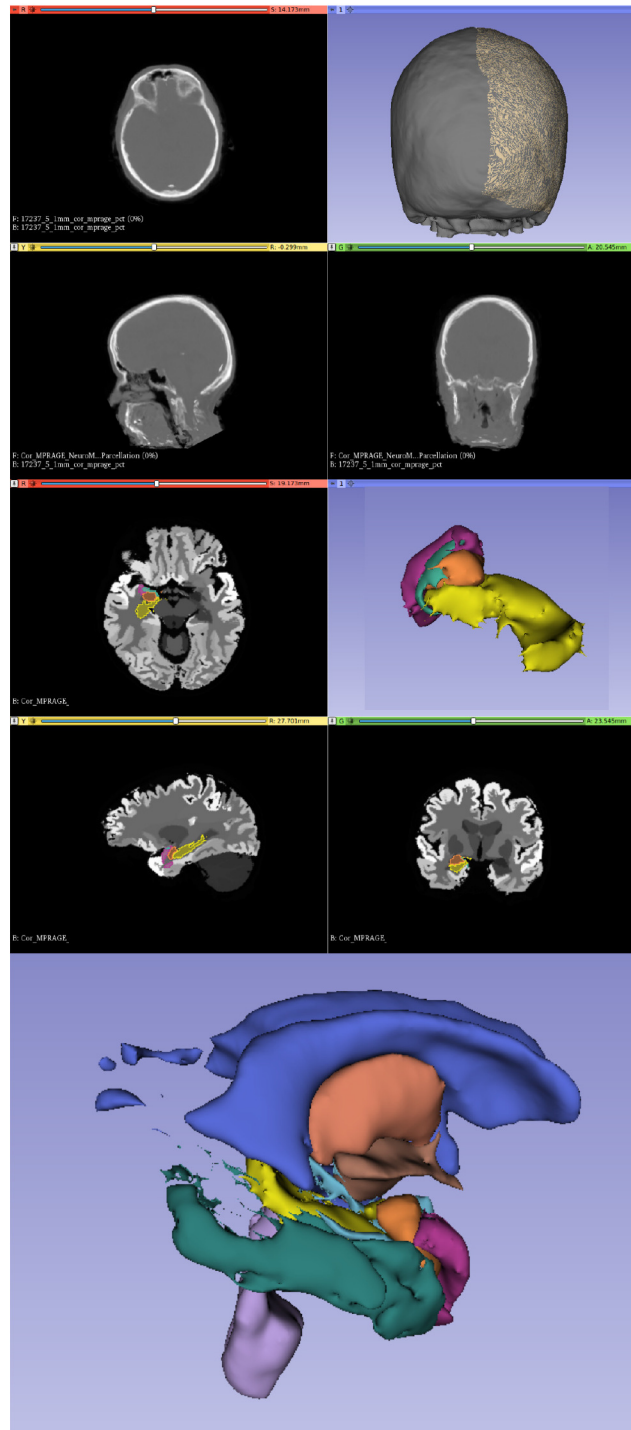
Figure 7.3: (Top) The pseudo-CT is segmented through thresholding and the skull surface mesh of the selected hemisphere is considered. (Middle) The ablation target regions are extracted from the patient's MRI parcellation: hippocampus (yellow), amygdala (orange), temporal piriform cortex (light green) and entorhinal cortex (purple). (Bottom) Sensitive brain structures surrounding the ablation area are also extracted from the parcellation: ventricles (blue), brainstem (violet), thalamus (salmon) and the PHG (light blue) on the back with respect to the FuG (dark green).
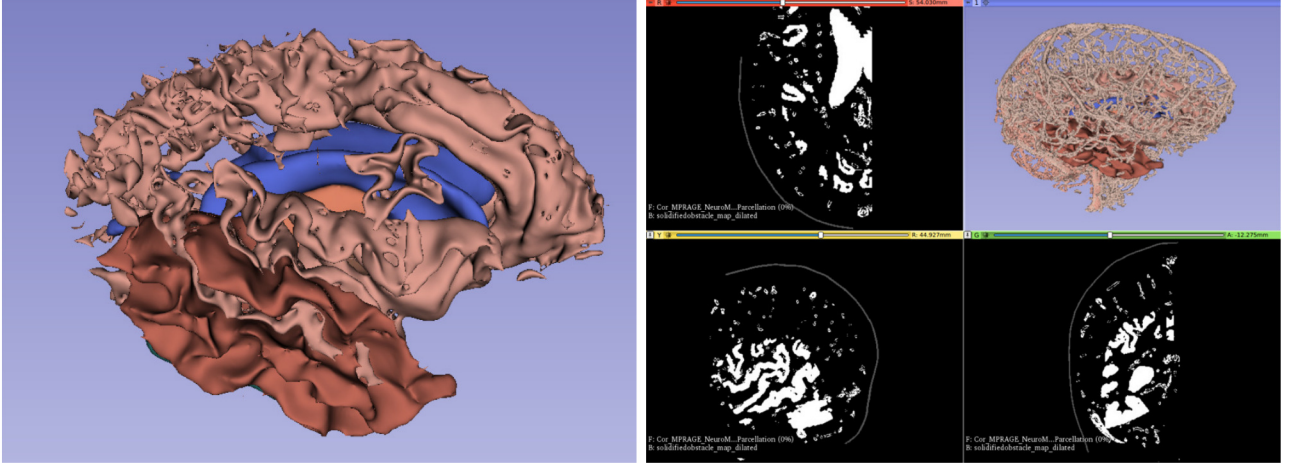
Figure 7.4: Sulci, temporal white matter and vasculature are part of the obstacle map. In the bottom, the resulting binary obstacle map is visualised in the three standard 2D views. The obstacles (white regions) have already been dilated by a safety margin (1.5 mm in this example).

On the other hand, damage to sensitive structures (Table 7.1: % ablation of non target areas) is minimised. The PHG ablation maximum tolerance was set to 16%, as this value has been shown to be acceptable both in past manual and automated LiTT planning results [VSL+19, LVS+19], with a significant reduction in % of ablation variance in the case of curved CAP (F-test, $p \leq 0.05$). WM and FuG damage rates are small for both curved and straight method, while the FuG standard deviation is statistically lower for curved CAP (F-test, $p \leq 0.01$). The smaller standard deviation, associated to % ablation of non target areas, suggests that greater flexibility could lead to higher CAP robustness.

With respect to safety metrics (Table 7.1: safety metrics), curved CAP-planned trajectories feature not significantly higher average intracerebral length (*Length*) with respect to straight paths. On the other hand, curved CAP trajectories resulted in a highly significant reduction in the computed overall risk (*Risk*) score (t-test, $p \leq 0.001$), based on a cumulative distance from critical structures (sulci and vasculature) along the entire length of the trajectory, thus reducing the potential risk of haemorrhage for patients. Finally, the cost function average value S_m for curved CAP is equal to 0.6, with a variance of ± 0.03.
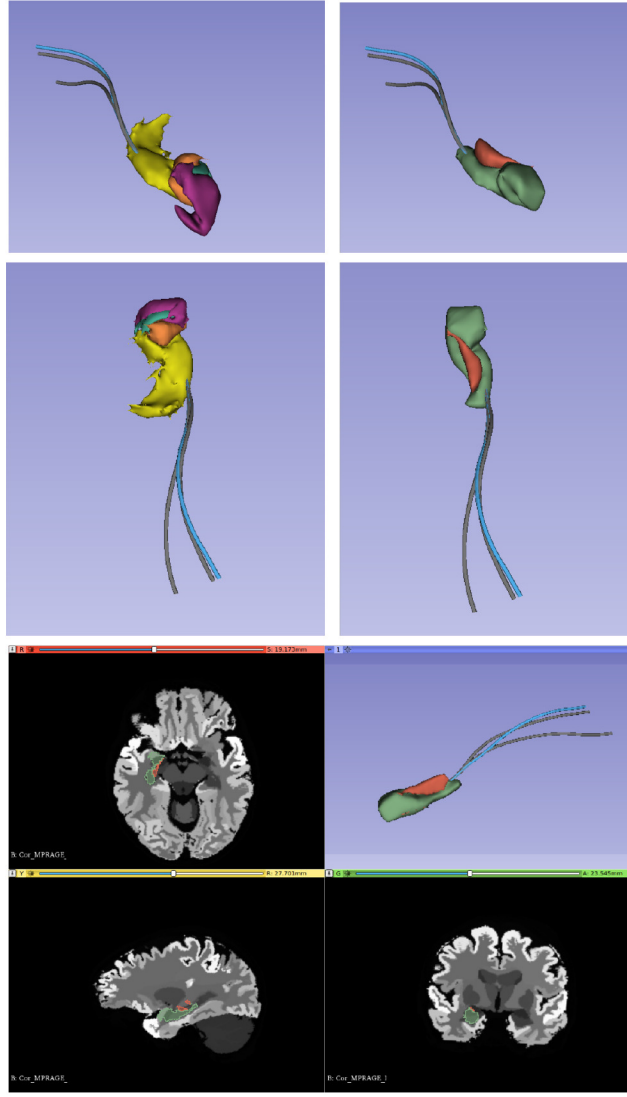
Figure 7.5: Three of the generated curved and optimised paths are shown in the top left column, together with the segmented ablation target regions; while the ablated target area (top right, green volume) and the collateral damage (top right, red volume) show the actual performances associated to the best ranked path (blue).

7.5 Discussion

The proposed curved LiTT algorithm presents enhanced flexibility, thus greater ability to cope with several constraints associated to better patient outcomes. The generated trajectories begin perpendicular to the patient's skull and advance through the brain meeting the hard constraints on the desired safety distance from all the predefined structures. A greater % ablation target area at reduced damage of PHG and nearby maesial sensitive structures is shown. The small standard deviation associated with both target area ablation and damage to sensitive structures demonstrates that curved ablation paths can handle different anatomies with
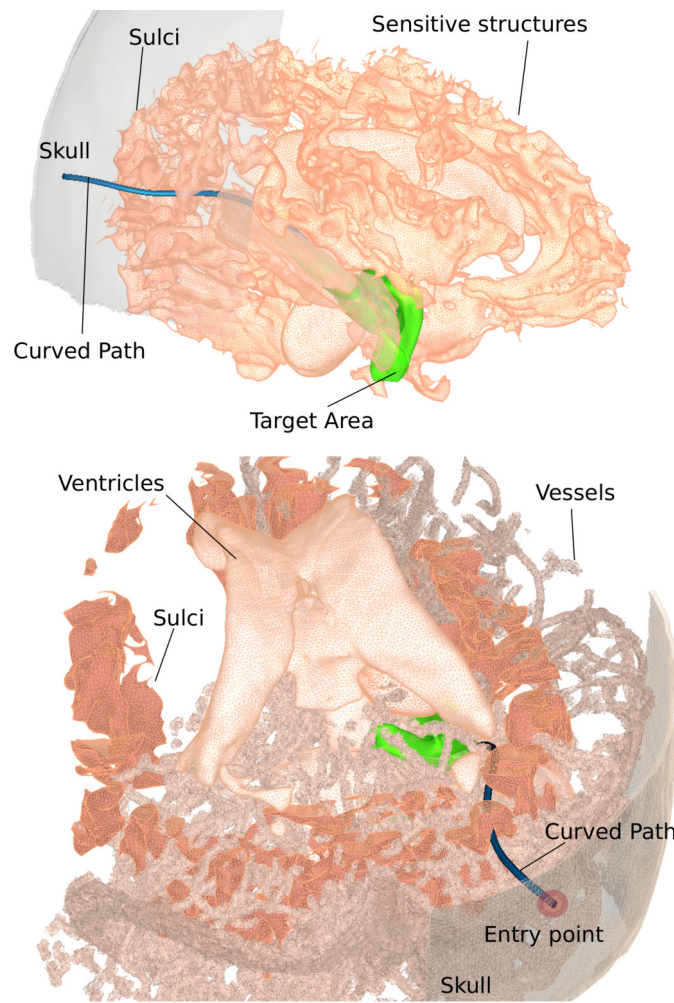
Figure 7.6: The best ranked path is shown to be collision-free within the intricate brain obstacle map. The map is cropped axially (bottom image) at the level of the specified path to show its sensitive structures avoidance.

equal performance. Also, the greater EnCx, amygdala and hippocampus ablation coverage and the inclusion of the PiCx at no expense of further PHG damage or smaller hippocampus ablation confirms the potential of steerable needles for LiTT. Furthermore, the ability of moving through a cluttered environment avoiding obstacles corresponds to smaller registered risk metrics and thus a reduced risk for patients. It is also worth considering that steerable needles are robotically driven systems that can be guided in real-time through soft-tissue to allow for small adjustments with respect to the preoperative plan, if needed. Their intra-operative flexibility could compensate for possible misalignments and tissue deformations, due to real-world uncertainties, which are responsible for erroneous placement and the need for follow-on LiTT surgery in up to 46% of patients [WPS+19]. Finally, performing the desired ablation with a single curved insertion may reduce the overall error rate which, especially in the case of multi-
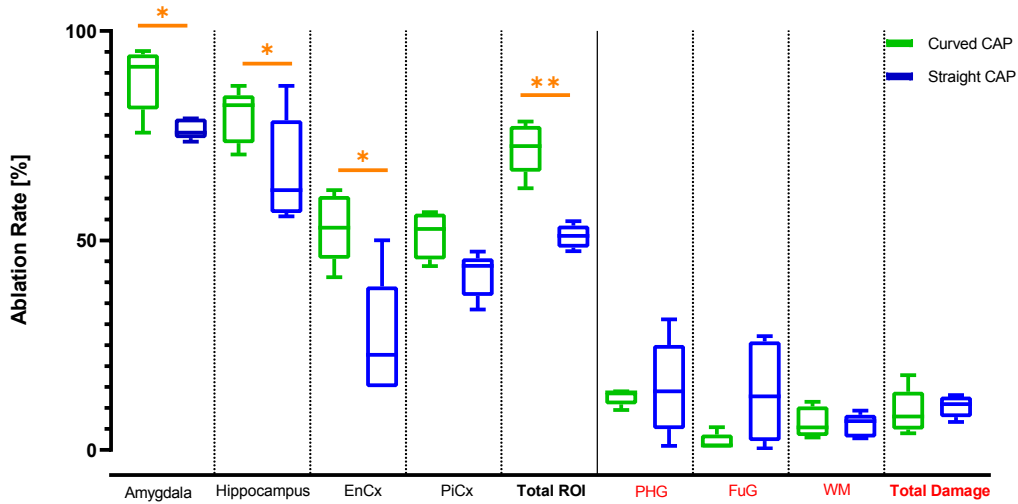
Figure 7.7: Box-plots of curved CAP % ablation (green) versus straight CAP results (blue). The statistical significance resulting from one sample t-test is shown using the p-value standard convention: * for p ≤ 0.05, ** for p ≤0.01, *** p ≤0.001, **** p ≤0.0001.

Table 7.1: LiTT: Curved CAP vs Straight CAP

% Ablation Target Areas

	Curved CAP	Straight CAP	t-test	F-test
Hippocampus	79.6±6.4%	66.5±12.8%	*	ns
Amygdala	88.6±7.8%	76.6±2.4%	*	*
EnC	53.1±8.2%	26.1±14.5%	*	ns
PiCx	51.3±5.6%	41.8±5.3%	ns	ns
Total	72±6.2%	50.9±2.8%	**	ns

% Ablation of Non Target Areas (collateral damage)

	Curved CAP	Straight CAP	t-test	F-test
PHG	12.7±1.9%	14.8±11.3%	ns	*
WM	6.6±3.7%	5.9 ±2.8	ns	ns
FuG	1.9±2%	13.8±11.9	ns	**
Total	9.1 ±5.3%	10.4±2.6	ns	ns

Safety Metrics

	Curved CAP	Straight CAP	t-test	F-test
Length	111 ±7.5mm	100 ±9.1mm	ns	ns
Risk	0.4 ±0.1	1.3 ±0.1	****	ns
S_m	0.6 ±0.03	NA	NA	NA

Curved CAP versus straight CAP Performance. Statistically significant results from one sample t-test and F-test are shown using the p-value standard convention: * for p ≤ 0.05, ** for p ≤0.01, *** for p ≤0.001, **** for p ≤0.0001, ns for not significant and NA for not comparable available data.

ple straight passes, equals the sum of all contributions. However, the generally larger diameter associated to current flexible catheters (e.g.[FFK+12, WSB19a]) could potentially cause more damage along the track, which means that further miniaturisation of this technology would be desirable. The EDEN2020 setup has already been tested within a standard surgical workflow during preclinical animal trials, demonstrating successful real-time performance and high target accuracy [SMG+20]. Following the results of this study, a new version of the existing EDEN2020 PBN, with smaller footprint and higher steerability will be developed. The proposed curved LiTT CAP algorithm will be included as an additional preoperative planner module within the EDEN2020 front-end interface. Autonomous path following under surgeon's supervision can be performed through adaptive path-following control [RS18]. To track the needle inside tissue, a system based on Fiber Bragg Gratings (FBGs) was being developed to track the needle tip [KDG+20b], as well as to sense the shape of each of the four needle segments, while intraoperative Ultrasound is used to provide information about real-time tissue deformation [GNH18]. The application of steerable needles in ablative therapies could also be beneficial in situations that require multi-trajectory planning, such as corpus callosotomy for generalized epilepsy. [VSV+].

7.6   Conclusion

This is the first fully automated CAP method for the generation of curved LiTT trajectories that maximizes both the ablation of mesial temporal target areas (hippocampus, amygdala, EnC and PiCx) and patient safety metrics, while minimizing collateral damage to nearby structures (PHG, WM and FuG). We have also presented the optimization of a variable ablation diameter field ranging between 5 and 15 mm diameter along the generated curved ablation trajectory and demonstrated that LiTT procedures could benefit from steerable needle technologies by tailoring the insertion path to the subject-specific anatomy. CAP methods provide an objective means of planning LiTT procedures that may overcome the heterogeneity existing between different surgeons and institutions. Future studies using larger datasets will be required to further assess and validate the exciting potential of the proposed method. It will follow the integration of the

proposed Curved CAP within a neurosurgical setup (i.e. EDEN2020 system) for *in-vitro* and *ex-vivo* trials.

Chapter 8

Conclusion

8.1 Summary of Thesis Achievements

In the introduction, the aims of the thesis were set out. These were:

- To assist surgeons during the pre-operative phase of steerable needles procedures requiring high accuracy on the final goal pose.

- To propose a computer-assisted planner for steerable needles that can generate safe and feasible paths according to neurosurgeons preference.

- To propose an intra-operative solution which compensates for tissue deformations and deviations from the pre-operative path.

- To demonstrate *ex-vivo* and *in-vivo* performance of pre-operative and intra-operative steerable needles path planning methods

- To explore a novel application for steerable needles in neurosurgery and demonstrate curved insertions potential over straights through a retrospective study.

In pursuit of the first aim, it was imperative to understand the potential of steerable needles technology in the operating room. Steerable needles can be actively controlled during the in-

sertion, compensating for target migration and needle deflection, thus providing high target accuracy. Additionally, delicate tissue (e.g. nerves or vessels) can be circumvented, and deep structures can be accessed, reducing related patients' risk. Different surgical fields and applications might benefit from this new technology; however, planning for steerable needle insertions might result counterintuitive to neurosurgeons due to their difficulty in exploiting steerable needle dexterity. Therefore, clinicians' desires need to be fully understood to promote the use of steerable needles, with their enhanced manoeuvrability, within the bounds of related surgical constraints. The thesis aims were pursued in part to aid the development of EDEN2020, an EU project which aims to deploy the PBN as a neurosurgical device to treat brain cancer. For this particular application, a radical new approach was needed to effectively address the current limitations related to poor targeting of infusion points [SAP+10] and suboptimal delivery of catheters [MPL+11] discussed in the introduction. For this purpose, the EDEN2020 project (Chapter 6) aims to address the key research challenges which stand in the way of a commercial robotically driven needle steering system.

With regard to planning and navigation, the following needs were identified:

- An intelligent planner which assist the surgeon to define the optimal catheter trajectory to a lesion

- A real-time intra-operative catheter insertion platform for accurate, adaptive path tracking in the presence of tissue deformation and real-world uncertainties.

In Chapter 3 and Chapter 4 surgical and technical constraints were assessed and taken into account for the development of computer-assisted pre-operative planning techniques for the application of steerable needles for precise surgery.

A GPU-accelerated path planning algorithm called AFT [LGCSR16], featuring high computational efficiency and great ability in finding solutions in very complex environments, was applied to the neurosurgical field. A sensitivity analysis of its parameters was performed, and optimal tuning for the neurosurgical context was found. Then, an extension of the AFT algorithm

called Ray-tracing AFT (3) was developed to aid clinicians during the patient-specific entry-point selection process. This method, similarly to available skull mapping techniques, provides guidance either during target pose selection or, once the target pose is already set, during entry point selection. The novelty of combining ray-tracing with a path planning method provides additional information on the feasibility of each plan, either in terms of target pose reachability or with respect to the desired entry angle tolerance. Contrary to straight needle pre-operative planning selection, neurosurgeons can benefit from interactively tuning the desired plan and relative entry pose while enforcing a hard constraint on the desired final pose.

However, in complex neurological planning such as the one proposed in EDEN2020, both the skull entry pose and the the drug delivery target pose might need to be defined *a priori*. Since the original AFT and the proposed AFT Ray-traced algorithms are not able to deal with both starting and final heading constraints, a new algorithm called AHFT (Chapter 4) was proposed to meet this additional requirement. The AHFT offers a robust technique to either refine the Ray-tracing AFT solution or provide new obstacle-free curvature-bounded paths connecting two given 3D poses.

Its performance was assessed first in a brain simulated environment and then tested on a commercial surgical interface, the NeuroInspire, both *ex-vivo* and *in-vivo* with positive feedback from clinicians.

The thesis follows with the illustration of an online intra-operative path re-planning method for accurate and adaptive path following in the presence of tissue deformation and real-world uncertainties. The target pose and the selected catheter pathway, computed individually for each patient during the pre-operative phase, are intra-operatively updated based on tissue deformation. Neurosurgeons specified the need for a re-planning method that could adapt the pre-operative plan to environmental changes during the insertion rather than recalculating an entirely new trajectory. To this end, we equipped a commercial system (NeuroInspire) with a state of the art, intelligent planning workstation and online re-planner, which fuse patient-specific imaging and therapeutic constraints with catheter limits and a deformable substrate to guide the surgeon along procedure-optimised trajectories.

The intra-operative planner adapts the path from the current needle tip pose while meeting the operational constraints on the desired target pose, obstacle avoidance, maximum achievable curvature and pre-operative plan proximity. The path adapts online, compensating for ongoing tissue deformation. The new path substitutes the reference one on the front-end visualisation with maximised path stability: a measure of the difference induced by the re-planning with respect to the reference plan. Preserving plan stability decreases the cognitive load on users observing the planned activity, by ensuring coherence and consistency of behaviours, even in a dynamic environment.

A proposed risk metric, measuring the feasibility of reaching the desired target from the current pose, triggers the path re-planning when the risk is above a predefined threshold. Results from multiple-user trials (Chapter 6, Section 6.2) suggest that the online updated path front-end visualisation leads to a statistically significant reduction in insertion position error standard deviation with respect to the pre-operative plan, thus indicating the influence of path re-planning visualisation on improved path stability and insertion guidance.

These results underline the advantages of further assistance during steerable needle insertions, especially in the case of a high maximum curvature constraint which prevents users from re-acting fast enough, thus interfering with the demanding target accuracy requirement. On the other hand, no statistically significant difference on the average final pose error was registered in these user trials. This may be due to the visual interface, which was part of an ongoing investigation, where its efficacy in guiding the users to the correct final pose was still under refinement. For this reason, a "replanning-as-control" framework, which naturally requires fast re-planning computation, was considered for a second study. This method allows the system to automatically steer the needle along the current path without using a joystick, but rather a "start and stop" approach where the user inputs the command via a foot pedal. Furthermore, this framework removes the need for a user to guide the needle insertion, thus avoiding this form of external influence on the trial's resulting accuracy. The combination of intra-operative sensing with path re-planning in a closed-loop fashion provided good accuracy results during *in-vitro* trials (Chapter 5), thus suggesting that the EDEN2020 PBN could benefit from automatic robotic guidance in delicate soft-tissue insertions and for maintaining a high level of

performance even for non-expert users.

Few path planning methods are currently able to take into account surgical and kinematic steerable needle constraints, especially if in the context of a very complex 3D environment such as the human brain. Therefore, our proposed techniques provide novel pre and intra-operative methods to aid both path planning selection and intra-operative path following accuracy in the field of PBN insertions for neurosurgery.

In light of the previous results and the clinicians' excitement for the EDEN2020 steerable technology, we started investigating new potential applications for steerable needles in neurosurgery. Among the existing procedures that could benefit from steering, laser interstitial thermal therapy (LiTT) for mesial temporal lobe epilepsy was found to have great potential due to the existing need for increased flexibility with respect to current straight LiTT tools in ablating deep brain curved structures. In fact, LiTT patients are currently found to suffer from visual field deficits, ranging from 5 to 29% of total cases [JKS+17, WOS+15], that arise from accidental heat transfer to the optic radiations or the lateral geniculate nucleus (LGN) during ablation. Additionally, current straight LiTT tools are associated with the erroneous placement and the need for follow-on LiTT surgery in up to 46% of patients [WPS+19].

A great collaboration with John Hopkins University Hospital and University College London (Department of Clinical and Experimental Epilepsy, Institute of Neurology) allowed us to closely understand the limits of the current commercially available straight technology in terms of low flexibility, usability and induced risk to the patient. Furthermore, surgical factors which were found to correlate with seizure-free outcomes were taken into account to realise an optimised curved LiTT computer-assisted planner (CAP). The generated curved CAP trajectories were evaluated on an dataset of epilepsy patients in terms of target area ablation, brain sensitive structures damage and overall risk with respect to previously published straight results. Improved safety and ablation distribution for the considered patients was shown in the simulations results in Chapter 7. This could also be beneficial to corpus callosum LiTT for generalized epilepsy, which currently requires multi-trajectory plans [VSV+20].

8.2 Limitations and Future Work

The main advantage of embedding one's Phd within a large-scale integrate program, is being able to apply your research directly and immediately realise impact. In EDEN2020, the PBN forms part of a neurosurgical system. It is being clinically evaluated through ongoing animal trials. The requirement of an effective path pre-operative planning and intra-operative re-planner method, taking into account precise surgical constraints, motivates this research: improvements in planning usability, efficiency and safety transfer to needle targeting accuracy and ultimately clinical outcomes. This thesis was able to contribute to the project in the areas of planning, intra-operative guidance and simulation. The proposed path planning techniques facilitate a surgeon to choose a preferential trajectory to follow during the insertion and control the needle curvature under disturbances, whilst maintaining proximity to the reference path.

In particular, future works on the Ray-tracing AFT (Chapter 3) path planning method could be focused on the integration of an augmented reality (AR) modality. Surgeons will be able to check the feasibility of the proposed entry regions looking directly at the patient skull by means of a tablet or an AR headset, in a more intuitive way with respect to standard surgical 2D visualisations and rendering. With regard to the AHFT planning technique (Chapter 4), full parallelisation of the algorithm should be considered. In particular, the OGH extensions departing from the AFT trajectories at different levels could be indipendently evaluated on the GPU. The voxel-based obstacle collision and the curvature check would then be performed in parallel in a similar way to the AFT method which covers the first part of the AHFT generated path. This would drastically reduce computation time at no-cost for the AHFT performance, thus facilitating surgeons interaction, similarly to the Ray-tracing AFT.

Moving to the intra-operative planning, while we demonstrated a successful planner, our physical experiments reveal that our needle dynamic model fails to perfectly model the needle motion, thus leading to inaccuracies and bigger deviations from the desired path. In addition, further studies under a real deforming environment will enable the full assessment of the proposed method. Future works will have to concentrate on mitigating dynamic model inaccuracies and assessing the algorithm's performance with more *ex-vivo* and subsequently *in-vivo* animal trials

planned with the EDEN2020 system. The *in-vivo* tests will feature a full setup including an intraoperative 3D ultrasound, hence the robustness of the replanner in compensating for realistic brain deformations will be evaluated. Additionaly, we show in this thesis that by integrating the needle mechanics-based model into the fast re-planning routine, it is possible to achieve more accurate trajectory following compared to joystick guidance results. An interesting future study would be to directly compare the automatic fast re-planning performance with respect to manual surgeon guidance (by means of a joystick) *in-vitro*. This would remove the influence of different testing conditions and soft-tissue interactions that influence the PBN's steering capabilities.

Regarding LiTT research, steerable needles seem to have great potential to improve on current methods, though our study was limited by the small dataset used. A PBN prototype, specifically designed for LiTT application is currently under development in our lab and not yet available for testing. Further studies will apply the proposed curved CAP method to a more extensive dataset. Comparison to straight CAP on a larger dataset will enable more statistically significant results. Additionally, the ongoing curved LiTT CAP front-end will be finalised together with a novel PBN design able to host a laser ablation fibre within. This could potentially be the first integrated steerable needle system for LiTT procedures.

In summary, the existing trend of efficient parallel computational methods and augmented reality in surgery should be taken into consideration to direct future improvements in the context of computer-assisted surgical planning and navigation tools. Artificial intelligence (AI) is also a growing field, however, current AI-based path planning solutions are still far from achieving optimal results in complex three-dimensional environments. Given the popularity of AI solutions and the increasing availability of data, future research should consider neurosurgical planning as a research topic with high potential.

Finally, future research in the field should consider that conducting research as part of a development project also has its challenges. The ability to manage an appropriate balance between development and research work is crucial in conducting research that is both thorough and impactful. On the other hand, the close contact with clinicians and the possibility of receiving

their feedback in the field is extremely stimulating and rewarding. As the EDEN2020 project matures further, the opportunities for impact will grow along with the challenges of isolating research from the demands of development. Future researchers should bear this keenly in mind, and also ensure that the research engages with the medical robotics community-at-large.

Bibliography

[20114] Highly resolved strain imaging during needle insertion: Results with a novel biologically inspired device. *Journal of the Mechanical Behavior of Biomedical Materials*, 30:50–60, 2014.

[ABB20] Michel A Audette, Stéphane P A Bordas, and Jason E Blatt. Robotically Steered Needles: A Survey of Neurosurgical Applications and Technical Innovations. *Robotic Surgery: Research and Reviews*, 7:1, 2020.

[ABG] Ron Alterovitz, Michael Branicky, and Ken Goldberg. Motion Planning Under Uncertainty for Image-guided Medical Needle Steering.

[Ach11] Nouara Achour. Mobile Robots Path Planning using Genetic Algorithms. *ICAS 2011 : The Seventh International Conference on Autonomic and Autonomous Systems*, (c):111–115, 2011.

[Ada20] An introduction to diffusion tensor image analysis. *MATLAB Central File Exchange*, 2020.

[AF20] Ferdinando Rodriguez y Baena Elena DeMomi Alberto Favaro, Riccardo Secoli. Model-based robust pose estimation for a multi-segment, programmable bevel-tip steerable needle. *Robotics and Automation Letters*, 2020.

[AGO05] Ron Alterovitz, Ken Goldberg, and Allison Okamura. Planning for steerable bevel-tip needle insertion through 2D soft tissue with obstacles. *Proceedings - IEEE International Conference on Robotics and Automation*, 2005(January):1640–1645, 2005.

[ALG+05] Ron Alterovitz, Andrew Lim, Ken Goldberg, Gregory S. Chirikjian, and Allison M. Okamura. Steering flexible needles under Markov motion uncertainty. *2005 IEEE/RSJ International Conference on Intelligent Robots and Systems, IROS*, pages 120–125, 2005.

[APM07] Niki Abolhassani, Rajni Patel, and Mehrdad Moallem. Needle insertion into soft tissue: A survey. *Medical Engineering & Physics*, 29(4):413–431, may 2007.

[ASG] Ron Alterovitz, Thierry Siméon, and Ken Goldberg. The Stochastic Motion Roadmap: A Sampling Framework for Planning with Markov Motion Uncertainty.

[ASG08] Ron Alterovitz, Thierry Siméon, and Ken Goldberg. The stochastic motion roadmap: A sampling framework for planning with Markov motion uncertainty. *Robotics: Science and Systems*, 3:233–240, jun 2008.

[AVP+14] Momen Abayazid, Gustaaf J. Vrooijink, Sachin Patil, Ron Alterovitz, and Sarthak Misra. Experimental evaluation of ultrasound-guided 3D needle steering in biological tissue. *International Journal of Computer Assisted Radiology and Surgery*, 9(6):931–939, nov 2014.

[BCM+13] Ninon Burgos, Manuel Jorge Cardoso, Marc Modat, Stefano Pedemonte, John Dickson, Anna Barnes, John S Duncan, David Atkinson, Simon R Arridge, Brian F Hutton, and Sebastien Ourselin. Attenuation correction synthesis for hybrid PET-MR scanners. *Medical image computing and computer-assisted intervention : MICCAI ... International Conference on Medical Image Computing and Computer-Assisted Intervention*, 16(Pt 1):147–54, 2013.

[BG07] Priyadarshi Bhattacharya and Marina L. Gavrilova. Voronoi diagram in optimal path planning. In *4th International Symposium on Voronoi Diagrams in Science and Engineering (ISVD 2007)*, pages 38–47. IEEE, jul 2007.

[BHW+16] Neil U Barua, Kirsten Hopkins, Max Woolley, Stephen O'Sullivan, Rob Harrison, Richard J Edwards, Alison S Bienemann, Marcella J Wyatt, Azeem Arshad, and Steven S Gill. A novel implantable catheter system with transcutaneous port for intermittent convection-enhanced delivery of carboplatin for recurrent glioblastoma. *Drug delivery*, 23(1):167–73, 2016.

[Bin11] Rosli Bin Omar. PATH PLANNING FOR UNMANNED AERIAL VEHICLES USING VISIBILITY LINE-BASED METHODS. Technical report, 2011.

[BSL+13] Jessica Burgner, Philip J. Swaney, Ray A. Lathrop, Kyle D. Weaver, and Robert J. Webster. Debulking From Within: A Robotic Steerable Cannula for Intracerebral Hemorrhage Evacuation. *IEEE Transactions on Biomedical Engineering*, 60(9):2567–2575, sep 2013.

[CA06] Wenyu Cheng and John R. Adler. An overview of cyberknife radiosurgery. *Chinese Journal of Clinical Oncology*, 3(4):229–243, Aug 2006.

[Cen05] Fernando Cendes. Mesial temporal lobe epilepsy syndrome: an updated overview. *Journal of Epilepsy and Clinical Neurophysiology*, 11(3):141–144, 2005.

[CF19] Antonella Castellano and Andrea Falini. EDEN2020 Human Brain MRI Datasets for Healthy Volunteers, 2019.

[CKB+17] Imen Chaari, Anis Koubaa, Hachemi Bennaceur, Adel Ammar, Maram Alajlan, and Habib Youssef. Design and performance analysis of global path planning techniques for autonomous mobile robots in grid environments. *International Journal of Advanced Robotic Systems*, 14(2):172988141666366, apr 2017.

[CMW+15] M Jorge Cardoso, Marc Modat, Robin Wolz, Andrew Melbourne, David Cash, Daniel Rueckert, and Sebastien Ourselin. Geodesic Information Flows: Spatially-Variant Graphs and Their Application to Segmentation and Fusion. *IEEE transactions on medical imaging*, 34(9):1976–88, sep 2015.

[CPC+17] Yue Chen, Megan E. Poorman, David B. Comber, E. Bryn Pitt, Cindy Liu, Isuru S. Godage, Hong Yu, William A. Grissom, Eric J. Barth, and Robert J. Webster. Treating Epilepsy via Thermal Ablation: Initial Experiments With an MRI-Guided Concentric Tube Robot. In *2017 Design of Medical Devices Conference.* American Society of Mechanical Engineers, apr 2017.

[CPG+16] David B. Comber, E. Bryn Pitt, Hunter B. Gilbert, Matthew W. Powelson, Emily Matijevich, Joseph S. Neimat, Robert J. Webster, and Eric J. Barth. Optimization of Curvilinear Needle Trajectories for Transforamenal Hippocampotomy. *Operative Neurosurgery*, 13(1):1, jul 2016.

[CPG+17] David B. Comber, E. Bryn Pitt, Hunter B. Gilbert, Matthew W. Powelson, Emily Matijevich, Joseph S. Neimat, Robert J. Webster, and Eric J. Barth. Optimization of Curvilinear Needle Trajectories for Transforamenal Hippocampotomy. *Operative Neurosurgery*, 13(1):15–22, feb 2017.

[CSHZ20] Chenxu Cai, Chunsheng Sun, Ying Han, and Qinhe Zhang. Clinical flexible needle puncture path planning based on particle swarm optimization. *Computer Methods and Programs in Biomedicine*, 193:105511, sep 2020.

[cvx] (18) CVX: MATLAB software for disciplined convex programming — M Grant — Request PDF.

[CYD+12] Chiara Caborni, Seong Young Ko, Elena De Momi, Giancarlo Ferrigno, and Ferdinando Rodriguez Baena. Risk-Based Path Planning for a Steerable Flexible Probe for Neurosurgical Intervention. *International Conference on Biomedical Robotics and Biomechatronics Roma*, 2012.

[DASG08] Vincent Duindam, Ron Alterovitz, Shankar Sastry, and Ken Goldberg. Screw-based motion planning for bevel-tip flexible needles in 3D environments with obstacles. In *Proceedings - IEEE International Conference on Robotics and Automation*, pages 2483–2488. IEEE, may 2008.

[D'E12]   John D'Errico. (2012b) Interparc function. MATLAB Central – File Exchange, 2012.

[DHM⁺95]   Glauser D, Fankhauser H, Epitaux M, Hefti JL, and Jaccottet A. Neurosurgical Robot Minerva: First Results and Current Developments. *Journal of image guided surgery*, 1(5), 1995.

[DJGK91]   J. M. Drake, M. Joy, A. Goldenberg, and D. Kreindler. Computer- and robot-assisted resection of thalamic astrocytomas in children. *Neurosurgery*, 29(1):27–33, Jul 1991.

[DLIB10]   Pierre E. Dupont, Jesse Lock, Brandon Itkowitz, and Evan Butler. Design and control of concentric-tube robots. *IEEE Transactions on Robotics*, 26(2):209–225, 2010.

[DLV⁺15]   Daniel L Drane, David W Loring, Natalie L Voets, Michele Price, Jeffrey G Ojemann, Jon T Willie, Amit M Saindane, Vaishali Phatak, Mirjana Ivanisevic, Scott Millis, Sandra L Helmers, John W Miller, Kimford J Meador, and Robert E Gross. Better object recognition and naming outcome with MRI-guided stereotactic laser amygdalohippocampotomy for temporal lobe epilepsy. *Epilepsia*, 56(1):101–13, jan 2015.

[DPK⁺10]   Pierre François D'haese, Srivatsan Pallavaram, Peter E. Konrad, Joseph Neimat, J. Michael Fitzpatrick, and Benoit M. Dawant. Clinical accuracy of a customized stereotactic platform for deep brain stimulation after accounting for brain shift. *Stereotactic and Functional Neurosurgery*, 88(2):81–87, 2010.

[DS05a]   S.P. DiMaio and S.E. Salcudean. Interactive Simulation of Needle Insertion Models. *IEEE Transactions on Biomedical Engineering*, 52(7):1167–1179, jul 2005.

[DS05b]   S.P. DiMaio and S.E. Salcudean. Interactive Simulation of Needle Insertion Models. *IEEE Transactions on Biomedical Engineering*, 52(7):1167–1179, jul 2005.

[EM19]   Stefano Galvan Ferdinando Rodriguez y Baena Eloise Matheson, Riccardo Secoli. Human-Robot Visual Interface for 3D Steering of a Flexible, Bioinspired Needle for Neurosurgery. In *2019 IEEE IROS*. IEEE IROS, 2019.

[EMKR10] Johnathan A Engh, Davneet S Minhas, Douglas Kondziolka, and Cameron N Riviere. Percutaneous Intracerebral Navigation by Duty-Cycled Spinning of Flexible Bevel-Tipped Needles. *Neurosurgery*, 67(4):1117–1123, oct 2010.

[FFK+12] Luca Frasson, Francesco Ferroni, Seong Young Ko, Gorkem Dogangil, and Ferdinando Rodriguez y Baena. Experimental evaluation of a novel steerable probe with a programmable bevel tip inspired by nature. *Journal of Robotic Surgery*, 6(3):189–197, sep 2012.

[FKT+10a] L Frasson, S Y Ko, A Turner, T Parittotokkaporn, J F Vincent, and F Rodriguez y Baena. STING: a soft-tissue intervention and neurosurgical guide to access deep brain lesions through curved trajectories. *Proceedings of the Institution of Mechanical Engineers. Part H, Journal of engineering in medicine*, 224(6):775–88, jun 2010.

[FKT+10b] L Frasson, S Y Ko, A Turner, T Parittotokkaporn, J F Vincent, and F. Rodriguez Y Baena. STING: A soft-tissue intervention and neurosurgical guide to access deep brain lesions through curved trajectories. *Proceedings of the Institution of Mechanical Engineers, Part H: Journal of Engineering in Medicine*, 224(6):775–788, 2010.

[FKT+10c] L Frasson, S Y Ko, A Turner, T Parittotokkaporn, J F Vincent, and F Rodriguez y Baena. STING: a soft-tissue intervention and neurosurgical guide to access deep brain lesions through curved trajectories. *Proceedings of the Institution of Mechanical Engineers. Part H, Journal of engineering in medicine*, 224(6):775–88, jun 2010.

[FSM18a] Johannes Fauser, Georgios Sakas, and Anirban Mukhopadhyay. Planning non-

linear access paths for temporal bone surgery. *International Journal of Computer Assisted Radiology and Surgery*, 13(5):637–646, 2018.

[FSM18b]   Johannes Fauser, Georgios Sakas, and Anirban Mukhopadhyay. Planning nonlinear access paths for temporal bone surgery. *International Journal of Computer Assisted Radiology and Surgery*, 13(5):637–646, may 2018.

[FSRyBDew]   Alberto Favaro, Riccardo Secoli, Ferdinando Rodriguez y Baena, and Elena DeMomi. Model-based robust pose estimation for a multi-segment, programmable bevel-tip steerable needle. In *2020 IEEE*. IEEE Robotics and automation letter, 2020 - second review.

[GAL+19]   Sanjeet S Grewal, Mohammed Ali Alvi, Victor M Lu, Waseem Wahood, Gregory A Worrell, William Tatum, Robert E Wharen, and Jamie J Van Gompel. Magnetic Resonance-Guided Laser Interstitial Thermal Therapy Versus Stereotactic Radiosurgery for Medically Intractable Temporal Lobe Epilepsy: A Systematic Review and Meta-Analysis of Seizure Outcomes and Complications. *World neurosurgery*, 122:e32–e47, feb 2019.

[GBW+13]   T Gill, N U Barua, M Woolley, A S Bienemann, D E Johnson, S O'Sullivan S O'Sullivan, G Murray, C Fennelly, O Lewis, C Irving, M J Wyatt, P Moore, and S S Gill. In vitro and in vivo testing of a novel recessed-step catheter for reflux-free convection-enhanced drug delivery to the brain. *Journal of neuroscience methods*, 219(1):1–9, sep 2013.

[GBWG+19]   Marian Galovic, Irene Baudracco, Evan Wright-Goff, Galo Pillajo, Parashkev Nachev, Britta Wandschneider, Friedrich Woermann, Pamela Thompson, Sallie Baxendale, Andrew W McEvoy, Mark Nowell, Matteo Mancini, Sjoerd B Vos, Gavin P Winston, Rachel Sparks, Ferran Prados, Anna Miserocchi, Jane de Tisi, Louis André Van Graan, Roman Rodionov, Chengyuan Wu, Mahdi Alizadeh, Lauren Kozlowski, Ashwini D Sharan, Lohith G Kini, Kathryn A Davis, Brian Litt, Sebastien Ourselin, Solomon L Moshé, Josemir W A Sander,

Wolfgang Löscher, John S Duncan, and Matthias J Koepp. Association of Piriform Cortex Resection With Surgical Outcomes in Patients With Temporal Lobe Epilepsy. *JAMA neurology*, 76(6):690–700, 2019.

[GNH18] Rüdiger Göbl, Nassir Navab, and Christoph Hennersperger. SUPRA: open-source software-defined ultrasound processing for real-time applications. *International Journal of Computer Assisted Radiology and Surgery*, 13(6):759–767, 2018.

[GS07] Daniel Glozman and Moshe Shoham. Image-guided robotic flexible needle steering. *IEEE Transactions on Robotics*, 23(3):459–467, 2007.

[GSB] Jonathan D Gammell, Siddhartha S Srinivasa, and Timothy D Barfoot. Informed RRT*: Optimal Sampling-based Path Planning Focused via Direct Sampling of an Admissible Ellipsoidal Heuristic. Technical report.

[HAE+15] R. Lyle Hood, Rudy T. Andriani, Tobias E. Ecker, John L. Robertson, and Christopher G. Rylander. Characterizing Thermal Augmentation of Convection-Enhanced Drug Delivery with the Fiberoptic Microneedle Device. *Engineering*, 1(3):344–350, sep 2015.

[HBM+19] Ayoung Hong, Quentin Boehler, Roman Moser, Ajmal Zemmar, Lennart Stieglitz, and Bradley J. Nelson. 3D path planning for flexible needle steering in neurosurgery. Technical Report 4, 2019.

[HG10] S Hota and D Ghose. Optimal geometrical path in 3D with curvature constraint. In *2010 IEEE/RSJ International Conference on Intelligent Robots and Systems*, pages 113–118. IEEE, oct 2010.

[HNR68] Peter Hart, Nils Nilsson, and Bertram Raphael. A Formal Basis for the Heuristic Determination of Minimum Cost Paths. *IEEE Transactions on Systems Science and Cybernetics*, 4(2):100–107, 1968.

[HWH+17] Christian Hoppe, Juri-Alexander Witt, Christoph Helmstaedter, Thomas

Gasser, Hartmut Vatter, and Christian E Elger. Laser interstitial thermotherapy (LiTT) in epilepsy surgery. *Seizure*, 48:45–52, may 2017.

[IYS+14] Michael E. Ivan, Jay Yarlagadda, Akriti P. Saxena, Alastair J. Martin, Philip A. Starr, W. Keith Sootsman, and Paul S. Larson. Brain shift during bur hole–based procedures using interventional MRI. *Journal of Neurosurgery*, 121(1):149–160, jul 2014.

[JDAG08] Xu Jijie, Vincent Duindam, Ron Alterovitz, and Ken Goldberg. Motion planning for steerable needles in 3D environments with obstacles using Rapidly-exploring random trees and backchaining. Technical report, 2008.

[JKS+17] Walter J Jermakowicz, Andres M Kanner, Samir Sur, Christina Bermudez, Pierre-Francois D'Haese, John Paul G Kolcun, Iahn Cajigas, Rui Li, Carlos Millan, Ramses Ribot, Enrique A Serrano, Naymee Velez, Merredith R Lowe, Gustavo J Rey, and Jonathan R Jagid. Laser thermal ablation for mesiotemporal epilepsy: Analysis of ablation volumes and trajectories. *Epilepsia*, 58(5):801–810, 2017.

[KC09] V. Kallem and N.J. Cowan. Image Guidance of Flexible Tip-Steerable Needles. *IEEE Transactions on Robotics*, 25(1):191–196, feb 2009.

[KDG+20a] F. Khan, A. Donder, S. Galvan, F. R. y. Baena, and S. Misra. Pose measurement of flexible medical instruments using fiber bragg gratings in multi-core fiber. *IEEE Sensors Journal*, pages 1–1, 2020.

[KDG+20b] Fouzia Khan, Abdulhamit Donder, Stefano Galvan, Ferdinando Rodriguez Y. Baena, and Sarthak Misra. Pose Measurement of Flexible Medical Instruments Using Fiber Bragg Gratings in Multi-Core Fiber. *IEEE Sensors Journal*, 20(18):10955–10962, sep 2020.

[KDH14] B. Konh, N. V. Datla, and P. Hutapea. Dynamic estimation of an active surgical needle deflection for brachytherapy procedures. In *2014 40th Annual Northeast Bioengineering Conference (NEBEC)*, pages 1–2. IEEE, apr 2014.

[KE]   J. Kennedy and R. Eberhart. Particle swarm optimization. In *Proceedings of ICNN'95 - International Conference on Neural Networks*, volume 4, pages 1942–1948. IEEE.

[Kha]   Oussama Khatib. Real-Time Obstacle Avoidance for Manipulators and Mobile Robots.

[KHJH88] Y. S. Kwoh, J. Hou, E. A. Jonckheere, and S. Hayati. A robot with improved absolute positioning accuracy for CT guided stereotactic brain surgery. *IEEE Trans Biomed Eng*, 35(2):153–160, Feb 1988.

[KS00]   James J Kuffner and Jr M Steven LaValle. RRT-Connect: An Efficient Approach to Single-Query Path Planning. Technical report, 2000.

[Lav06] Steven M Lavalle. Planning Algorithms. 2006.

[LGCSR16] Fangde Liu, Arnau Garriga-Casanovas, Riccado Secoli, and Ferdinando Rodriguez y Baena. Fast and Adaptive Fractal Tree-Based Path Planning for Programmable Bevel Tip Steerable Needles. *IEEE Robotics and Automation Letters*, 1(2):601–608, jul 2016.

[LJL+17a] Pan Li, Shan Jiang, Dong Liang, Zhiyong Yang, Yan Yu, and Wei Wang. Modeling of path planning and needle steering with path tracking in anatomical soft tissues for minimally invasive surgery. *Medical Engineering and Physics*, 41(January):35–45, 2017.

[LJL+17b] Pan Li, Shan Jiang, Dong Liang, Zhiyong Yang, Yan Yu, and Wei Wang. Modeling of path planning and needle steering with path tracking in anatomical soft tissues for minimally invasive surgery. *Medical Engineering & Physics*, 41:35–45, mar 2017.

[LJYY]   Pan Li, Shan Jiang, Jun Yang, and Zhiyong Yang. A Combination Method of Artificial Potential Field and Improved Conjugate Gradient for Trajectory Planning for Needle Insertion into Soft Tissue. *Journal of Medical and Biological Engineering*, 34(6):568–573.

[LKR18] Changsheng Li, Nicolas Kon Kam King, and Hongliang Ren. A Skull-Mounted Robot with a Compact and Lightweight Parallel Mechanism for Positioning in Minimally Invasive Neurosurgery. *Annals of Biomedical Engineering*, 46(10):1465–1478, 2018.

[LOR16] Alexander Leibinger, Matthew J. Oldfield, and Ferdinando Rodriguez y Baena. Minimally disruptive needle insertion: a biologically inspired solution. *Interface Focus*, 6(3):20150107, jun 2016.

[LSLL98] J P Laumond, S Sekhavat, F Lamiraux, and Jean-Paul Laumond. Guidelines in Nonholonomic Motion Planning for Mobile Robots Robot Motion Planning and Control Guidelines in Nonholonomic Motion Planning for Mobile Robots. Technical report, 1998.

[LT11] Chi-Tai Lee and Ching-Chih Tsai. 3D Collision-Free Trajectory Generation Using Elastic Band Technique for an Autonomous Helicopter. *CCIS*, 212:34–41, 2011.

[LVR+13] Mohsen LA, Shi V, Jena R, Gillard JH, and Price SJ. Diffusion tensor invasive phenotypes can predict progression-free survival in glioblastomas. *British journal of neurosurgery*, 27(4), 2013.

[LVS+19] Kuo Li, Vejay N. Vakharia, Rachel Sparks, Lucas G.S. França, Alejandro Granados, Andrew W. McEvoy, Anna Miserocchi, Maode Wang, Sebastien Ourselin, and John S. Duncan. Optimizing Trajectories for Cranial Laser Interstitial Thermal Therapy Using Computer-Assisted Planning: A Machine Learning Approach. *Neurotherapeutics*, 16(1):182–191, 2019.

[LZP+02] Qing Hang Li, Lucía Zamorano, Abhilash Pandya, Ramiro Perez, Jianxing Gong, and Fernando Diaz. The application accuracy of the neuromate robot—a quantitative comparison with frameless and frame-based surgical localization systems. *Computer Aided Surgery*, 7(2):90–98, 2002.

[MEFR07] Davneet S. Minhas, Johnathan A. Engh, Michele M. Fenske, and Cameron N. Riviere. Modeling of needle steering via duty-cycled spinning. *Annual International Conference of the IEEE Engineering in Medicine and Biology - Proceedings*, pages 2756–2759, 2007.

[Moh14] Afshin Mohammadi. A New Path Planning and Obstacle Avoidance Algorithm in Dynamic Environment. (Icee):1301–1306, 2014.

[Moh15] Nazanin Mohamadnejad. Path Planning of Nonholonomic Flying Robots Using a New Virtual Obstacle Method. pages 612–617, 2015.

[MP20] R. Secoli S. Galvan F. Rodriguez y Baena M. Pinzi, T. Watts. Adaptive Path Replanning for Orientation-constrained Needle Steering. Transaction of Biomedical Engineering, 2020.

[MPL+11] Sabine Mueller, Mei-Yin Polley, Benjamin Lee, Sandeep Kunwar, Christoph Pedain, Eva Wembacher-Schröder, Stephan Mittermeyer, Manfred Westphal, John H Sampson, Michael A Vogelbaum, David Croteau, and Susan M Chang. Effect of imaging and catheter characteristics on clinical outcome for patients in the PRECISE study. *Journal of neuro-oncology*, 101(2):267–77, jan 2011.

[MSB+18] Eloise Matheson, Riccardo Secoli, Christopher Burrows, Alexander Leibinger, and Ferdinando Rodriguez Y Baena. Cyclic Motion Control for Programmable Bevel-Tip Needles to Reduce Tissue Deformation. *Journal of Medical Robotics Research*, page S2424905X18420011, mar 2018.

[MT05] Tomas Möller and Ben Trumbore. Fast, minimum storage ray/triangle intersection. Technical report, 2005.

[MVO+18a] Hani J Marcus, Vejay N Vakharia, Sebastien Ourselin, John Duncan, Martin Tisdall, and Kristian Aquilina. Robot-assisted stereotactic brain biopsy: systematic review and bibliometric analysis. *Child's Nervous System*, 34(7):1299–1309, 2018.

[MVO+18b] Hani J. Marcus, Vejay N. Vakharia, Sebastien Ourselin, John Duncan, Martin Tisdall, and Kristian Aquilina. Robot-assisted stereotactic brain biopsy: Systematic review and bibliometric analysis. *Child's Nervous System*, 34(7):1299–1309, jul 2018.

[MWRO10] Ann Majewicz, Thomas R Wedlick, Kyle B Reed, and Allison M Okamura. Evaluation of Robotic Needle Steering in ex vivo Tissue. *IEEE International Conference on Robotics and Automation : ICRA : [proceedings]. IEEE International Conference on Robotics and Automation*, 2010:2068–2073, 2010.

[NKS+] Sherdil Niyaz, Alan Kuntz, Oren Salzman, Ron Alterovitz, and Siddhartha S Srinivasa. Following Surgical Trajectories with Concentric Tube Robots via Nearest-Neighbor Graphs. Technical report.

[PBWA14] Sachin Patil, Jessica Burgner, Robert J. Webster, and Ron Alterovitz. Needle Steering in 3-D Via Rapid Replanning. *IEEE Transactions on Robotics*, 30(4):853–864, aug 2014.

[PG15] Craig Pitcher and Yang Gao. Analysis of drill head designs for dual-reciprocating drilling technique in planetary regoliths. *Advances in Space Research*, 56(8):1765–1776, oct 2015.

[PGR19a] Marlene Pinzi, Stefano Galvan, and Ferdinando Rodriguez Y Baena. The Adaptive Hermite Fractal Tree (AHFT): a novel surgical 3D path planning approach with curvature and heading constraints. *International journal of computer assisted radiology and surgery*, 14(4):659–670, apr 2019.

[PGR19b] Marlene Pinzi, Stefano Galvan, and Ferdinando Rodriguez y Baena. The Adaptive Hermite Fractal Tree (AHFT): a novel surgical 3D path planning approach with curvature and heading constraints. *International Journal of Computer Assisted Radiology and Surgery*, 14(4):659–670, apr 2019.

[PHB17] P. Pharpatara, B. Herisse, and Y. Bestaoui. 3-D Trajectory Planning of Aerial

Vehicles Using RRT*. *IEEE Transactions on Control Systems Technology*, 25(3):1116–1123, may 2017.

[PRH+16] Andrew J. Petruska, Fabio Ruetz, Ayoung Hong, Luca Regli, Oguzkan Surucu, Ajmal Zemmar, and Bradley J. Nelson. Magnetic needle guidance for neurosurgery: Initial design and proof of concept. In *2016 IEEE International Conference on Robotics and Automation (ICRA)*, pages 4392–4397. IEEE, may 2016.

[PTC+19] Valentina Pieri, Marco Trovatelli, Marcello Cadioli, Davide Danilo Zani, Stefano Brizzola, Giuliano Ravasio, Fabio Acocella, Mauro Di Giancamillo, Luca Malfassi, Mario Dolera, Marco Riva, Lorenzo Bello, Andrea Falini, and Antonella Castellano. In vivo diffusion tensor magnetic resonance tractography of the sheep brain: An atlas of the ovine white matter fiber bundles. *Frontiers in Veterinary Science*, 6:345, 2019.

[PVdA11] Sachin Patil, Jur Van den, and Berg Ron Alterovitz. Motion Planning Under Uncertainty In Highly Deformable Environments. *Robotics science and systems : online proceedings*, jun 2011.

[PWS+ew] Marlene Pinzi, Thomas Watts, Riccardo Secoli, Stefano Galvan, and Ferdinando Rodriguez y Baena. Replanning as control method for a robotic assisted steerable needle. *IEEE Transaction of biomedical Engineering*, 1(1):1, 2020 - under second review.

[QKa] S. Quinlan and O. Khatib. Elastic bands: connecting path planning and control. pages 802–807.

[QKb] Sean Quinlan and Oussama Khatib. Elastic Bands: Connecting Path Planning and Control.

[RHM+17] Marco Riva, Christoph Hennersperger, Fausto Milletari, · Amin Katouzian, · Federico Pessina, · Benjamin Gutierrez-Becker, Antonella Castellano, · Nassir Navab, and · Lorenzo Bello. 3D intra-operative ultrasound and MR image

guidance: pursuing an ultrasound-based management of brainshift to enhance neuronavigation. *Int J CARS*, 12:1711–1725, 2017.

[RJWKC+06] III Robert J. Webster, Jin Seob Kim, Noah J. Cowan, Gregory S. Chirikjian, and Allison M. Okamura. Nonholonomic modeling of needle steering. *The International Journal of Robotics Research*, 25(5-6):509–525, 2006.

[RNK+04] M. H. T. Reinges, H.-H. Nguyen, T. Krings, B.-O. Htter, V. Rohde, and J. M. Gilsbach. Course of brain shift during microsurgical resection of supratentorial cerebral lesions: limits of conventional neuronavigation. *Acta Neurochirurgica*, 146(4):369–377, apr 2004.

[RQK+15] Seok Chang Ryu, Zhan Fan Quek, Je-Sung Koh, Pierre Renaud, Richard J. Black, Behzad Moslehi, Bruce L. Daniel, Kyu-Jin Cho, and Mark R. Cutkosky. Design of an Optically Controlled MR-Compatible Active Needle. *IEEE Transactions on Robotics*, 31(1):1–11, feb 2015.

[RS18] Ferdinando Rodriguez y Baena Riccardo Secoli. Experimental validation of curvature tracking with a programmable bevel-tip steerable needle. In *2018 International Symposium on Medical Robotics (ISMR)*, pages 1–6, 2018.

[RvdBvdDM15] Roy J. Roesthuis, Nick J. van de Berg, John J. van den Dobbelsteen, and Sarthak Misra. Modeling and steering of a novel actuated-tip needle through a soft-tissue simulant using Fiber Bragg Grating sensors. In *2015 IEEE International Conference on Robotics and Automation (ICRA)*, pages 2283–2289. IEEE, may 2015.

[SAP+10] John H. Sampson, Gary Archer, Christoph Pedain, Eva Wembacher-Schröder, Manfred Westphal, Sandeep Kunwar, Michael A. Vogelbaum, April Coan, James E. Herndon, Raghu Raghavan, Martin L. Brady, David A. Reardon, Allan H. Friedman, Henry S. Friedman, M. Inmaculada Rodríguez-Ponce, Susan M. Chang, Stephan Mittermeyer, David Croteau, Raj K. Puri, and ˍ ˍ.

Poor drug distribution as a possible explanation for the results of the PRE-CISE trial. *Journal of Neurosurgery*, 113(2):301–309, aug 2010.

[SBGW13] Philip J. Swaney, Jessica Burgner, Hunter B. Gilbert, and Robert J. Webster. A flexure-based steerable needle: High curvature with reduced tissue damage. *IEEE Transactions on Biomedical Engineering*, 60(4):906–909, 2013.

[SDH+14] John Schulman, Yan Duan, Jonathan Ho, Alex Lee, Ibrahim Awwal, Henry Bradlow, Jia Pan, Sachin Patil, Ken Goldberg, and Pieter Abbeel. Motion planning with sequential convex optimization and convex collision checking. *The International Journal of Robotics Research*, 33(9):1251–1270, aug 2014.

[SKBD17] M. Scali, D. Kreeft, P. Breedveld, and D. Dodou. Design and evaluation of a wasp-inspired steerable needle. volume 10162, page 1016207. International Society for Optics and Photonics, apr 2017.

[SMG+20] Riccardo Secoli, Eloise Matheson, Stefano Galvan, Marlene Pinzi, Tom Watts, Abdul Donder, and Ferdinando Rodriguez y Baena. A Modular Robotic Platform for Precision Neurosurgery with a Programmable Bevel-Tip Needle. In *The International Journal of Robotics Research*, 2020.

[SPF+19a] Alice Segato, Valentina Pieri, Alberto Favaro, Marco Riva, Andrea Falini, Elena De Momi, and Antonella Castellano. Automated steerable path planning for deep brain stimulation safeguarding fiber tracts and deep gray matter nuclei. *Frontiers in Robotics and AI*, 6:70, aug 2019.

[SPF+19b] Alice Segato, Valentina Pieri, Alberto Favaro, Marco Riva, Andrea Falini, Elena De Momi, and Antonella Castellano. Automated Steerable Path Planning for Deep Brain Stimulation Safeguarding Fiber Tracts and Deep Gray Matter Nuclei. *Frontiers in Robotics and AI*, 6:70, aug 2019.

[SR13a] Riccardo Secoli and Ferdinando Rodriguez y Baena. Closed-loop 3D motion modeling and control of a steerable needle for soft tissue surgery. In *2013*

IEEE International Conference on Robotics and Automation, pages 5831–5836. IEEE, may 2013.

[SR13b] Seong Young Seong Young Ko and Ferdinando Rodriguez y Baena. Toward a Miniaturized Needle Steering System With Path Planning for Obstacle Avoidance. *IEEE Transactions on Biomedical Engineering*, 60(4):910–917, apr 2013.

[SR16] Riccardo Secoli and Ferdinando Rodriguez y Baena. Adaptive path-following control for bio-inspired steerable needles. In *2016 6th IEEE International Conference on Biomedical Robotics and Biomechatronics (BioRob)*, pages 87–93, June 2016.

[SRB18] R. Secoli, F. Rodriguez, and Baena. Experimental validation of curvature tracking with a programmable bevel-tip steerable needle. In *2018 International Symposium on Medical Robotics (ISMR)*, pages 1–6. IEEE, mar 2018.

[SSCD] Alice Segato, Luca Sestini, Antonella Castellano, and Elena De Momi. *GA3C Reinforcement Learning for Surgical Steerable Catheter Path Planning.*

[ST09] Nasser Sadati and Meysam Torabi. Adaptive 2D-Path Optimization of Steerable Bevel-Tip Needles in Uncertain Model of Brain Tissue. In *2009 WRI World Congress on Computer Science and Information Engineering*, pages 254–260. IEEE, 2009.

[TBV17] Skander Taamallah, Xavier Bombois, and Paul M.J. Van den Hof. Trajectory planning and trajectory tracking for a small-scale helicopter in autorotation. *Control Engineering Practice*, 58:88–106, jan 2017.

[TBZ+ew] Marco Trovatelli, Stefano Brizzola, Davide Danilo Zani, Marco Riva, Antonella Castellano, Max Woolley, Patrick Moore, Ruan Terblanche, David Johnson, Fabio Acocella, Ferdinando Rodriguez y Baena, Lorenzo Bello, Andrea Falini, and Riccardo Secoli. Development and in-vivo assessment of a novel mri-compatible stereotactic system for the ovine animal model. *Journal of Neuroscience Methods*, TBC(TBC), 2020 - second review.

[TDBF] P Tirelli, E De Momi, N A Borghese, and G Ferrigno. COMPUTER AS-SISTED NEUROSURGERY An intelligent atlas-based planning system for keyhole neurosurgery.

[TDR+20] Michele Terzano, Daniele Dini, Ferdinando Rodriguez y Baena, Andrea Spagnoli, and Matthew Oldfield. An adaptive finite element model for steerable needles. *Biomechanics and Modeling in Mechanobiology*, 19(5):1809–1825, oct 2020.

[Tro12] Miri Trope. *Planning safe trajectories in image-guided keyhole neurosurgery Supervised by.* PhD thesis, 2012.

[TYLC18] Xiaoyu Tan, Pengqian Yu, Kah-Bin Lim, and Chee-Kong Chui. Robust path planning for flexible needle insertion using Markov decision processes. *International Journal of Computer Assisted Radiology and Surgery*, 13(9):1439–1451, sep 2018.

[VA15] M. A. Vogelbaum and M. K. Aghi. Convection-enhanced delivery for the treatment of glioblastoma. *Neuro-Oncology*, 17(suppl 2):ii3–ii8, mar 2015.

[VAP+14] Gustaaf J Vrooijink, Momen Abayazid, Sachin Patil, Ron Alterovitz, and Sarthak Misra. Needle path planning and steering in a three-dimensional non-static environment using two-dimensional ultrasound images. *The International Journal of Robotics Research*, 33(10):1361–1374, 2014.

[VDTB97] Marc Vaillant, Christos Davatzikos, Russell H Taylor, and R Nick Bryan. A path-planning algorithm for image-guided neurosurgery. In Jocelyne Troccaz, Eric Grimson, and Ralph Mösges, editors, *CVRMed-MRCAS'97*, pages 467–476, Berlin, Heidelberg, 1997. Springer Berlin Heidelberg.

[VHW+12] Louis C Vazquez, Erik Hagel, Bradley J Willenberg, Wei Dai, Fernando Casanova, Christopher D Batich, and Malisa Sarntinoranont. Polymer-coated cannulas for the reduction of backflow during intraparenchymal infusions. *Journal of materials science. Materials in medicine*, 23(8):2037–46, aug 2012.

[VRB+19] Vikas Vazhayil, Madhav Rao, Manish Beniwal, Nishanth Sadashiva, Narasinga Rao Kannepalli, Venkata Lakshmi, and Sampath Somanna. An Overview of Robotics in Functional Neurosurgery. *J Neurosurg*, 8:6–10, 2019.

[VSL+18] Vejay N. Vakharia, Rachel Sparks, Kuo Li, Aidan G. O'Keeffe, Anna Miserocchi, Andrew W. McEvoy, Michael R. Sperling, Ashwini Sharan, Sebastien Ourselin, John S. Duncan, and Chengyuan Wu. Automated trajectory planning for laser interstitial thermal therapy in mesial temporal lobe epilepsy. *Epilepsia*, 59(4):814–824, 2018.

[VSL+19] Vejay N. Vakharia, Rachel E. Sparks, Kuo Li, Aidan G. O'Keeffe, Fernando Pérez-García, Lucas G.S. França, Andrew L. Ko, Chengyuan Wu, Joshua P. Aronson, Brett E. Youngerman, Ashwini Sharan, Guy McKhann, Sebastien Ourselin, and John S. Duncan. Multicenter validation of automated trajectories for selective laser amygdalohippocampectomy. *Epilepsia*, 60(9):1949–1959, 2019.

[VSMM] Laurence Vancamberg, Anis Sahbani, Serge Muller, and Guillaume Morel. Needle Path Planning for Digital Breast Tomosynthesis Biopsy.

[VSV+] Vejay N Vakharia, Rachel E Sparks, Sjoerd B Vos, Yarema Bezchlibnyk, Ashesh D Mehta, Jon T Willie, Chengyuan Wu, Ashwini Sharan, Sebastien Ourselin, and John S Duncan. Computer-assisted planning for minimally invasive anterior two-thirds laser corpus callosotomy: A feasibility study with probabilistic tractography validation. *NeuroImage. Clinical*, page 102174.

[VSV+20] Vejay N. Vakharia, Rachel E. Sparks, Sjoerd B. Vos, Yarema Bezchlibnyk, Ashesh D. Mehta, Jon T. Willie, Chengyuan Wu, Ashwini Sharan, Sebastien Ourselin, and John S. Duncan. Computer-assisted planning for minimally invasive anterior two-thirds laser corpus callosotomy: A feasibility study with probabilistic tractography validation: Automated laser callosotomy trajectory planning. *NeuroImage: Clinical*, 25(October 2019):102174, 2020.

[WA14] Wen Sun and Ron Alterovitz. Motion planning under uncertainty for medical needle steering using optimization in belief space. In *2014 IEEE/RSJ International Conference on Intelligent Robots and Systems*, pages 1775–1781. IEEE, sep 2014.

[WGJD08] E. P. Westebring – van der Putten, R. H. M. Goossens, J. J. Jakimowicz, and J. Dankelman. Haptics in minimally invasive surgery – a review. *Minimally Invasive Therapy & Allied Technologies*, 17(1):3–16, jan 2008.

[WJ10] R. J. Webster and B. a. Jones. Design and Kinematic Modeling of Constant Curvature Continuum Robots: A Review. *The International Journal of Robotics Research*, 29(13):1661–1683, 2010.

[WJC$^+$19a] Chengyuan Wu, Walter J. Jermakowicz, Srijata Chakravorti, Iahn Cajigas, Ashwini D. Sharan, Jonathan R. Jagid, Caio M. Matias, Michael R. Sperling, Robert Buckley, Andrew Ko, Jeffrey G. Ojemann, John W. Miller, Brett Youngerman, Sameer A. Sheth, Guy M. McKhann, Adrian W. Laxton, Daniel E. Couture, Gautam S. Popli, Alexander Smith, Ashesh D. Mehta, Allen L. Ho, Casey H. Halpern, Dario J. Englot, Joseph S. Neimat, Peter E. Konrad, Elliot Neal, Fernando L. Vale, Kathryn L. Holloway, Ellen L. Air, Jason Schwalb, Benoit M. Dawant, and Pierre-Francois D'Haese. Effects of surgical targeting in laser interstitial thermal therapy for mesial temporal lobe epilepsy: A multicenter study of 234 patients. *Epilepsia*, 60(6):epi.15565, may 2019.

[WJC$^+$19b] Chengyuan Wu, Walter J Jermakowicz, Srijata Chakravorti, Iahn Cajigas, Ashwini D Sharan, Jonathan R Jagid, Caio M Matias, Michael R Sperling, Robert Buckley, Andrew Ko, Jeffrey G Ojemann, John W Miller, Brett Youngerman, Sameer A Sheth, Guy M McKhann, Adrian W Laxton, Daniel E Couture, Gautam S Popli, Alexander Smith, Ashesh D Mehta, Allen L Ho, Casey H Halpern, Dario J Englot, Joseph S Neimat, Peter E Konrad, Elliot Neal, Fernando L Vale, Kathryn L Holloway, Ellen L Air, Jason Schwalb,

Benoit M Dawant, and Pierre-Francois D'Haese. Effects of surgical targeting in laser interstitial thermal therapy for mesial temporal lobe epilepsy: A multicenter study of 234 patients. *Epilepsia*, 60(6):1171–1183, 2019.

[WJLS17] Xiaoliang Wang, Peng Jiang, Deshi Li, and Tao Sun. Curvature Continuous and Bounded Path Planning for Fixed-Wing UAVs. *Sensors*, 17(9):2155, sep 2017.

[WOS+15] Hena Waseem, Katie E Osborn, Mike R Schoenberg, Valerie Kelley, Ali Bozorg, Daniel Cabello, Selim R Benbadis, and Fernando L Vale. Laser ablation therapy: An alternative treatment for medically resistant mesial temporal lobe epilepsy after age 50. *Epilepsy & behavior : E&B*, 51:152–7, oct 2015.

[WPS+19] Elysa Widjaja, Tina Papastavros, Beate Sander, Carter Snead, and Petros Pechlivanoglou. Early economic evaluation of MRI-guided laser interstitial thermal therapy (MRgLITT) and epilepsy surgery for mesial temporal lobe epilepsy. *PLoS ONE*, 14(11), 2019.

[WSB18] Thomas Watts, Riccardo Secoli, and Ferdinando Rodriguez Baena. Needle Steerability Measures: Definition and Application for Optimized Steering of the Programmable Bevel-Tip Needle. In *2018 IEEE International Conference on Robotics and Biomimetics, ROBIO 2018*, pages 59–64. IEEE, dec 2018.

[WSB19a] Thomas Watts, Riccardo Secoli, and Ferdinando Rodriguez y Baena. A Mechanics-Based Model for 3-D Steering of Programmable Bevel-Tip Needles. *IEEE Transactions on Robotics*, 35(2):371–386, apr 2019.

[WSB19b] Thomas Watts, Riccardo Secoli, and Ferdinando Rodriguez y Baena. A Mechanics-Based Model for 3-D Steering of Programmable Bevel-Tip Needles. *IEEE Transactions on Robotics*, 35(2):371–386, apr 2019.

[WSyB18] T. Watts, R. Secoli, and Ferdinando. Rodriguez y Baena. Needle steerability measures: Definition and application for optimized steering of the

programmable bevel-tip needle. In *2018 IEEE International Conference on Robotics and Biomimetics (ROBIO)*, pages 59–64, 2018.

[YC04]   Jun Hai Yong and Fuhua Cheng. Geometric Hermite curves with minimum strain energy. *Computer Aided Geometric Design*, 21(3):281–301, 2004.

[YK16]   Byunghyun Yoo and Jinwhan Kim. Path optimization for marine vehicles in ocean currents using reinforcement learning. *JOURNAL OF MARINE SCIENCE AND TECHNOLOGY*, 21(2):334–343, jun 2016.

[YMY+14] Kwangjin Yang, Sangwoo Moon, Seunghoon Yoo, Jaehyeon Kang, Nakju Lett Doh, Hong Bong Kim, and Sanghyun Joo. Spline-Based RRT Path Planner for Non-Holonomic Robots. *Journal of Intelligent & Robotic Systems*, 73(1-4):763–782, jan 2014.

[YNN+18] Atsushi Yamada, Shigeyuki Naka, Norihisa Nitta, Shigehiro Morikawa, and Tohru Tani. A Loop-Shaped Flexible Mechanism for Robotic Needle Steering. *IEEE Robotics and Automation Letters*, 3(2):648–655, apr 2018.

[YQS+16] Liang Yang, Juntong Qi, Dalei Song, Jizhong Xiao, Jianda Han, and Yong Xia. Survey of Robot 3D Path Planning Algorithms. *Journal of Control Science and Engineering*, 2016:1–22, 2016.

[ZDB19] Wenbo Zhan, Daniele Dini, and Ferdinando Rodriguez y Baena. Transport of Chemotherapeutic Agents in Anisotropic Tissue under Convection Enhanced Delivery for Localised Treatment, 2019.

[ZSP15] Zhijie Zhu, Edward Schmerling, and Marco Pavone. A convex optimization approach to smooth trajectories for motion planning with car-like robots. *Proceedings of the IEEE Conference on Decision and Control*, 54rd IEEE:835–842, jun 2015.

[ZW18a] Wenbo Zhan and Chi-Hwa Wang. Convection enhanced delivery of chemotherapeutic drugs into brain tumour. *Journal of Controlled Release*, 271:74–87, feb 2018.

[ZW18b]   Wenbo Zhan and Chi-Hwa Wang. Convection enhanced delivery of chemother-
          apeutic drugs into brain tumour. *Journal of Controlled Release*, 271:74–87, feb
          2018.

[ZWZ⁺]   Yan-Jiang Zhao, Wen-Qiang Wu, Yong-De Zhang, Rui-Xue Wang, Jing-Chun
          Peng, and Yan Yu. 3D Dynamic Motion Planning for Robot-assisted Cannula
          Flexible Needle Insertion into Soft Tissue. *International Journal of Advanced
          Robotic Systems*.